INVESTIGATION AND DISCOVERY OF NOVEL TRANSITION METAL CYSTEAMINE SYSTEMS WITH HALOGENS FROM THE FIRST PRINCIPLES CALCULATIONS

by

Noura Dawas Alkhaldi

DISSERTATION

Submitted in partial fulfillment of the requirements
for the degree of Doctor of Philosophy at
The University of Texas at Arlington
December, 2021

Arlington, Texas

Supervising Committee:

Muhammad N. Huda, Supervising Professor
Alexander Weiss
Qiming Zhang
Wei Chen
Yujie Chi

Abstract

Investigation and Discovery of Novel Transition Metal Cysteamine Systems with Halogens from the First Principles Calculations

Noura Dawas Alkhaldi, Ph. D.
The University of Texas at Arlington, 2021

Supervising Professor: Muhammad N. Huda

Cu-cysteamine (Cu-Cy) is a material that has the cysteamine bonded with Cu. It is a molecular photosensitizer which can be activated by visible, ultraviolet light, and X-rays to generate reactive oxygen species (ROS). Cu-Cy has been used in various applications such as solid-state lighting, radiation detection, and as treatment of both shallow and deep cancers. Hence, it is important to study the stability, electronic and optical properties of Cu-Cy as well as finding other possible cysteamine systems. The first principle theoretical investigations of novel transition metal cysteamine systems with halogens are performed by density functional theory. In the first part of this dissertation, we have studied Cu-Cy-X (X = F, Cl, Br, and I). Different spin-multiplicities are considered to understand the electron transition from the occupied to the unoccupied bands. Diffusion barriers of Cu atom to escape out of Cu-Cy-X surface are calculated to mimic the experimentally observed Cu leaching. Our theoretical results show good agreements with the experimental data.

As the experimental synthesis of all Cu-Cy-X samples contained Cl as impurity, so it is imperative to understand the effect of Cl in the stability and properties of Cu-Cy-X. Thus, in the second part of this dissertation, we have studied the mixed halogen in Cu-cysteamine Cu-Cy-Cl_n-$X2_m$ (where, X_2 = F, Br, and I) and (n = 1, 4, and 7 and m = 8 – n). We have investigated the

stability of $Cu\text{-}Cy\text{-}Cl_n\text{-}X2_m$ structures as well as their electronic and optical properties. We have seen the presence of Cl in Cu-Cy-X (X = F, Br, and I) makes the material harder.

In the last part of the dissertation, we have considered other possible transition metal cysteamine systems M-Cy-X (M = Co, Ag, Au, and Zn) and (X = F, Cl, Br, and I). Our theoretical results indicate that Ag-Cy and Au-Cy behave like Cu-Cy where all of them stabilize in singlet state. However, Co-Cy and Zn-Cy are stabilized in triplet state which means the mechanism of the optical absorption and emission will be completely different from Cu-Cy. We have also seen in triplet state, Cu-Cy-Cl behaves like semiconductor with a mid-gap state, Ag-Cy as half metal, and Au-Cy-Cl is a metal.

Acknowledgements

First, I would like to express my deep gratitude to my research advisor, Dr. Muhammad N. Huda for giving me the opportunity to conduct my research under his tutelage. My advisor has opened his door to me and allowed me to ask any questions related to my research and steered me in the right direction. He always encourages me to read in my field and increase my knowledge. Thanks for pushing me a lot to do the best. I am greatly grateful for his guidance, time, and patience. The successful of this work would not be done without his support.

I would like to thank my committee members, Dr. Alexander Weiss, Dr. Qiming Zhang, and Dr. Wei Chen and Dr. Yujie Chi for their time, and guidance which are invaluable. It was my pleasure attending their classes and improving my education through their instruction. Special thanks to my collaborators Dr. Chen and his group, I had a great pleasure working with them.

I would like to thank to my previous and current group members, Dr. Sajib Barman, Dr. Edan Bainglass, Dr. Hori Pada Sarker, Hussain Alathlawi, and Achyuth Manoj, Dr. Pranab Sarker, and Dr. Shafaq Moten for their support, and encouragement.

I would like to thank Physics department support staff at UTA specially Ms. Stacey Cody, Ms. Holly Zander, Ms. Nieshea Crow, and Mr. Victor Reece for their administrative support.

I am grateful to University of Hafr Albatin for giving me the opportunity to complete my study in USA, as well as Saudi Arabian Cultural Mission to the US for their financial support.

I would like to thank Texas Advanced Computing Center (TACC) for the generous time that allowing us to do all the calculations which are performed in this dissertation.

Lastly, I am deeply thankful to my family, especially my father who is giving me unfailing support. This accomplishment would not be possible without his support. I want to thank my mother who is not alive, nevertheless she is definitely alive in my heart. It has been years since she passed away, but I consider her lessons every day. I would like to give special thanks to my sister Hanof, she is an example of great supporters who help me when I feel I can’t do it. I would like to thank my sister Sara, my brothers Fahad, Mohammad, and Mefleh for their support and encouragements to do my best regardless the distance.

List of Figures

List of Tables

Table of Contents

Chapter 1

Introduction

Computational and theoretical methods have been utilized for the last several decades to study the electronic and crystal structures of condensed matter. The foremost goal of theory is to provide us fundamental understanding of a phenomena and predict the properties of the systems. First principal theory is useful because it does not require any experimental parameter. Density functional theory (DFT) is one of the most successful theories nowadays, and thousands of publications are published each year within the DFT framework in all over the scientific fields such as physics, chemistry, and material science. The research for this dissertation has been performed within DFT framework which will be shown in the following chapters that yields to theoretical results which can be used as guidance for the experimental. The theory and experiment together can help in facilitating the discovery of new transition metal cysteamine materials. Herein, in the introduction, we have presented an overview of studies that have done on transition metal cysteamine systems.

1.1. Literature Review on Transition Metal Cysteamine Systems

Metal complexes specially transition metal compounds have become attractive in recent times to science and technology due to their novel structures, properties, and applications [1-7] such as light emitting devices, solar cells, biological imaging, and therapeutic agents [8-12]. Among ligands, cysteamine is an organic stable molecule with both active thiol and amino groups [13]. It is a white, water-soluble solid. Cysteamine has been used widely as linking agent at metal surfaces, and it has become incredibly attractive [14-31]. It performs several physiological functions in the human body, and it is used as a drug for numerous diseases [13, 32, 33]. Cysteamine is a mercaptoethylamine compound, that is derived from the coenzyme-A degradative pathway. It can be easily transported into lysosomes and reacts with cysteine to form cysteine-cysteamine disulfide [34]. Cu(I) metal has become one of the most attractive transition metal complexes due to the fact that Cu has low cost, lower toxicity, and abundance [35-37]. Copper-cysteamine (Cu-Cy) complex is one of the convenient model compounds in the interest of essential knowledge about copper-containing enzymes [38].

1.1.1. Physical Properties of Cu-Cy

Copper–cysteamine (Cu-Cy) is a new type of Cu complexes which has been reported in 1997 [39, 40] as $Cu_{13}Cl_{13}$ $(SR)_6$ and $Cu_8Cl_8(SR)_6$ where R = $CH_2CH_2NH_3$. In 2014, Cu-Cy with the formula Cu_3Cl $(SR)_2$ where R = $CH_2CH_2NH_2$ was reported experimentally by Chen's group [41]. Cu_3Cl $(SR)_2$ where R = $CH_2CH_2NH_2$ has less atoms in its periodic unit cell than what previously were reported in 1997 [39, 40]. The XRD pattern of this Cu_3Cl $(SR)_2$ did not match with any known Cu-compounds in the present XRD database that means this Cu_3Cl $(SR)_2$ is a new compound that has never been reported [41]. Figure 1.1 presents the powder XRD pattern of Cu_3Cl $(SR)_2$ [42]. Cu-Cy is a material that has both amino and thiol groups which form cysteamine and bonded with Cu [41]. The solid-state nuclear magnetic resonance data shows that the oxidation state of Cu in Cu_3Cl $(SR)_2$ is +1 rather than +2 .

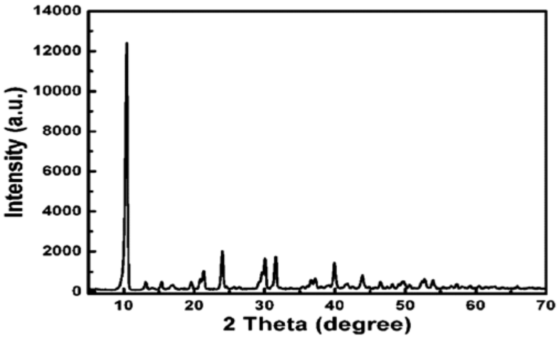

Figure 1.1. The Powder XRD pattern of Cu_3Cl $(SR)_2$ [42].

Cu-Cy is a type of photosensitizer [43, 44] that produces chemical changes in another molecule in a photochemical process. Cu-Cy can be activated by visible, ultraviolet (UV), X-rays, ultrasound, and microwaves (MW) [45] to generate reactive oxygen species (ROS), [41, 43, 45-47]. ROS is oxygen molecules in singlet state, and it is a type of unstable molecule that easily react with other molecules in the cell. ROS cause damage in DNA, RNA, and proteins, and may cause cell death [48].

Cu-Cy is considered as a molecular solid [49] which means each basis is a molecule that goes to each lattice point. A molecular solid is a solid which consist of discrete molecules meaning the building blocks are individual molecule not atom. In Cu-Cy, the inter layer bonds are very weak Van der Waals type bonds [49] and it is well known that Van der Waals binding is typically much weaker than the forces holding together other solids. The unit cell of Cu-Cy structures shows two different types of Cu atoms where the first one is Cu(1) coordinated by two S atoms and one Cl atom and the other one is Cu(2), which binds to 4 other atoms in the crystal, three sulfurs atoms and one N atom [49]. It has been reported in previous papers [39, 40] and as well in 2014 [41, 42] that Sulfur atom bridges to four Cu atoms simultaneously. Cu atom in molecular environment shows SOC effect, which is reported to be larger for Cu^{+1} Compounds [50].

1.1.2. Applications of Cu-Cy

According to the World Health Organization, cancer is one of the major causes of threatening the human's health. It is responsible for an estimated 9.6 million deaths in 2018, and it is projected that by 2040 the cases will be doubled. In fact, cancer is the second leading cause of death globally, and around the world about 1 in 6 dies due to cancer. Especially, as the breast cancer has become one of the most common causes of cancer death of female, it is important to discover new effective treatments which will be hope for the patients [51, 52]. With those facts, it is imperative to develop novel therapeutic modalities with better efficiencies as well as low side effects to treat cancer.

Beside the conventional cancer treatment methods, alternative and developed methods have been discovered, such as Photodynamic therapy (PDT) [53-62]. PDT has been found to be a highly effective therapy for certain kinds of cancers and pre-cancerous lesions. Photodynamic therapy (PDT) is referred to phototherapy and photochemotherapy where photosensitizers (PSs) are utilized to produce highly reactive oxygen species (ROS) by photoexcitation, such as hydroxyl radicals ($^{\cdot}OH$), singlet oxygen ($^1O_2$), and peroxides ($R–O–O^{\cdot}$) where the photoexcitation damages cancer cells [63-65]. The challenge of using PDT to treat tumors is direct light delivery for PDT activation. Several solutions for the light delivery have been proposed such as using photosensitizers activated by near-infrared (NIR) light that enter deeper into tissues than UV and visible light [66-68]. Nevertheless, near-infrared light activated photosensitizers reduce the singlet oxygen production efficiency [69, 70] and it has small energy gaps. It has shown that photosensitizers which can be activated directly by X-rays can overcome this problem. In 2014 [41], Lun Ma, et al. have reported Cu–Cy nanoparticles as a type of photosensitizer that can be efficiently activated by X-ray and makes PDT possible to be used in treating deep cancer [41]. Cu–Cy nanoparticles under X-ray activation showed noteworthy cell destruction in both vitro and in vivo study on human breast cancer cells (MCF-7) [41].

Also, one of the limitations to use photodynamic therapy in deeply situated tumors is the poor tissue penetration by light. This obstacle can be solved if the photosensitizers can be activated as well by microwaves (MW) to permeate deep into tissues. In 2016 [45], Mengyu Yao, et al. explored microwave-induced photodynamic therapy and exploit Cu-Cy nanoparticles as photosensitizer which can be activated by microwaves to generate singlet oxygen to treat cancer.

Moreover, Lun Ma, et al. [41] observed that the amount of singlet oxygen produced from Cu–Cy particles is higher than any other known photosensitizers using X-rays which means that Cu–Cy particles can be used for deep-seated cancers by overcoming the limitation of traditional PDT [41].

Further, Sonodynamic therapy (SDT) is one of the promising cancer treatments. However, it has a limitation due to the absences of highly efficient sonosensitizer. It was reported that Cu–Cy nanoparticles can be used as new sonosensitizers for SDT to treat breast cancer [71]. The results indicate that upon exposure of Cu–Cy to ultrasound, large amount of reactive oxygen species (ROS) is generated for cancer cell destruction with great efficiency of SDT in order to induce cell apoptosis and necrosis. It has been reported that Cu–Cy mediated SDT provides a new treatment for cancer without any side-effects [71].

As the colorectal cancer (CRC) is the third most common cancer which threat the humans' life and health, and around 1.2 million new cases are reported with 600,000 deaths per year [72], it is important to discover an effective treatment to limit the death of this type of cancer. In 2017 [73], Liu et al. studied the effects of Cu-Cy radiosensitizers on SW620 colorectal cells and it was found that Cu–Cy nanoparticle radiosensitizers can improve the X-ray radiation efficiently to damage colorectal cancer cells by inducing apoptosis and autophagy. Also, they discovered that the X-ray activated Cu-Cy nanoparticles can kill SW620 cancers cells in a dose-dependent manner [73].

In 2021, X. Chen et al. [74] investigated the treatment efficiency of Cu-Cy based X-ray induced photodynamic therapy (X-PDT) by mimicking the clinical conditions with the clinical linear accelerator and by building deep-seated tumor models in order to study the effectiveness as well as its effects on the cell migration and proliferation in the level of the cell. Their results indicate that Cu-Cy has a safe clinical application prospect in X-PDT which improve the efficiency of radiotherapy (RT) to be used in deep-seated tumors and prevent tumor cell production and migration [74].

Q. Zhang et al. in 2020 showed that the ROS produced by Cu-Cy, which is activated by X-ray, leads to direct destruction of melanoma [75]. Also, it shows that Cu–Cy and X-rays can effectively promote an antitumor immune response and in general, it can simultaneously enable radiotherapy, oxidative therapy, and immunotherapy in order to treat cancer and to overcome the limitations of conventional cancer treatment [75].

As Hepatocellular carcinoma (HCC) becomes one of the most malignant tumors in the world [76, 77], new treatment methods for liver cancer are urgently needed. In 2019, X. Huang et al. [46] reported for the first time the anti-Hepatocellular carcinoma (anti-HCC) effects of copper-cysteamine nanoparticles. They showed that the activity of HepG2 cells is reduced by very low dose of Cu-Cy NPs at a short time of ultraviolet radiation and it reduced tumor growth in vivo. In addition, Cu-Cy NPs can enter easily into exosomes secreted by tumor cell, and these exosomes can be used as a delivery of Cu-Cy NPs to target tumor cells [46].

Additionally, in 2019, Shresthaa et al.[78] reported the strong potential of pH-low insertion peptide–conjugated (pHLIP) Cu-Cy nanoparticles, combined with X-rays, as a photosensitizer for Photodynamic therapy to successfully treat mammalian cancer.

Further studies on Cu-Cy to be used as treatment of cancer have done in 2020 by Lalit Chudal et al. showed that Cu-Cy nanoparticles which has Cu^{1+} instead of Cu^{2+} can be used as an efficient heterogeneous fenton-like catalyst for highly selective cancer treatment [79]. They suggest that Cu-Cy NPs can catalyze overproduced H_2O_2 in cancer cells in order to produce higher levels of ROS, thus inducing much more cancer cell destruction than healthy cells.

In 2020, Yan Chang et al. showed that Cu-Cy NPs are new promising material which can help to provide Cu to work with DSF in order to improve the anticancer effect in esophageal cancer significantly. They proposed that the increased cytotoxic of Cu-Cy + DSF is due to the synergetic effect of the ROS production and formation of the DSF−Cu complex which can be supported by the evidence of changing in the physical color, fluorescence, and absorption spectra, as well the XRD patterns, and FTIR spectra [80]. They show that the combination of DSF and Cu-Cy induced cell killing as well as block the translocation of NF-κB (p65) into the nucleus in ESCC cells. This can help to open the door to develop new chemotherapy strategy using DSF and Cu-Cy NPs for EC and other cancer patients.

As the toxicity is an important factor to evaluate materials which are used in biological applications, the toxicity of Cu–Cy particles was tested [41] using MTT assay after the particles were cultured with MCF-7 cells for 24h [41]. It shows there is certain concentration of Cu–Cy particles which has low toxicity [41].

Moreover, Cu–Cy can be used in cell imaging during cancer treatment due to the fact that Cu-Cy have strong photoluminescence and X-ray excited luminescence [41]. Also, this indicates that Cu-Cy can be used for radiation detection and as a light source for X-ray-induced photodynamic therapy to treat cancer. In fact, $Cu_3Cl\ (SR)_2$ has strong luminescence comparing to the previous reported Cu–Cy complexes [39, 40] which has no luminescence. It has been shown that the X-ray luminescence of $Cu_3Cl\ (SR)_2$ is about 10 times stronger in intensity than ZnS:Mn and around 35 times stronger than CdTe quantum dots, and the intensity of X-ray luminescence of $Cu_3C\ l(SR)_2$ is stronger around 5 times than PVT/PPO. Those results shows that $Cu_3Cl\ (SR)_2$ is a new scintillator for radiation detection and dosimetry.

Moreover, In 2019 [81], Huang et al. discovered the possibility of using Cu-Cy NPs for bacteria inactivation by treating gram-positive bacteria and gram-negative bacteria, and their results indicate that Cu-Cy NPs are very effective in killing gram-positive bacteria but limited in killing gram-negative bacteria. The main killing mechanism is to damage the cell by singlet oxygen due to the interaction of singlet oxygen and H_2O_2. They conclude that Cu-Cy NPs are potential agents for bacteria inactivation [81].

In 2020, X. Zhen et al. have demonstrated that the combination of Cu-Cy nanoparticles and potassium iodide (KI) can help significantly in inactivating both Gram-positive MRSA and Gram-negative E. coli under UV light. It shows with the interaction in cell-free medium of KI with Cu-Cy, there were no copper ions were released which means the fenton reaction induced by copper ions is not responsible in killing the bacteria. They observed that the main killing mechanism requires the toxic species, such as hydrogen peroxide, iodide ions, singlet oxygen, and triiodide ions [82].

It is a well-known fact that the white light phosphors have many applications such as solid-state lighting, and light source, and most of these phosphors are rare-earth-based materials. These rare-earth-based materials are expensive and have limited availability. Hence, it is important to find alternative materials. In 2015 [83], it was reported for the first time a new white color composite consisted of a graphitic-phase nitrogen carbon (g-C_3N_4) treated with nitric acid and copper-cysteamine $Cu_3Cl(SR)_2$. Their results indicate that these composites can produce strong white light which could be used as solid-state lighting, and as light source as well as in full color displays due to the fact that these materials can provide blue and red emission for photosynthesis enhancement [83].

In 2020, Z. Huang et al. emerged Cu–Cy nanosheets with red fluorescence, and they have found that fluorescence of Cu–Cy can be quenched by Fe^{3+} and at the same time recovered through the removal of Fe^{3+} upon the addition of dopamine. They demonstrated that Cu–Cy nanosheets can be used for fluorescence sensing and molecular information processing, and they showed that Cu-Cy may help to develop sensors and smart molecular logic devices in sensing, biomedicine, as well as molecular computing [84].

Also, as electrochemical disinfection has become one of the most promising alternatives to the conventional decontamination of water in various applications [85, 86]. More attention has been given to reactive oxygen species (ROS) as ROS has been used to kill pathogenic microbial cells and has been used as disinfectants and antiseptics [85, 86]. Also, the morphological change of cells made by electrochemical ROS can make a noteworthy deactivation of microorganism, as high as chlorine in the electrochemical disinfection [85, 86].

In addition, as we know that industrial release of the chemical dye to water pathways makes the water toxic, such as shown in Figure 1.2, and it will be harmful for human and other lives. Cu-Cy can be used in water, and it can be activated by the sunlight. Hence, it will generate the ROS and it has been shown that ROS plays a significant role in degradation of organic dyes [87-89]. Thus, ROS from Cu-Cy can be used as decontamination of water from organic dye molecules.

Figure 1.2. The released chemical dye in the water.

In short, Cu-Cy shows great potential to be used in various applications such as therapeutics, imaging, solid state lighting, radiation detection [41, 42, 44, 46, 49, 73, 90]as well as treatment of both shallow and deep cancers [41, 42, 44, 46, 47, 71, 73, 78] and it can be tagged with functional groups for targeted drug delivery due to the fact that it can be formulated at the nanoscale [45].

1.1.3. Synthesis of Cu-Cy

Cu-Cy is easy to synthesize, and it is cost effective [41]. It has been reported that Cu–Cy complex crystals can be synthesized at room temperature and need long time for crystal growth [39, 40]. Various effective methods have been considered to synthesis Cu-Cy [45, 91, 92] such as wet chemical method with no harm to the environment due to the fact that cysteamine is nontoxic and soluble in water [41, 42, 90]. The development of the method to synthesis Cu-Cy has been done in a simpler and faster way in order to produce increasingly efficient products which is inexpensive as well [93]. The method [93] shows that there is noticeable decreasing in both the stirring and heating time by about 24 and 6 times, respectively, and that will help to make Cu–Cy nanoparticles more economical than what was reported before. This method may increase the reactivity of the Cu–Cy nanoparticles due to size reduction and it enhances the effectiveness of Cu–Cy nanoparticles for photodynamic therapy. It has been shown that the Cu–Cy particles can be synthesized at temperatures which range from 80 C° to the boiling point of water by varying reaction conditions [93]. In addition, Cu–Cy particles can be synthesized at different pH values around 6.3 to 9 and that can be done by changing certain reaction parameters [93].

Cu-Cy can be fabricated at the nano scale to increase water solubility [41]. Figure 1.3 shows the scanning electron microscope (SEM) image of $Cu_3Cl(SR)_2$ crystals in pm and μm [42].

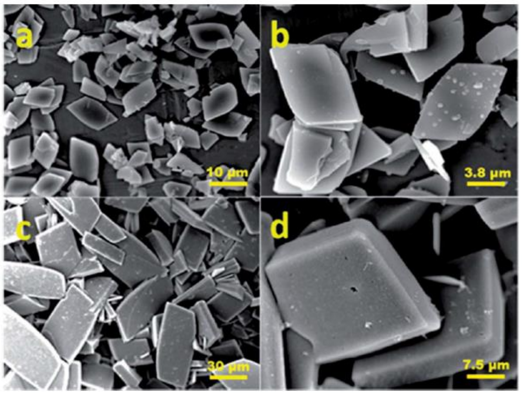

Figure 1.3. Scanning electron microscope (SEM) image of $Cu_3Cl (SR)_2$ crystals [42].

1.2. Summary

The main aim of this first principles theoretic study is to determine the electronic and optical properties of transition metal cysteamine with halogens in details which can be used in various applications and to mitigant some of environmental problem. The results that are provided in this dissertation will serve as a basic understanding to develop the new generation material which can be used in medical, technological as well as environmental applications. We have provided comprehensive examinations of the various possible transition metal cysteamine systems that can be made experimentally to those which are not synthesized yet or help improving the quality of the cysteamine systems which were already synthesized. In the next chapter, we will present the theoretical and computational methodology to study transition metal cysteamine with halogens.

Chapter 2

Theoretical and Computational Methodology

Density functional theory (DFT) is one of the most successful methods which has been used to study many-body system by using the electron density. It is a fundamental theory to study the ground state electronic properties of condensed matter and molecules. In this chapter, we will present brief descriptions of DFT and its various approximations that we have used in our calculations. The chapter is mainly from publications by Parr and Yang [94], Jones [95], Capelle [96], Cramer [97], and Walter Kohn [98], who set the foundation of density functional theory.

2.1. Many-Particle Systems

Schrödinger equation is the starting point of any system in quantum mechanics and by solving it the properties of the system can be determined.

The Hamiltonian of a material is given by the following:

$$H = T_e + T_N + V_{ee} + V_{NN} + V_{ext} \tag{2.1}$$

$$H = -\frac{\hbar^2}{2m}\sum_i \nabla_i^2 - \frac{\hbar^2}{2}\sum_\alpha \frac{\nabla_\alpha^2}{M_\alpha} + \frac{1}{2}\sum_{i\neq j}\frac{e^2}{4\pi\epsilon_0|\vec{r}_i - \vec{r}_j|} + \frac{1}{2}\sum_{\alpha\neq\beta}\frac{Z_\alpha Z_\beta e^2}{4\pi\epsilon_0|\vec{R}_\alpha - \vec{R}_\beta|} + \frac{1}{2}\sum_{i,\alpha}\frac{Z_\alpha e^2}{4\pi\epsilon_0\,|\vec{r}_i - \vec{R}_\alpha|} \tag{2.2}$$

where the first term presents electronic kinetic energy $T_e = -\frac{\hbar^2}{2m}\sum_i \nabla_i^2$,

second term is the nuclei kinetic energy $T_N = \frac{\hbar^2}{2}\sum_\alpha \frac{\nabla_\alpha^2}{M_\alpha}$,

third term is electron-electron interaction $V_{ee} = \frac{1}{2}\sum_{i\neq j}\frac{e^2}{4\pi\epsilon_0|\vec{r}_i - \vec{r}_j|}$,

fourth one is nuclei-nuclei interaction $V_{NN} = \frac{1}{2}\sum_{\alpha\neq\beta}\frac{Z_\alpha Z_\beta e^2}{4\pi\epsilon_0|\vec{R}_\alpha - \vec{R}_\beta|}$,

and the last term is electron-nuclei interaction $V_{ext} = \frac{1}{2}\sum_{i,\alpha}\frac{Z_\alpha e^2}{4\pi\epsilon_0\,|\vec{r}_i - \vec{R}_\alpha|}$, where the indices i, j are for electrons, α, β indices are related to the nucleus, M_α is the mass of nucleus α, m the mass of the electron, Z_α , and Z_β are the atomic number of nucleuses α and nucleus β respectively.

$|\vec{r}_i - \vec{r}_j|$ is the distance between electron i and electron j.

$|\vec{r}_i - \vec{R}_\alpha|$ is the distance between electron i and nucleus α.

$|\vec{R}_\alpha - \vec{R}_\beta|$ is the distance between nucleus α and nucleus β.

Schrödinger equation, which is an eigen-values equation, is given by:

$$H\,\psi\,(\{r_i\},\{R_\alpha\}) = E\,\psi\,(\{r_i\},\{R_\alpha\}) \tag{2.3}$$

where H is the Hamiltonian, ψ presents the wave function, and E is the energy of the system. This Hamiltonian can be solved analytically for simple systems such as one-body or two-body problem and the wave functions of the system can be determined. Three-body can be solved to some extent but not quite accurately. However, it is impossible to solve it for N-body system where N is more than 3, and it requires approximation.

2.2. Born-Oppenheimer Approximation

Born Oppenheimer approximation was the first approximation to simplify the Hamiltonian. It stated that as the mass of a proton is about 2000 times of the electron, which make the electron moves faster than nuclei in response to external perturbations, the dynamics of nuclei and the electrons can be separated, and their wave function can be decoupled,

$$\psi\,(\{r_i\},\{R_\alpha\}) = \psi_e(r_i) * \psi_N(R_\alpha) \tag{2.4}$$

where $\psi_e(r_i)$ is the electronic wavefunction, and $\psi_N(R_\alpha)$ is the nuclei wavefunction. Now, from the total Hamiltonian which is given by equation (2.2) we can first solve the electronic Hamiltonian:

$$H_e = -\frac{\hbar^2}{2m}\sum_i \nabla_i^2 + \frac{1}{2}\sum_{i\neq j}\frac{e^2}{4\pi\epsilon_0|\vec{r}_i - \vec{r}_j|} + \frac{1}{2}\sum_{i,\alpha}\frac{Z_\alpha e^2}{4\pi\epsilon_0\,|\vec{r}_i - \vec{R}_\alpha|} \tag{2.5}$$

where the first term is the electron kinetic energy, second term is electron-electron interaction, and the last term is electron-nuclei interaction. The nucleus part will be calculated separately and will be added to the total energy after the electron Hamiltonian is calculated.

Now, the electronic Hamiltonian is given by

$$H_e = [T_e + V_{ee} + V_{ext}] \tag{2.6}$$

Thus, Schrödinger equation can be written as

$$H_e\,\psi(r_1, r_2, \ldots, r_N) = [T_e + V_{ee} + V_{ext}]\,\psi = E\,\psi \tag{2.7}$$

where $E = \langle \psi \mid H_e \mid \psi \rangle$ (2.8)

Solving this Schrodinger equation is impractical for large numbers of electrons, such as N number where there are 3N degrees of freedom. For example, a simple system such as water molecule, H_2O, has 10 electrons with three spatial coordinates per electron, Schrodinger equation then becomes a 30 variables equation, 30 degrees of freedom. Hence, it is important to find quantum mechanical approaches to solve this kind of many electronic Hamiltonian. The most common quantum mechanical approach to solve N-body problem is to start with Hartree-Fock method, then leading to and density functional theory.

2.3. Hartree-Fock Method

Hartree-Fock method deals with the wavefunction and with 3N degrees of freedom. Hartree-Fock is a simple theory that does not consider the electron correlations, and that makes this theory easy to start with. The advantage of Hartree-Fock theory is that the Fock part that calculates the exchange interaction exactly. Here, we will discuss the Hartree approximation as it will be used in Kohn-Sham Hamiltonian of the DFT Theory, which will be discussed later in details.

2.3.1. Mean Field Approximation (Hartree Approximation)

The simplest starting point of N-electrons system is to consider the noninteracting electrons. Hartree considers the electron-electron interaction as mean field interaction, which means one electron experiences the effective electric field or coulomb field that is created by the rest of the electrons. It is kind of one electron vs. electron's cloud interaction. The electron does not depend on the other electrons explicitly rather the created average field by other electrons [99, 100]. Thus, the Hamiltonian can be given as a sum of single Hamiltonian for each individual electron: $H = \sum_{i=1}^{N} h(i)$ (2.9)

where $h(i)$ is the kinetic energy and the potential of one electron. The $h(i)$ is an effective one electron Hamiltonian that include the effect of electron-electron repulsion in an average way [100].

As because H is a sum of one electrons Hamiltonian, the total wave function, ψ^H, is a simple product of single-electron's wave functions, $\psi_i(r_i)$, is given by:

$$\psi^H(r_1, r_2, r_3, \dots., r_n) = \psi_1(r_1)\psi_2(r_2) \dots \psi_N(r_N) \tag{2.10}$$

The ψ^H is called Hartree product. Here, the many body wavefunction turned into a Hartree product, with $\psi_i(r_i)$ is the i'th electrons wavefunction.

Hence,

$$H\psi^H = E\psi^H \tag{2.11}$$

where $E = \varepsilon_1 + \varepsilon_2 + \varepsilon_3 + \cdots . + \varepsilon_N$ (2.12)

E is the sum of single-particle energy eigenvalues , ε_i, of Hamiltonian in equation (2.9) [100].

Now, the electron-electron interaction in the electronic Hamiltonian equation will be replaced by the Hartree mean field potential as the following:

$$\frac{1}{2}\sum_{i \neq j} \frac{1}{|\vec{r}_i - \vec{r}_j|} \rightarrow \frac{1}{2}\int d^3r' \frac{\rho(r')}{|\vec{r}_i - \vec{r}\,'|} \tag{2.13}$$

Thus, the electronic Hamiltonian of a single electron is given by:

$$H_i = -\frac{\hbar^2}{2m}\nabla_i^2 + \frac{1}{2}\frac{1}{4\pi\epsilon_0}\int d^3r' \frac{\rho(r')}{|\vec{r}_i - \vec{r}\,'|} + \frac{1}{2}\sum_\alpha \frac{Z_\alpha e^2}{4\pi\epsilon_0\,|\vec{r}_i - \vec{R}_\alpha|} \tag{2.14}$$

Our computational work is based on density functional theory, so in the following the fundamentals of density functional theory is introduced.

2.4. Density Functional Theory

Density Functional Theory solves N-body system by the ground state electron density instead of the wave function [95, 101, 102]. It will reduce the problem from 3N degrees of freedoms to 3 degrees of freedoms.

2.4.1. Thomas-Fermi Model

The idea of Thomas-Fermi theory was to determine the ground state energy as a function of the electron density instead of wave-function.

To handle many-electron systems, in 1927, Thomas stated the first assumption that says the electrons are distributed uniformly in the six-dimensional phase space with two electrons at each of the smallest unit cell, and there is an effective field which is determined by the nuclear charge and the distribution of electrons[103-105]. Within this formalism, the total kinetic energy is given by

$$T_{TF}[\rho(r)] = C_F \int \rho^{5/3}(r)\,dr \tag{2.15}$$

where C_F is a constant that equal 2.871.

Thomas-Fermi determined the expression for the total energy of the N-electrons system as a function of electron density $E_{TF}[\rho(r)]$ is given by

$$E_{TF}[\rho(r)] = C_F \int \rho^{5/3}(r)dr + \int \rho(r)\,V_{ext}(r)\,dr + \frac{1}{2}\iint \frac{\rho(r_1)\rho(r_2)}{|r_1 - r_2|} dr_1 dr_2 \tag{2.16}$$

Due the assumption of homogeneous electron gas, Thomas-Fermi method fails to predict most of properties of many-body system such as bound states of atomic systems. Hence, it is important to go beyond this theory. In the following, we will present the DFT with the Hohenberg-

Kohn (HK) theorems which was published in 1965 [106], and the effective algorithm for calculations that was provided by Kohn and Sham[107].

2.4.2. First Hohenberg-Kohn Theorem

Hohenberg-Kohn proved that all observable properties in any system can be determined by its ground state electron density [103]. They stated in the first theorem that the ground state energy is a unique functional of the ground state electron density $\rho(r)$:

$$E[\rho(r)] = T_e[\rho(r)] + V_{ee}[\rho(r)] + \int \mathrm{d}^3r\, V_{ext}(r)\rho(r) \tag{2.17}$$

where $T_e[\rho(r)]$ is the electron kinetic energy, $V_{ee}[\rho(r)]$ is electron-electron interaction and the last term is electron-nuclei interaction. We can rewrite the expression for the total energy in the following manner

$$E[\rho(r)] = F[\rho(r)] + \int \mathrm{d}^3r\, V_{ext}(r)\rho(r) \tag{2.18}$$

Where $F[\rho(r)] = T_e[\rho(r)] + V_{ee}[\rho(r)]$ (2.19)

$F[\rho(r)]$ is a universal functional in the sense that it does not depend on $V_{ext}(r)$. The universal functional means its analytical form is same for any material but the value change depending on the electron density of the material.

It stated in the first theorem that between the external potential and the ground state electron density there exists a one-to-one correspondence.

Proof:

Assume two potentials U and U', each gives same electron density for the ground state of a system. Then, there will be two Hamiltonians H and H' where the ground state electron densities were same although the normalized wave functions ψ and ψ' would be different.

Consider ψ' as a trial function for H, using the variational principle for the ground state $E_0 \leq E$ where E is the expectation value of the Hamiltonian H with respect to the wave function ψ', Then,

$$E_0 \leq E = <\psi' |H |\psi'> = <\psi' |H' |\psi'> + <\psi' |H - H' |\psi'> \qquad (2.20)$$

[rewrite H in this way $H = H' + H - H'$] where $H = T + U(r)$ (2.21)

$$E_0 \leq E = E'_0 + <\psi' |T + U(r) |\psi'> - (<\psi' |T + U'(r) |\psi'>) \qquad (2.22)$$

$$\because <\psi' |\psi'> = \int \psi'^*(r)\, \psi'(r)\, dr = \int |\psi'(r)|^2\, dr \qquad (2.23)$$

and $|\psi'(r)|^2 = \rho(r)$ (2.24)

$$\rightarrow <\psi' |\psi'> = \int \rho(r)\, dr \qquad (2.25)$$

$\because <\psi' |U(r) |\psi'> = \int U(r)\, \rho(r)\, dr$ and $<\psi' |U'(r) |\psi'> = \int U'(r)\, \rho(r)\, dr$ (2.26)

$$\rightarrow E_0 \leq <\psi' |H |\psi'> = E'_0 + \int \rho(r)\, [U(r) - U'(r)] dr \qquad (2.27)$$

Similarly taking ψ as a trial function for H',

$$E'_0 \leq <\psi |H' |\psi> = <\psi |H |\psi> + <\psi |H' - H |\psi> \qquad (2.28)$$

$$E'_0 \leq <\psi |H' |\psi> = E_0 - \int \rho(r)\, [U(r) - U'(r)] dr \qquad (2.29)$$

Adding equation (2.27) and (2.29):

$$E_0 + E'_0 \leq E'_0 + E_0 \qquad (2.30)$$

It is contradiction and thus there cannot be two different U that give same electron density for their ground states [94]. Hence U is a unique functional of the ground state electron density of the system.

2.4.3. Second Hohenberg-Kohn Theorem

The electron density which minimizes the energy functional is the true ground state electron density [94]:

$$E\, [\rho(r)] \geq E_0\, [\rho_0(r)] \qquad (2.31)$$

which means any electron density other than the ground state electron density will give higher energy. This is similar to the variational principle for wave function:

$< H > = < \psi \; |H \; |\psi > \geq E_0$ (2.32)

Where $E_0 = \; < \psi_0 \; |H \; |\psi_0 >$, and $\rho_0(r) = |\psi_0(r)\;|^2$ (2.33)

Proof of second theorem [108]:

To calculate the ground state energy E_0 , using variational principle where the expectation value of H with respect to any trial wave function is greater than or can be equal to E_0:

$E_0 \leq \; < \psi \; |H \; |\psi > \; \equiv \; < H >$ (2.34)

where $|\psi\rangle$ is a trial wave function and can be given by the linear combination of basis functions ψ_n:

$\psi = \sum_n C_n \psi_n$ where $H \, \psi_n = E_n \psi_n$ (2.35)

$1 = < \psi \; |\psi > \; = \; < \sum_m C_m \psi_m \; | \sum_n C_n \psi_n > \; = \sum_n \; |C_n\;|^2$ (2.36)

Here, the orthogonality of the basis functions was used: $< \psi_m \; |\psi_n > = \; \delta_{mn} = 1$ if n = m, otherwise 0. The C_n are the coefficients of the linear expansion, are in general complex numbers. From equation (2.34):

$< H > \; = \; < \sum_m C_m \psi_m \; |H \; | \sum_n C_n \psi_n > \; = \sum_m \sum_n C^*{}_m E_n C_n < \psi_m \; |\psi_n >$ (2.37)

$< H > \; = \sum_n E_n \; |C_n\;|^2$ (2.38)

Where the ground state energy is the smallest eigen value, so $E_n \geq E_0$

Hence, $< H > \; \geq E_0 \sum_n \; |C_n\;|^2 = E_0$ (2.39)

With the two Hohenberg-Kohn theorems, we can see that the foundation of density functional theory has been stablished and that DFT has a valid mathematical foundation. The ground state electron density is the central quantity in density functional theory from where we can derive all the ground state properties of a system. The universal functional is comprised of kinetic energy and electron-electron interactions.

Now, it is important to show the implementation of DFT which will also lead us to some approximation for the universal functional.

2.4.4. Kohn-Sham Formalism

One of the ways to implement DFT for computation is by Kohn-Sham formalism which is the most used formalism in present days. The idea is to map many-body interacting system into a system of non-interacting particles with the same ground state electron density $\rho(r)$ as the many-particles system as shown in Figure 2.1.

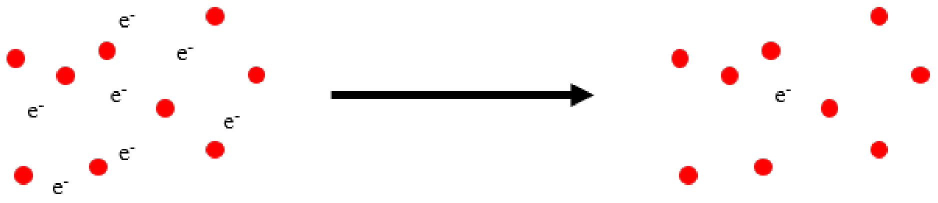

(a) (b)

Figure 2.1. (a) interacting electrons in a real external potential: $H = T_e + V_{ee} + V_{ext}$ and (b) A set of non-interacting electrons (with the same density as the interacting system) in some effective potential.

Kohn-Sham proposed that with the same ground state electron density $\rho(r)$, N-body interacting system can be replaced by a system of non-interacting particles to simplify the system and get an idea about the form of the functional. Kohn-Sham assumed this can be done for any system because it is known that each material will be represented by different nuclei from other material which generate the external potential. It is known from Hohenberg-Kohn theorem when the external potential is changed, the electron density will be changed. Hence, Kohn-Sham stated that the electron density is same for both systems because external potential is not changing. Even though we are modeling interacting system vs. non-interacting system, the electron density is same by H-K theorem because it is same physical system.

From our previous electronic Hamiltonian, we are now dealing with these terms:

$$H_e = -\frac{\hbar^2}{2m}\sum_i \nabla_i^2 + \frac{1}{2}\sum_{i\neq j}\frac{e^2}{4\pi\epsilon_0|\vec{r}_i - \vec{r}_j|} + \frac{1}{2}\sum_{i,\alpha}\frac{Z_\alpha e^2}{4\pi\epsilon_0\,|\vec{r}_i - \vec{R}_\alpha|} \qquad (2.40)$$

Kohn-Sham Formalism takes the concept of Hartree method where it considers the system as non-interacting electrons. However, in real system, there are interactions between the electrons, so to compensate Kohn-Sham Formalism includes the exchange-correlation term.

Thus, the electronic Hamiltonian of a single electron of Kohn-Sham is given by:

$$H_s = T_s[\rho(r)] + \frac{1}{2}\int d^3r'\,\frac{\rho(r')}{|\vec{r}_i - \vec{r}\,'|} + H_{xc}[\rho(r)] + \int \mathrm{d}^3r\, V_{ext}(r)\rho(r) \qquad (2.41)$$

where we set $\hbar = 1$, $\frac{1}{4\pi\epsilon_0} = 1$ using natural units for simplicity.

where $T_s[\rho(r)] + \frac{1}{2}\int d^3r'\,\frac{\rho(r')}{|\vec{r}_i - \vec{r}\,'|}$ is non-interacting electron kinetic energy and non-interacting mean field potential. $H_{xc}[\rho(r)]$ will be whatever that are not included in independent particle model as exchange-correlation term, and last term $\int \mathrm{d}^3r\, V_{ext}(r)\rho(r)$ is the external potential. The $H_{xc}[\rho(r)]$ is given by:

$$H_{xc}[\rho(r)] = H_x + H_c = H_x + T_{e-e\,\text{interaction}} + V_{e-e\,interaction} \qquad (2.42)$$

where we know that $T_e[\rho(r)] = T_s + T_{e-e\,\text{interaction}}$ (2.43)

and $V_e[\rho(r)] = \frac{1}{2}\int d^3r'\,\frac{\rho(r')}{|\vec{r} - \vec{r}\,'|} + V_{e-e\,interaction}$ (2.44)

where $T_{e-e\,\text{interaction}} + V_{e-e\,interaction}$ are the kinetic energy and potential due to the electron-electron interaction which are not considered in the independent particle model.

In addition, $H_{xc}[\rho(r)]$ includes spin-spin interaction that follow Pauli exclusion principle where it says there cannot be two electrons in same orbital with same spin.

Now, Kohn-Sham formalism reduces the problem from the total universal functional to exchange-correlation term only and now E_{xc} needs some approximation which we will be discussed later in this chapter.

Hence, the universal functional is given by

$$F[\rho(r)] = T_s[\rho(r)] + \frac{1}{2}\int d^3r' \frac{\rho(r\prime)}{|\vec{r}_i - \vec{r}\,'|} + E_{xc}[\rho(r)] \tag{2.45}$$

and the energy functional is given by

$$E[\rho(r)] = T_s[\rho(r)] + \frac{1}{2}\int d^3r' \frac{\rho(r\prime)}{|\vec{r}_i - \vec{r}\,'|} + \int \mathrm{d}^3r\, V_{ext}(r)\rho(r) + E_{xc}[\rho(r)] \tag{2.46}$$

Now, by applying the variational principle:

$$\delta E[\rho(r)] = 0$$

and by minimizing the energy functional with respect to the electron density, the chemical potential can be given by

$$\mu = \frac{\delta E[\rho(r)]}{\delta\rho(r)} \tag{2.47}$$

$$\mu = \frac{\delta T_s[\rho]}{\delta\rho(r)} + \frac{\delta}{\delta\rho(r)}[\frac{1}{2}\int d^3r' \frac{\rho(r')}{\left|\vec{r}_i - \vec{r}\,'\right|} + \int \mathrm{d}^3r\, V_{ext}(r)\rho(r)] + \frac{\delta E_{xc}[\rho]}{\delta\rho(r)} \tag{2.48}$$

$$\mu = \frac{\delta T_s[\rho]}{\delta\rho(r)} + V_{eff} \tag{2.49}$$

where $V_{eff}(r)$ is the Kohn-Sham effective potential [94], and it is given by

$$V_{eff} = V_{ext} + \frac{1}{2}\int d^3r' \frac{\rho(r\prime)}{|\vec{r}_i - \vec{r}\,'|} + V_{xc}[\rho(r)] \tag{2.50}$$

where $V_{xc}[\rho(r)] = \frac{\delta E_{xc}[\rho(r)]}{\delta\rho(r)}$ (2.51)

Now, with this the effective potential, N-body problem becomes a one-body problem where one particle effective Hamiltonian is given by

$$H_{eff} = -\frac{1}{2}\nabla^2 + V_{eff} \tag{2.52}$$

And Kohn-Sham of single particle equation is given by

$$\left[-\frac{1}{2}\nabla^2 + V_{eff}(r)\right]\psi_i = \varepsilon_i\,\psi_i \tag{2.53}$$

where $\psi_i$is the Kohn-Sham eigen-functions and ε_i is the energy eigenvalues. By solving Kohn-Sham equation, electron density can be calculated by

$$\rho(r) = \sum_i^N |\psi_i(r)\,|^2: \tag{2.54}$$

Finally, the kinetic energy $T_s[\rho]$ can be obtained by the following equation:

$$T_s[\rho] = \frac{1}{2}\sum_{i=1}^N < \psi_i\left|\nabla_i^2\right|\psi_i > = \sum_{i=1}^N \varepsilon_i - \int d^3r'\ V_{eff}\rho(r) \tag{2.55}$$

Kohn-Sham method is a simple and powerful method that considers the exchange correlation effects and includes it in the energy [94] which will help to obtain the ground state properties of many body systems in proper way.

The only term which needs to be approximated is the exchange-correlation energy functional, $E_{xc}[\rho(r)]$, and there are some approximations which is used to calculate the total energy of many-body system within the DFT framework.

2.5. Exchange Correlation Energy $\mathrm{E}_{xc}[\boldsymbol{\rho}]$

The most usful approximations to the Exchange Correlation Energy $\mathrm{E}_{xc}[\rho]$ are the Local Density Approximation (LDA), Generalized Gradient Approximation (GGA), and Hybrid functionals.

2.5.1. Local Density Approximation (LDA)

LDA assumes the exchange-correlation energy functional is purely local and it is derived from homogenous electron gas. The exchange-correlation energy functional is given by

$$E_{xc}^{LDA}[\rho] = \int d^3r\,\rho(r)\,\varepsilon_{xc}(\rho) \tag{2.56}$$

The exchange-correlation energy functional divided into two terms as the following equation,

$$E_{xc}^{LDA}[\rho(r)] = E_x[\rho(r)] + E_c[\rho(r)] \tag{2.57}$$

where the first term $E_x[\rho(r)]$ is the exchange energy, and the second term $E_c[\rho(r)]$ is the correlation energy [109].

2.5.2. Local Spin Density Approximation (LSDA)

It is similar to local density approximation, but the spin density is separated to spin-up and spin-down [103, 110] densities, LSDA equation is written as

$$E_{xc}^{LDA}[\rho(r)] = \int d^3r\, \varepsilon_{xc}[\rho \uparrow (r), \rho \downarrow (r)] \tag{2.58}$$

Local density approximation can be used to determine the vibrational properties and the ground state geometries; however, the lattice parameters are usually smaller than what are expected, and it underestimates the band gap of semiconductor materials.

2.5.3. Generalized Gradient Approximation (GGA)

As we know that any real system is an inhomogeneous system that has a varying density $\rho(r)$. GGA includes information of the variation of electronic density in the functional. The exchange-correlation energy functional depends on both electronic density $\rho(r)$ and on its gradient $\nabla\rho$ [94, 111-113].

$$E_{xc}^{GGA}[\rho(r)] = \int d^3r\, \varepsilon_{xc}[\rho(r), \nabla\rho(r)] \tag{2.59}$$

where the functional forms of $\varepsilon_{xc}[\rho(r), \nabla\rho(r)]$ can be developed through parameter fitting to experimental data. However, PW GGA functional [112], which works well for many properties of the exact E_{XC} fails to provide better results in homogeneous systems comparing to LSDA [110, 114, 115]. The calculations in this dissertation employ the parameterization of Perdew-Burke-Ernzerhof (GGA-PBE) [113]. GGA-PBE provide better energies and structure geometries than LSDA [113]. However, like the LDA functional, the GGA functionals are also known to underestimate band gaps of semiconductors.

2.5.4. Hybrid Functional

As mentioned above that LDA and GGA functionals underestimate the fundamental band gaps of semiconductors. In Kohn-Sham theory, the electrons will encounter coulombic interaction via a mean-field electronic density which gives self-interaction energy errors [116]. This kind of errors will delocalize the electrons [117], particularly in highly correlated transition metal systems. To overcome this problem, adiabatic connection approximation [118] can be applied by including some amount of Hartree-Fock exact exchange.

Hybrid functionals mix a portion of exact exchange from Hartree-Fock theory to the DFT exchange and correlation functional. Hybrid functionals improve description of the lattice constants, surface energies, and band gaps of semiconductors and insulators. The hybrid functional we used for our computation is Heyd-Scuseria-Ernzerhof functional (HSE06) [119-122]. In HSE, the spatial decay of the HF exchange interaction is accelerated by substitution of the full 1/r Coulomb potential with a screened one. The HSE functional partitions the Coulomb potential for exchange into two components, short range (SR) and long range (LR) components:

$$\frac{1}{r} = \frac{1-erf(\omega r)}{r} + \frac{erf(\omega r)}{r} \tag{2.60}$$

where $\frac{1-erf(\omega r)}{r}$ is SR and $\frac{erf(\omega r)}{r}$ is LR components.

The exchange-correlation energy is then calculated as

$$E_{xc}^{HSE} = aE_x^{HF,SR}(\omega) + (1-a)E_x^{PBE,SR}(\omega) + E_x^{PBE,LR} + E_c^{PBE} \tag{2.61}$$

where ω is the screening parameter that defines the separation range, $E_x^{HF,SR}$ is the short-range HF exchange, $E_x^{PBE,SR}$, $E_x^{PBE,LR}$ are the short-range and long-range components of the PBE respectively, and the parameter a is the HF mixing constant and the standard value of it is 0.25.

The flow chart of the DFT self-consistent Kohn-Sham loop is given by Figure 2.2.

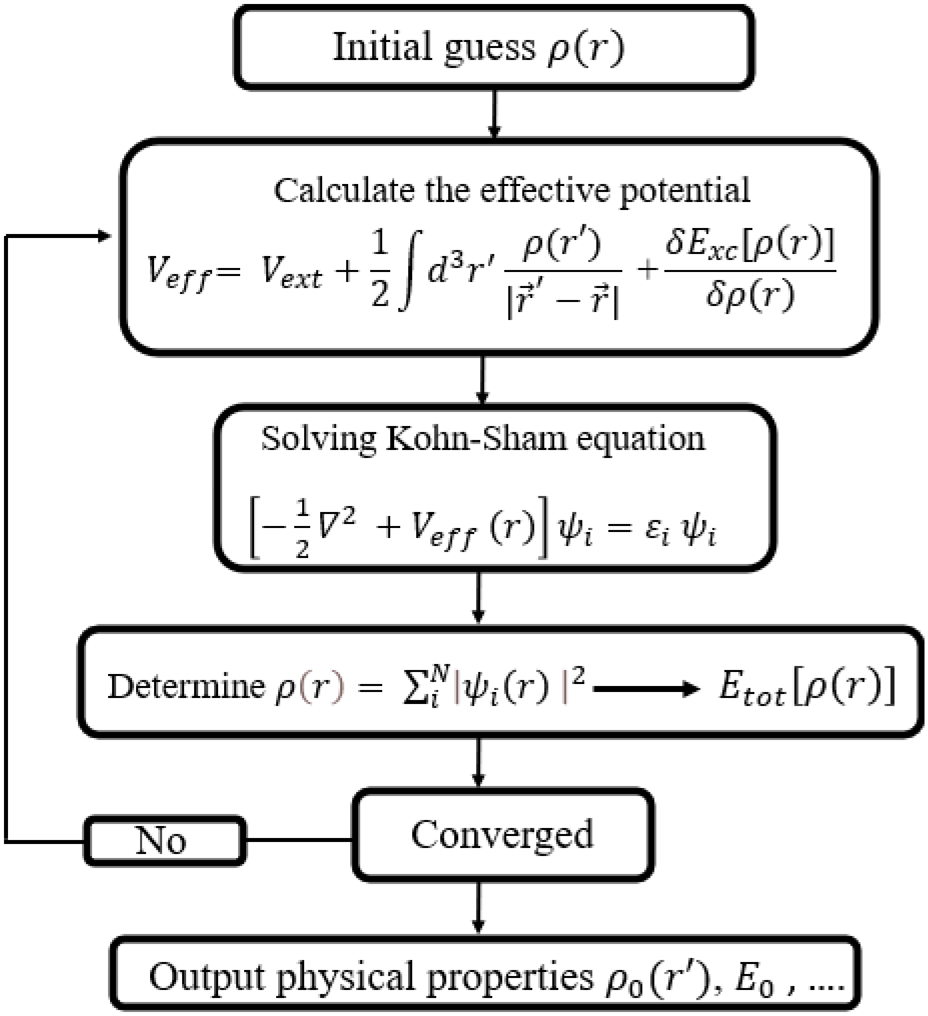

Figure 2.2. The flow chart of the DFT self-consistent Kohn-Sham loop.

Chapter 3

Copper Cysteamine with Halogens (Cu-Cy-X)

3.1. Computational Method

The calculations were done within the framework of density functional theory (DFT) as implemented in Vienna ab initio simulation package (VASP) [123, 124]. Projector augmented wave method (PAW) [125, 126] was utilized. Generalized gradient approximation (GGA) [113], which calls the Perdew–Burke–Ernzerhof (PBE) [127] as an exchange-correlation functional was used. The Heyd–Scuseria–Ernzerhof (HSE06) hybrid function [120] has been utilized on the systems to determine accurate information about the lowest state of each spin symmetry, S_0 and T_1 for the singlet and triplet state, respectively. The calculations of this work were spin polarized, and the convergence criteria which is the global break condition for the electronic self-consistent loop was 10^{-06} eV for Hybrid and GGA calculations. The cut-off energy for plane wave basis set was 500 eV, and the condition to break the ionic relaxation loop was -0.01 eV/Å. We used VESTA (visualization for electronic and structural analysis) to visualize all the crystal structures before and after the relaxation and to make the vacancies in the structures [128]. We used different denser K-point meshes [129] taking the size of the cell into account where higher denser K-point meshes are used to calculate the total energies. The tetrahedron method is used to obtain total energy as well for density of states (DOS) calculations [129].

We included the Van der Waals interactions [130-136] for proper structural relaxations and total energy calculations. VDW is needed because the inter-layer interactions are weak which is Van der Waals type. Also, it is important to include Van der Waals forces with the DFT Hamiltonian because we have molecular solid which means a unit of the solid behave as if it is molecule and the Cu-Cy formulae unit by itself behaves like a molecule.

Formation enthalpies were calculated to examine the stability of the structures thermodynamically by following formula:

$$\Delta H_f\left(A_iB_jC_kD_lE_mF_n\right) = E_{total}\left(A_iB_jC_kD_lE_mF_n\right) - i\,E(A) - j\,E(B) - k\,E(C) - l\,E(D) - m\,E(E) - n\,E(F) \quad (3.1)$$

Where A, B, C, D, E and F present the elements and i, j, k, l, m and n present the total number of atoms, respectively.

where ΔH_f is the formation enthalpy, E_{total} is the total energy of the pristine structure, $E(A)$ present the energy per atom of element A in its ground state (bulk) phase.

For example, the formation enthalpy of Cu-Cy-Br ($C_8Br_2Cu_6H_{24}N_4S_4$) can be calculated by the following equation

$$\Delta H_f(\mathrm{C_8Br_2Cu_6H_{24}N_4S_4}) = E_{prisitne}(\mathrm{C_8Br_2Cu_6H_{24}N_4S_4}) - 8E(C) - 2E(Br) - 6E(Cu) - 24E(H) - 4E(N) - 4E(S) \quad (3.2)$$

A negative number of the formation enthalpy will imply a thermodynamically stable configuration where the more negative a binding energy is, the more stable a structure is.

We have calculated the defect formation energy [137, 138] of the Cu-vacancy (Cu_v) and X_v in Cu-Cy-X structures using the following equation

$$E_f(\mathrm{Cu}_v) = E(\mathrm{Cu}_v) - E_{tot} + E(\mathrm{Cu}_{atom}) + \Delta\mu_{\mathrm{Cu}} \quad (3.3)$$

Where $E_f(\mathrm{Cu}_v)$ is the defect formation energy of Cu-vacancy, $E(\mathrm{Cu}_v)$ presents the total energy when we make the Cu-vacancy in the pristine Cu-Cy-X structure, $E(\mathrm{Cu}_{atom})$ is the energy per atom of Cu in its elemental ground state (bulk) phase, and $\Delta\mu_{\mathrm{Cu}}$ the chemical potential which can be determined by the following conditions:

$$\Delta\mu_{\mathrm{Cu}} = 0 \text{ at Cu-rich condition} \quad (3.4)$$

$$\Delta\mu_{\mathrm{Cu}} = \frac{\Delta H_f}{6} \text{ at Cu-poor condition} \quad (3.5)$$

where ΔH_f is the formation enthalpy which is calculated by equation 3.1.

Chemical potential defines as if we have N-particles, and if we want to take out one particle, then how much energy needs to take it out of the system is called as chemical potential.

The optical absorption has been calculated for all Cu-Cy-X using the frequency dependent complex dielectric function $\varepsilon(\omega) = \varepsilon_1(\omega) + i\,\varepsilon_2(\omega)$ which is calculated in the independent particle picture using VASP. ε_1 and ε_2 are the real and imaginary parts respectively, and ω is the frequency of the incident photon [139-141].

Bader charge analyses are performed using the code which is provided by the Henkelman group [142-146]

Bader net charge Q_{net} is defined as

$$Q_{net} = Q_{VASP} - Q_{Bader} \tag{3.6}$$

where Q_{VASP} is the valence charge which considered in the calculation, and Q_{Bader} is the calculated Bader atomic charge. Q_{net} can help to estimate the oxidation states of the atoms.

3.2. Results and Discussion

3.2.1. Derived Smaller Unit Cell of Cu-Cy-Cl from the Super Cell of Cu-Cy-Cl

The theoretical work in this dissertation mostly done with smaller unit cell. We derived the smaller unit cell of Cu-Cy-Cl from the super cell of Cu-Cy which are from XRD where both super cell and unit cell are monoclinic structures. Figure 3.1 presents Cu-Cy structure where (a) is the super cell of Cu-Cy-Cl and (b) is the unit cell of Cu-Cy-Cl . Table 3.1 shows the lattice parameters and angels of Cu-Cy-Cl experimentally and theoretically before and after relaxation.

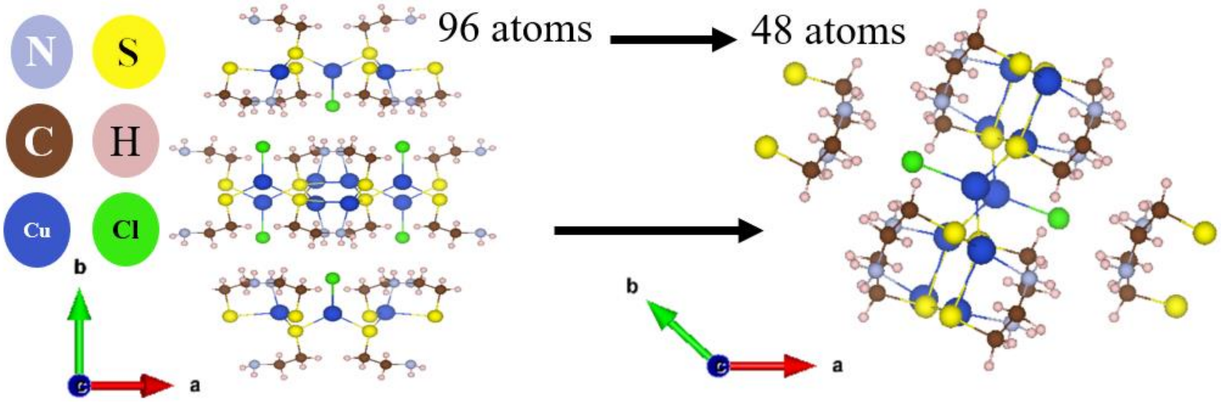

Figure 3.1. Ball and stick representation of the structural unit of the Cu-Cysteamine crystal. (a) super cell of Cu-Cy-Cl and (b) the unit cell of Cu-Cy-Cl . Cl atoms are represented in green, S in yellow, Cu in dark blue, C in brown, N in light blue and H in light pink.

Table 3.1. Lattice parameters and angels of Cu-Cy-Cl experimentally and theoretically before and after relaxation

Singlet	a (Å)	b (Å)	c (Å)	α (°)	β (°)	γ (°)	V (Å^3)
Experimental (super cell)	7.551	16.984	7.836	90	104.798	90	971.701
Experimental (unit cell)	9.293	9.293	7.836	95.955	95.955	132.062	485.847
Theoretical (unit cell)	9.206	9.206	7.683	95.879	95.879	132.037	468.104

3.2.2. Stability of Cu-Cy-X

We have studied the stability of Cu-Cy-X materials theoretically in VASP by considering periodic structures of Cu-Cy-X. Figure 3.2 shows the relaxed structures of (a) Cu-Cy-F, (b) Cu-Cy-Cl, (c) Cu-Cy-Br and (d) Cu-Cy-I where we have 8 atoms of C, 6 atoms of Cu, 24 atoms of H, 4 atoms of N, 4 atoms of Sulfur and 2 atoms of X (X= F, Cl, Br, I). The unit cell shows that there are two different types of Cu atoms Cu (1), which is coordinated by two sulfur atoms and one Cl atom, and the second one called Cu (2), which binds to 4 other atoms in the crystal, three sulfur atoms and one N atom.

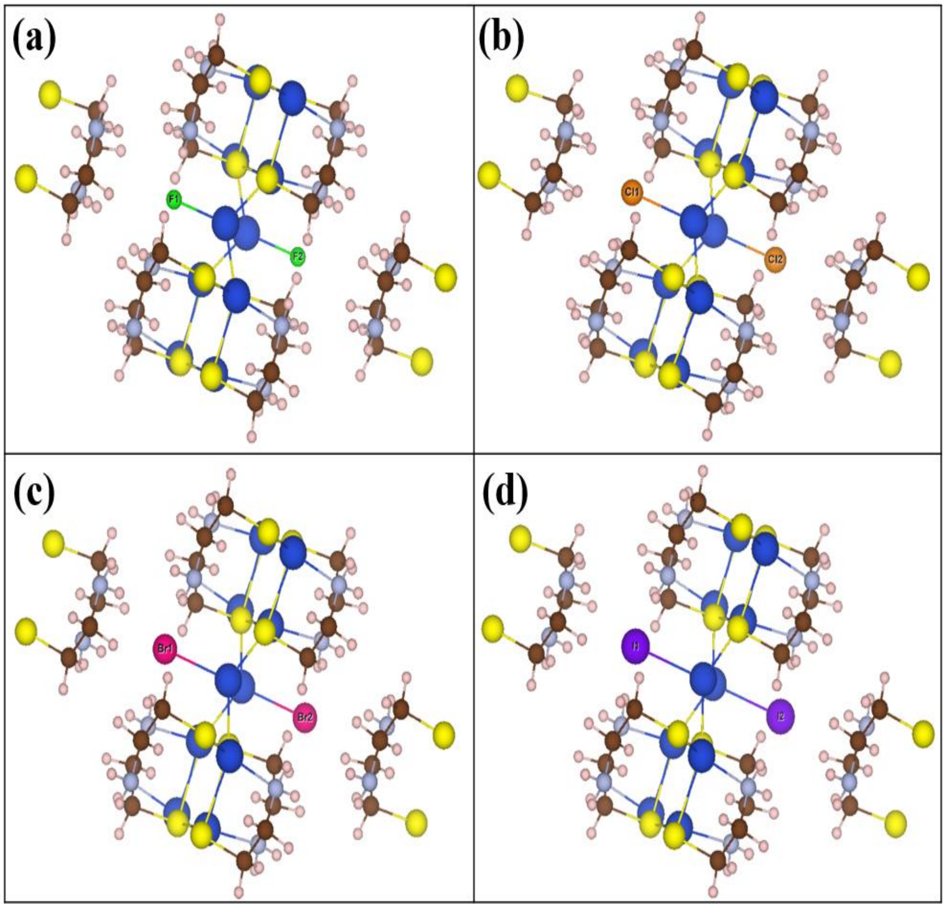

Figure 3.2. Ball and stick representation of the structural unit of the Cu-Cysteamine crystal. (a) Cu-Cy-F, (b) Cu-Cy-Cl, (c) Cu-Cy-Br and (d) Cu-Cy-I. F atoms are represented in green, Cl in orange, Br in dark pink, I in purple, S in yellow, Cu in dark blue, C in brown, N in light blue and H in light pink.

First, we started to relax Cu-Cy-X structures fully using (HSE06) hybrid functional. As because Cu-Cy-X is a molecule, we considered two states called singlet state and triplet state. Singlet state means there is no spin in the system, spin up equals to spin down, so total spin is zero which means all electrons are paired (S = 0).

Oppositely, triplet state means there is spin moment (S =1) where the multiplicity is given by 2S+1.

When the structures are fully relaxed, we obtain the lattice parameters and the volume of the unit cells, as shown in Table 3.2. Our computed data shows the lattice *a* and *b* are equal within each Cu-Cy structure and the lattice parameter *c* is slightly smaller. Also, we can see that Cu-Cy-Cl has the lowest *a* and *b* lattice parameters comparing to the other Cu-Cy structures where Cu-Cy-I has the largest values. Note, that the volume of the unit cell increases from Cu-Cy-F to Cu-Cy-I, implying that the average lattice constants are increasing to accommodate the larger atomic radius of the halogen atoms.

Table 3.2. Lattice parameters and volume of Cu-Cy-X (X= Cl, Br, and I) of singlet states calculated by hybrid functional

Structures	a (Å)	b (Å)	c (Å)	α (°)	β (°)	γ (°)	Volume (Å^3)
Cu-Cy-F	8.85044	8.85044	8.40403	90.9973	90.9973	140.1400	421.36
Cu-Cy-Cl	8.77302	8.77302	8.663382	91.2781	91.2781	137.3480	449.3862
Cu-Cy-Br	8.86266	8.86266	8.74888	91.4066	91.4066	137.1996	465.86
Cu-Cy-I	9.08253	9.08253	8.90052	91.4982	91.4982	137.6545	493.28

After the full relaxation, we obtained the total energy. From the energy differences trend shown in Figure 3.3, it can be infered that the Cu-X bond plays the important role in the spin-state stabilities. The bonds of Cu with the hlogens X (X= Fl, Cl, Br and I) and with Sulfur atoms are listed in Table 3.3. We can see that Cu-F has the shortest bond length comparing to Cu-Cl, Cu-Br, and Cu-I has the longest bond length. This trend is shown in both singlet and triplet states.

Table 3.3. Bond length (Å) of pristine Cu-Cy-X (X= F, Cl, Br, and I) for singlet and triplet states calculated by hybrid functional

Structures	Singlet				Triplet			
	Cu-Cy-F	Cu-Cy-Cl	Cu-Cy-Br	Cu-Cy-I	Cu-Cy-F	Cu-Cy-Cl	Cu-Cy-Br	Cu-Cy-I
Cu-X	2.01238	2.36879	2.52523	2.68460	1.98020	2.33008	2.46485	2.59946
Cu-S(1)	2.20369	2.20334	2.19880	2.20221	2.21114	2.17682	2.17622	2.25876
Cu- S(2)	2.20369	2.20334	2.19880	2.20221	2.21114	2.17682	2.17622	2.25876

The results indicate that for all Cu-Cy-X, singlet state has lower energy which means singlet state is the ground state for all of them. Figure 3.3 shows the difference in the energy between singlet and triplet state for Cu-Cy-X strucutres where we can see the diffrence between singlet and triplet state for Cu-Cy-F structure is 2.668 eV, Cu-Cy-Cl has the highest energy diffrence 2.896 eV, Cu-Cy-Br with difrence 2.838 eV, and 2.306 eV for Cu-Cy-I.

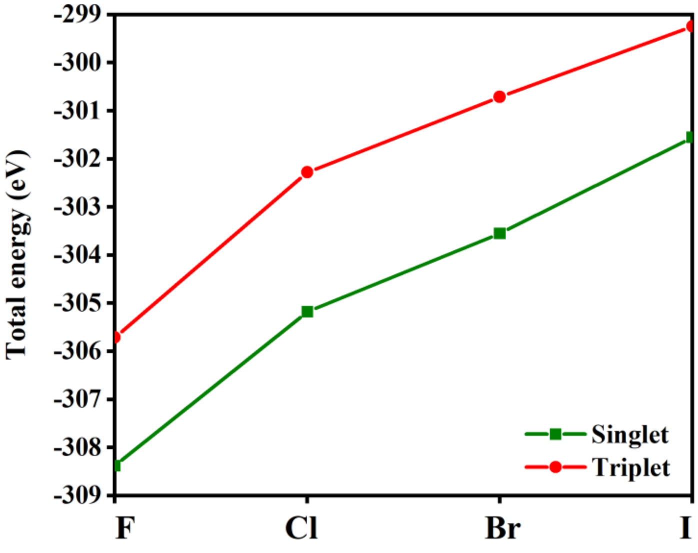

Figure 3.3. Total energy of singlet and triplet state of Cu-Cy-X calculated by hybrid functional.

As because singlet state is the ground state of Cu-Cy-X, we have calculated the formation enthalpies of Cu-Cy-X to compare the stability of all structures. To calculate the formation enthalpies of Cu-Cy-X, total energy of individual elements in their ground state (bulk) phase are calculated using the hybrid functional which is given in Table 3.4.

Table 3.4. Total energy of individual elements in their ground state (bulk) phase calculated by hybrid functional

Element	E/atom (eV)
C	-11.401
S	-6.602
Cu	-3.560
N	-11.433
H	-3.854
I	-3.316
Br	-3.799
F	-5.137
Cl	-4.414

Table 3.5 presents the formation enthalpies of Cu-Cy-X structures singlet state. It can be seen that Cu-Cy-F has the lowest formation enthalpy which means it is the most stable structure

and Cu-Cy-I structure is the least stable one thermodynamically. This can be explained by the electronegativity of the halogen atoms. The higher electronegative atom makes the ionic part bonding stronger, and as because F has the highest electronegativity comparing to Cl, Br and I, the ionic part bonding between Cu and F will be the strongest. On the other hand, the electron donating from Cu to I atom will be less so the ionic part bonding will be weaker, and it will relatively lower the thermodynamic stability.

Table 3.5. Formation enthalpies of Cu-Cy-X structures singlet state calculated by hybrid functional

Structure	ΔH_f (eV)
Cu-Cy-F	-20.903
Cu-Cy-Cl	-19.143
Cu-Cy-Br	-18.747
Cu-Cy-I	-17.716

3.2.3. Density of States

We have calculated the orbital projected partial and total density of states (DOS) using hybrid functional to study electronic and optical properties. Figures 3.4 - 3.11 show the DOS plots for Cu-Cy-X in singlet and triplet state. Here, we will take Cu-Cy-I plots to explain in detail. Figures 3.4 shows the DOS plot of Cu-Cy-I singlet state, we have seen that valence band (VB) has significant contribution from of Cu (1) d-orbital, Cu (2) d-orbital, S p-orbital, and I-p orbital. In the conduction band (CB), the most contributions come from Cu (1), Cu (2) orbital as well as from S p-orbital. Note, that the dominant contributions from Cu (1) and Cu (2) atoms in the conduction band (CB) will help in the non-radiative transition between singlet and triplet state due to spin-orbit coupling. Also, we have seen that S_0 to S_1 transition will be mainly initiated by Cu-3d to S-2p. last point be notice is that the dominant Cu 3d near VB implies a $3d^{10}4s^0$ configuration of S_0 state, which is a Cu^{+1} oxidation state.

Figures 3.5 shows the density of states (DOS) for the triplet (T_1) state of Cu-Cy-I structure. The spin-up and spin-down are presented here explicitly. We can see the top of the valence band is dominated by Cu (1) and Cu (2) s-, p-, and d-orbitals, S s-orbital and p-orbitals as well as I-p orbitals. Also, it is noticeable that there are empty bands from Cu (1), Cu (2) d-orbitals and S p-orbital above the valence band in down spin channel, which was absent in the singlet DOS plot. It confirms T_1 state has a Cu $3d^9 4s^1$ configuration, which implies a Cu^{+1} oxidation state.

Similar behavior is observed in all Cu-Cy-F, Cu-Cy-Cl, and Cu-Cy-Br DOS plots where the most contribution come from Cu (1), Cu (2) s-, p- and d-orbitals and S p-orbital in VB and CB for both singlet and triplet state.

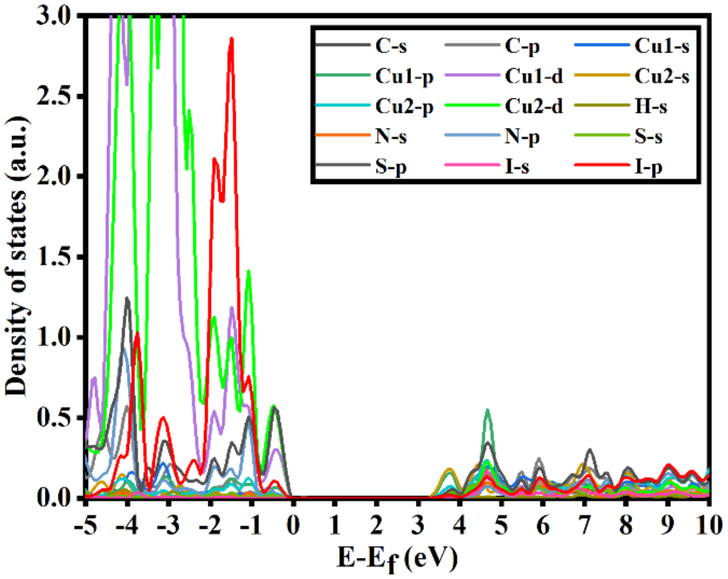

Figure 3.4. Partial density of states of singlet state of Cu-Cy-I calculated with hybrid functional (HSE06). The top of the valence band is scaled to 0 eV, which is called Fermi level. Spin-polarized calculations were performed, but for singlet state (S_0) only spin-up DOS is plotted.

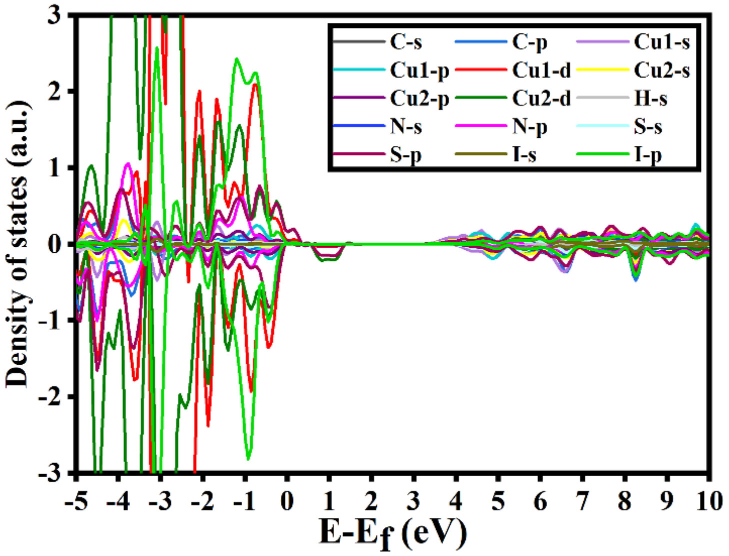

Figure 3.5. Partial density of states of triplet state of Cu-Cy-I calculated with hybrid functional (HSE06). The top of the valence band is scaled to 0 eV which called the Fermi level. The spin-up channel is presented by positive density of states and spin-down channels by the negative density of states.

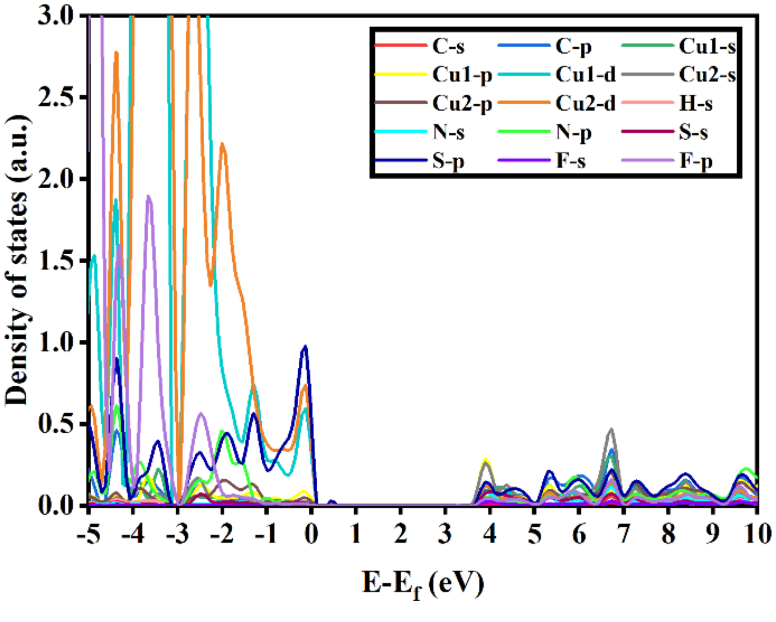

Figure 3.6. Partial density of states of singlet state of Cu-Cy-F calculated with hybrid functional (HSE06).

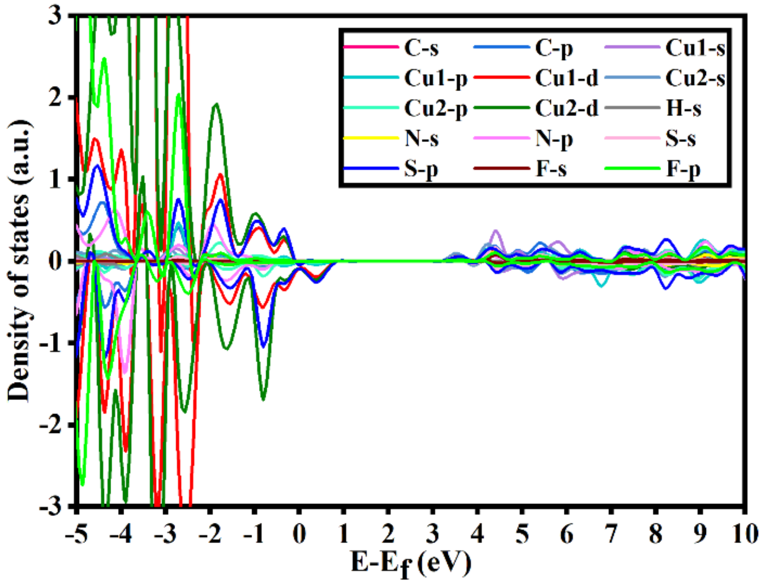

Figure 3.7. Partial density of states of triplet state of Cu-Cy-F calculated with hybrid functional (HSE06).

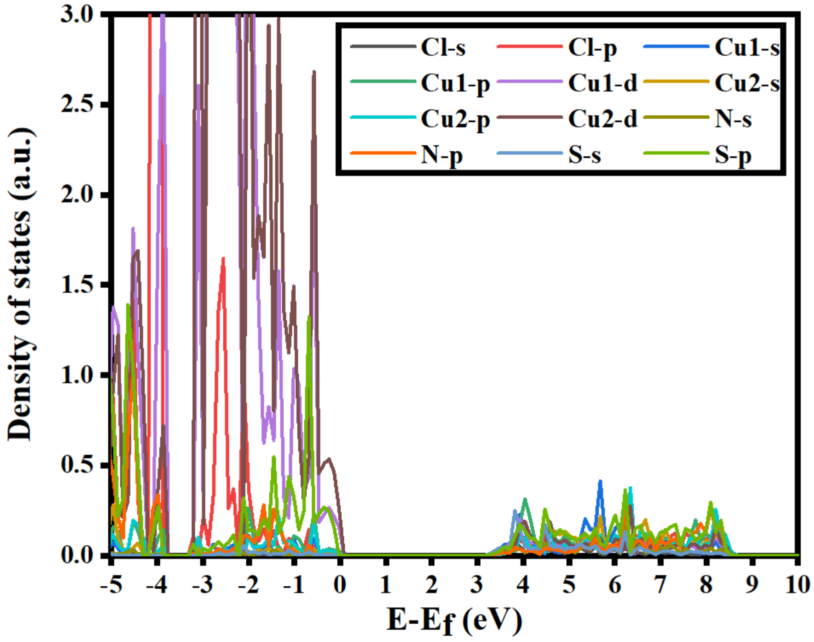

Figure 3.8. Partial density of states of singlet state of Cu-Cy-Cl calculated with hybrid functional (HSE06).

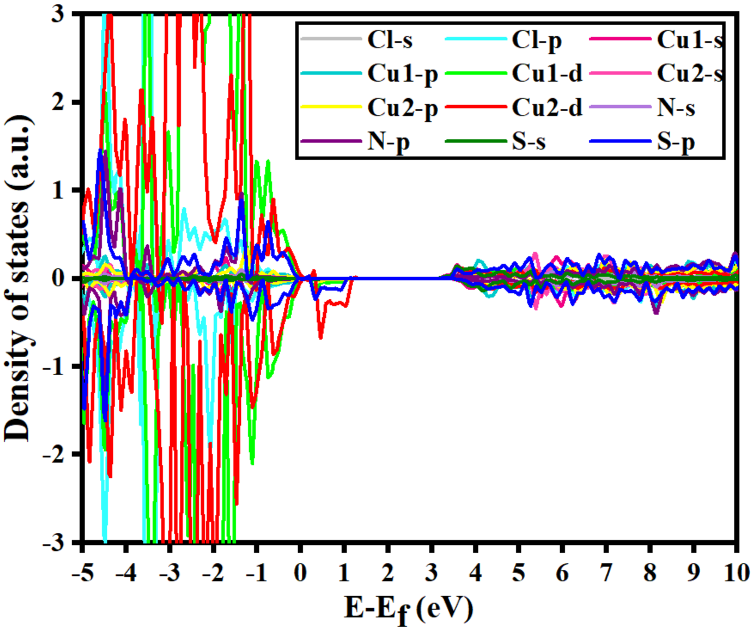

Figure 3.9. Partial density of states of triplet state of Cu-Cy-Cl calculated with hybrid functional (HSE06).

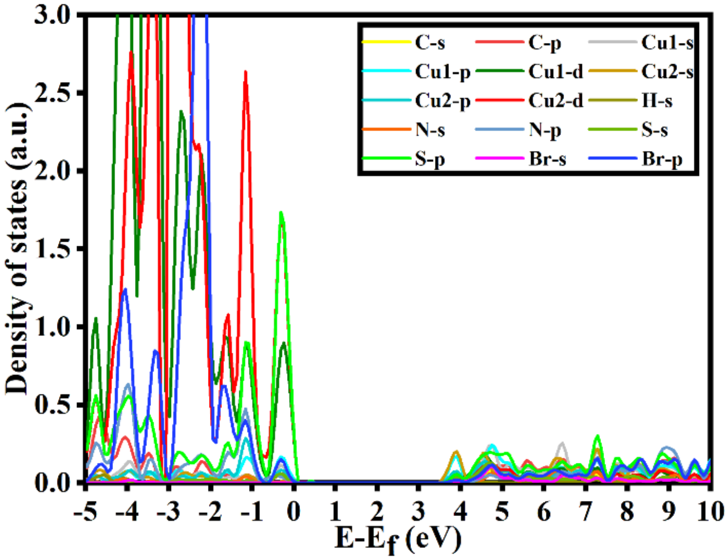

Figure 3.10. Partial density of states of singlet state of Cu-Cy-Br calculated with hybrid functional (HSE06).

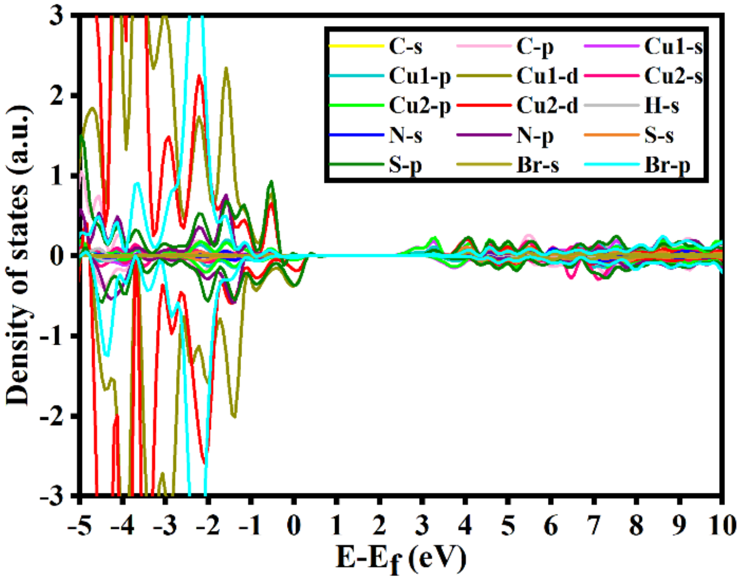

Figure 3.11. Partial density of states of triplet state of Cu-Cy-Br calculated with hybrid functional (HSE06).

Now, we will explain the excitation and deexcitation from total DOS plot for Cu-Cy-Cl shown in Figure 3.12 to understand the optical-emission phenomena that measured experimentally in the lab [147]. First, if the material is not excited by light, the electrons will remain in the singlet state as singlet state is the ground state of all Cu-Cy-X (X= Cl, F, Br, and I). Now, if Cu-Cy-X is activated by light, the electron will be excited from ground state from valance band maxima (VBM) singlet state to conduction band minima (CBM) singlet state by the radiative transition shown in the green arrow. the energy difference within the singlet state (VBM to CBM singlet state) will be the excitation energy. We can see that this excitation energy is around 3.35 eV, from zero to the onset of CB. This excitation energy is matching with onset of the optical plot shown in Figure 3.13. where we can see the absorption starts at around 3.35 eV for Cu-Cy-Cl. This excitation energy is close to the experimental absorption energy 3.42 eV (362 nm).

Then, when the electron is in singlet CB, there will be singlet to triplet transition because triplet has lower energy in up spin channel that can be seen in the CB which is shown in red arrow on the right figure. This transition called non-radiative transition and it requires spin-orbit-coupling (SOC) where with SOC the quantum spin-state is not preserved. Within the SOC, the excited electron in S_1 state non-radiatively transitions into the T_1 state before it is de-excited to the first available lower energy state (T_0 or S_0). It is non-radiative transition because their magnetic moment is different singlet has no spin and triplet has 2 bohr magnetron, and the transition between singlet and triplet state will occur only on Cu cite. Also, SOC will allow flipping in the spin from up spin to down spin within triplet sate. Then, when the electron is in triplet CB down spin channel, it will deexcite (the deexcitation is the emission spectra) to the nearest unoccupied band which is down spin triplet state (T_1-T_0) (the green arrow which is radiative transition) and that is 2.07 eV which is matching with experimental emission. When the electron is in T_0, it might again go back S_0 with non-radiative transition (in the red arrow).

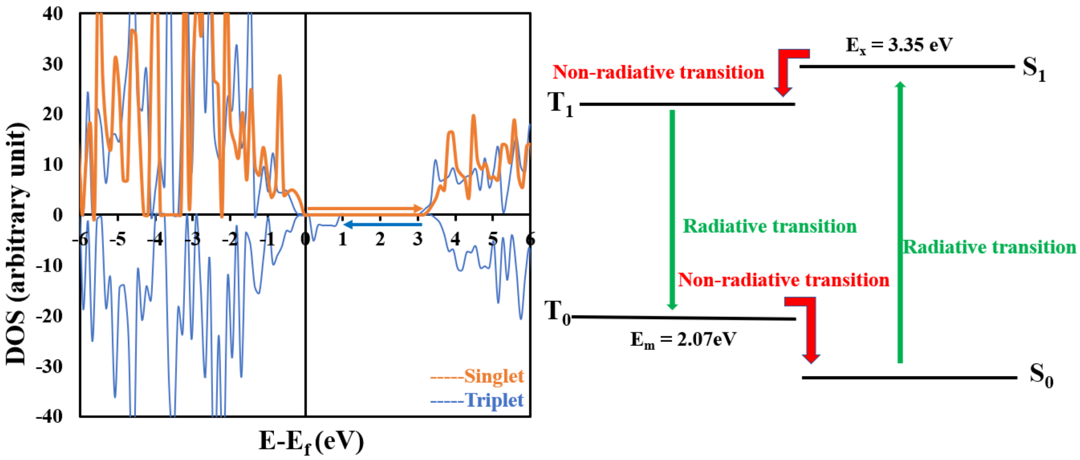

Figure 3.12. Total DOS of Cu-Cy-Cl of singlet and triplet state calculated with hybrid functional (HSE06).

Now, here we will explain the mechanism of emission phenomena of all Cu-Cy-X, especially for the experimental emission peaks [147], from the electronic structures' perspective, such as DOS plots shown in Figures 3.4 - 3.11.

From Figure 3.4 and 3.5, the first possible emission pathway is the simplest one, within Cu-Cy-I, photoexcited electrons de-excite from up-spin singlet CB to up-spin singlet VB which is the original state from where the electron was excited, a direct transition from S_1 to S_0 state, and the emission energy for this one will be equal to the excitation energy around 3.4 eV (364.66 nm) [singlet deexcitation, does not need S to T transition].

Second pathway involves non-radiative intra-band transition of electrons from the excitation S_1 state to T_1 in the CB. The singlet-triplet state (non-radiative transition) requires flipping of the spin up to down spin, and then de-excitation from 3.5 eV to 1.4 eV in spin-down band which is 2.1 eV (590.400 nm). This second de-excitation agreed well with the experimental result for Cu-Cy-I system where the experimental emission is 580 nm [147].

For Cu-Cy-F, one of the deexcitation that may occur with the non-radiative transition and spin flipping in lower range of energy from 3.10 eV to 1.00 eV that is 2.10 eV (590.40 nm) (Figure 3.6 and 3.7).

For Cu-Cy-Cl, the photoluminescence emission spectrum that may occur from the triplet state down spin from 3.07 eV to 1.00 eV which is 2.07 eV (598.9600 nm). This deexcitation is in the range of the experimental emission for Cu-Cy-Cl which is 2.04 eV (608.00 nm) (Figure 3.8 and 3.9).

Similarly, from the DOS plot of Cu-Cy-Br (Figure 3.10 and 3.11), there are some possible emission pathways can happen, but we will demonstrate the most probable one. Within the up-spin level, the singlet to triplet transition occurs in CB and as because triplet energy is lower, the electron will be in triplet CB and the de-excitation will occur from 3.20 eV to lower spin-down state 1.20 eV which is 2.00 eV (619.92 nm). This compared well to the experimental emission which is around 2.06 eV (601.00 nm) [147].

We can conclude that the initial excitation always occurs between the S_0 and the S_1, and then there is an intermediate non-radiative transition takes place from S_1 to T_1, and then to the lower available energy state. The spin-orbit-coupling plays an important role in the optical absorptions and emission spectra of Cu-Cy-X.

In conclusion, as we have seen that in a system with transition metal atoms, the large spin-obit-coupling will increase the probability of singlet excited to triplet excited state (S_1 -T_1 transitions), the non-radiative transition. Although, the spin-orbit coupling from Cu cite is suppressed in crystalline system, Cu-Cy is a molecular solid. Thus, the effect of spin-orbit-coupling from Cu atoms will be significant in the molecular unit.

The overall transitions we have here are between the S_0 and the S_1 (absorption), and the T_1 with T_0 or S_0 (emission) states. The intermediate non-radiative transition from S_1 to T_1 state can be in part due to part spin-orbit-coupling from Cu atoms.

3.2.4. Optical Absorption of Cu-Cy-X

We have calculated the theoretical optical absorption coefficients by considering periodic structures of Cu-Cy-X. As singlet state is the ground state of all Cu-Cy-X structures, we calculated the optical absorption of singlet state.

We have checked the quality of our theoretical results and the capability of our model to accurately represent the Cu-Cy crystal and its excited state chemistry by comparing it with the maximum of the first absorption peak in the experimental spectrum of Cu-Cy-X structures [147].

From the calculated optical absorption coefficients in Figure 3.13, we note that the initial absorption of Cu-Cy-I is around 3.40 eV (364.66 nm), and this absorption energy is compared well with the experimental one that is 3.46 eV (358 nm).

Also, we can see for Cu-Cy-Br, the absorption starts around 3.50 eV (354.24 nm). This excitation energy is close to one provided by the experimental data which is around 3.40 eV (364 nm). For Cu-Cy-Cl, we have seen that the absorption energy was 3.35 eV which is close to the experimental absorption energy 3.42 eV (362 nm) [147].

For the last Cu-Cy-F, the optical gap is around 3.6 eV (344.4 nm) which is not similar to the experimental data [147]. The reason being the synthesized of Cu-Cy-F sample which has mostly Cl than F, whereas the calculated model for Cu-Cy-F is a pristine one.

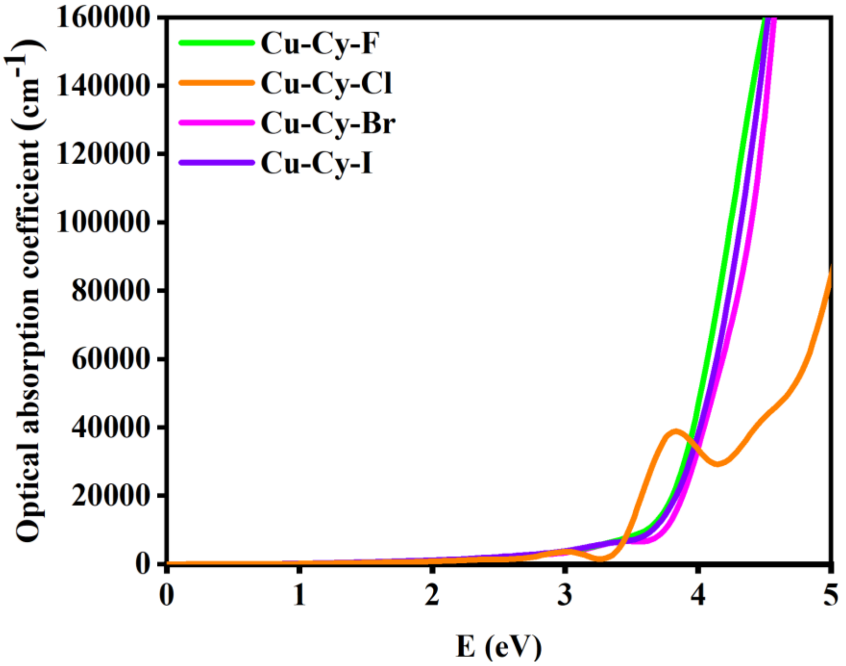

Figure 3.13. Optical absorption coefficients calculated with periodic boundary conditions calculated with hybrid functional (HSE06).

Notice all theoretical optical absorption values, we have got from the optical plot, are matching well with the calculated band gap we have from the band structure calculation using HSE06 functional. The computed band gaps of Cu-Cy-X are listed in Table 3.6. GGA functional has been used as well to obtain the band structures of Cu-Cy-X. Band structure of Cu-Cy-X calculated by GGA functional can be found in Appendix A (Figure A.1 - A.8).

Table 3.6. Band gaps of Cu-Cy-X calculated with hybrid functional (HSE06)

Structure (singlet)	Band gap (eV)
Cu-Cy-F	3.664
Cu-Cy-Cl	3.210
Cu-Cy-Br	3.454
Cu-Cy-I	3.352

3.2.5. Cu-vacancy and X-vacancy in Pristine Cu-Cy-X (X = F, Cl, Br, and I)

Cu vacancies (Cu_v) in the pristine Cu-Cy-X were investigated to observe another pathway for the destabilization of the Cu-Cy-X structures.

If we take out one Cu atom in Cu-Cy-X, then we are leaving charge (vacancy charge) in that atom vacancy in the structure. Those electrons that supposed to be given up by Cu atom is not given up by any other atom. If we relax the structure, then the atoms will start to move, and this charge vacancy may disappear because of the relaxation.

We have considered both the Cu (1) and Cu (2) vacancies. Figure 3.14 shows the GGA relaxed structural unit of the Cu-Cy-I crystal where (a) presents the pristine structure without defect, (b) the strucure with Cu (1) vcancy in which the vacancy is made with the Cu atom that bonds to I and S, and (c) in which the vacancy is made with the Cu (2) that bonds to the N and S.

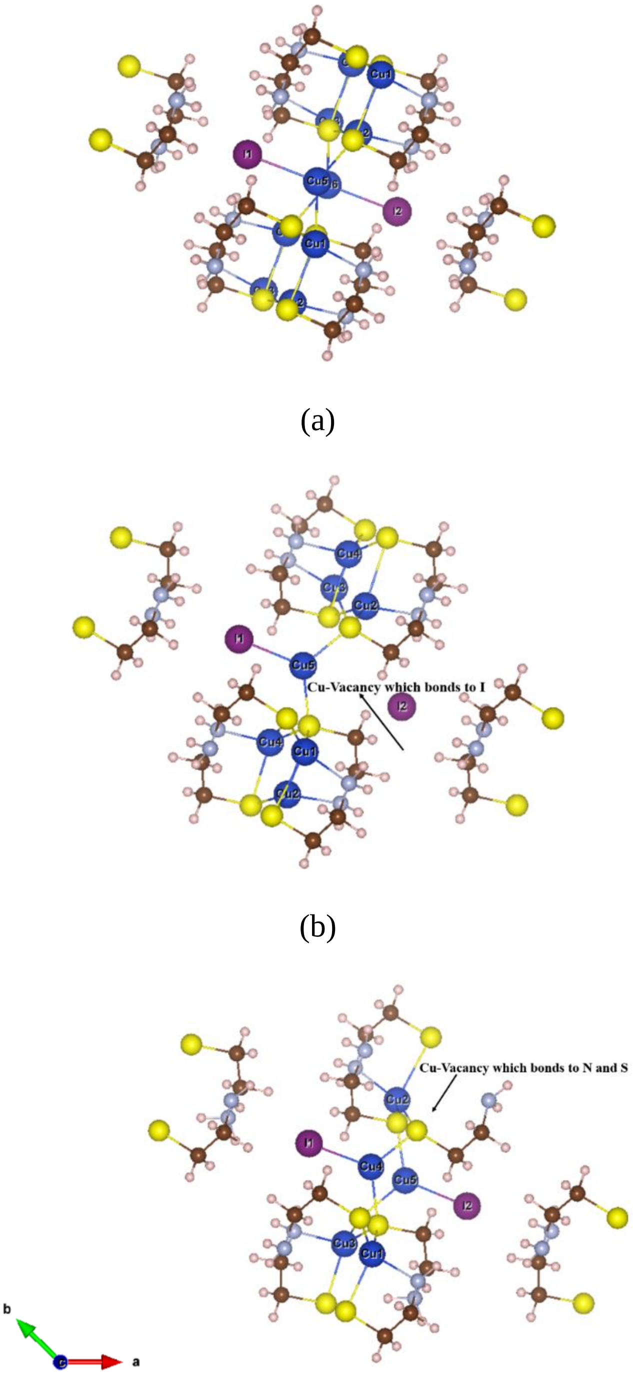

(a)

Cu-Vacancy which bonds to I

(b)

Cu-Vacancy which bonds to N and S

(C)

Figure 3.14. The relaxed unit cell of Cu-Cy-I crystal, (a) pristine without defect, (b) Cu-Cy-I with Cu (1) vcancy in which the vacancy is made with the Cu that bonds to I and S, (c) Cu-Cy-I with Cu(2) vcancy in which the vacancy is made with Cu that bonds to the N and S.

We have considered two different states when we make Cu vacancy (Cu_v) called doublet and quartet state as because the structure which is stabilized in singlet or triplet state cannot be stabilized in these states anymore when we make defects such as the Cu vacancy.

Our GGA calculations indicate that doublet state is the ground state for all Cu-Cy-X with Cu (1) vacancy and Cu (2) vacancy as it can be seen in Table 3.7, where the energy is lower in doublet state than in quartet state.

Table 3.7. Total energy of doublet and quartet state of Cu-Cy-X with Cu_v (1) and Cu_v (2) calculated by GGA functional

Structure	Cu_v (1) - doublet	Cu_v (1) - quartet	Cu_v (2) – doublet	Cu_v (2) - quartet
Cu-Cy-F	-243.473	-240.934	-243.110	-241.384
Cu-Cy-Cl	-241.072	-238.218	-240.886	-238.828
Cu-Cy-Br	-240.085	-237.220	-239.938	-237.695
Cu-Cy-I	-238.987	-236.081	-238.893	-236.564

3.2.5.1. Formation Defect Hybrid Calculation

We have used GGA functional to relax Cu-Cy-X structures with Cu-vacancies and then we have used hybrid functional to calculate the total energies of doublet state of Cu-Cy-X with Cu_v (1) and Cu_v (2) shown in Table 3.8.

Table 3.8. Total energy of doublet state of Cu-Cy-X with Cu_v (1) and Cu_v (2)

Structure	Doublet - Cu_v (1)	Doublet - Cu_v (2)
Cu-Cy-F	-304.162	-303.826
Cu-Cy-Cl	-300.501	-300.348
Cu-Cy-Br	-298.949	-298.845
Cu-Cy-I	-297.227	-297.165

The formation defect energy were calculated by equation 3.3. in the computational method and by considering both rich and poor conditions which are given by equation 3.4. and 3.5. Table 3.9, Figure 3.15 and 3.16 show the formation defect energy of Cu_v (1) and Cu_v (2) in Cu-Cy-X strucutres at Cu-poor and Cu-rich conditions in Cu-Cy-X.

Table 3.9. Defect formation energy of Cu_v (1) and Cu_v (2) in Cu-Cy-X strucutres

Structure	Cu_v (1) (eV)		Cu_v (2) (eV)	
	rich	poor	rich	poor
Cu-Cy-F	0.659	-2.824833333	0.995	-2.488833333
Cu-Cy-Cl	1.114	-2.0765	1.267	-1.9235
Cu-Cy-Br	1.04	-2.0845	1.144	-1.9805
Cu-Cy-I	0.765	-2.187666667	0.827	-2.125666667

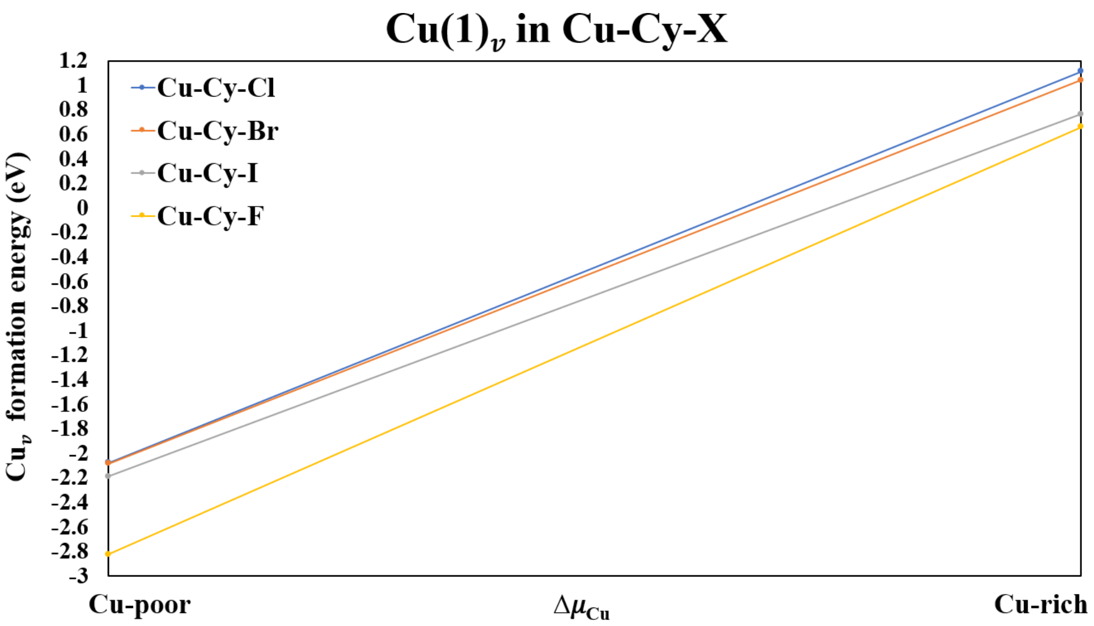

Figure 3.15. Defect formation energy with Cu_v (1) where Cu (1) is bonded to X and S at Cu-poor and Cu-rich conditions in Cu-Cy-X.

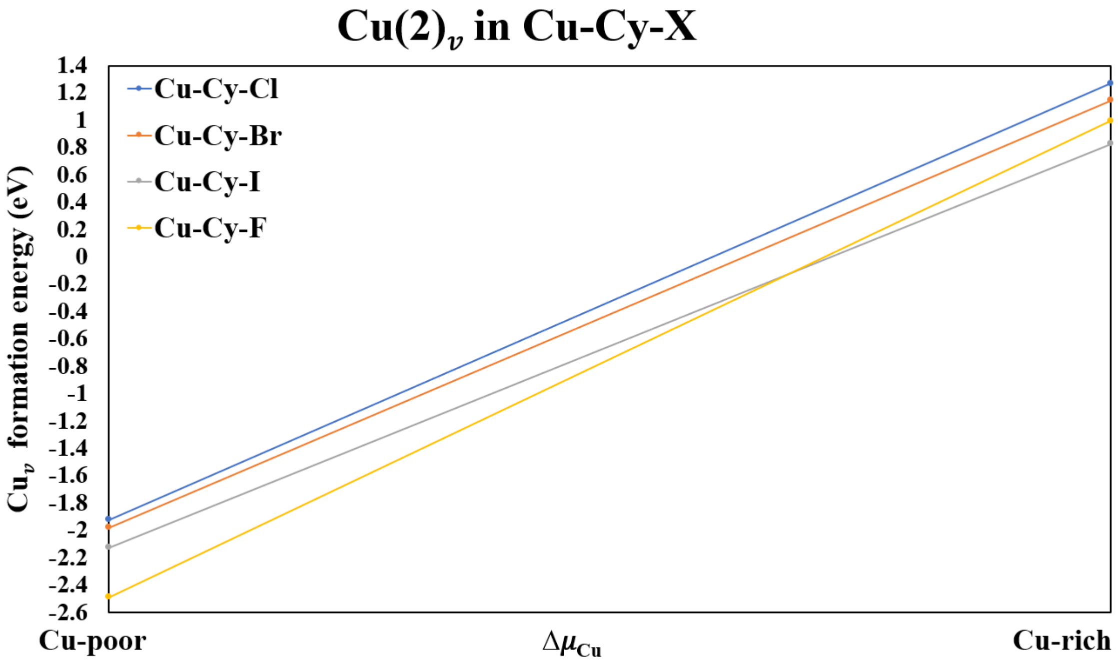

Figure 3.16. Defect formation energy with Cu_v (2) where Cu (2) is bonded to N and S at Cu-poor and Cu-rich conditions in Cu-Cy-X.

First, we can notice that at Cu-rich condition, the probability of making the vacancy will be less than when we have Cu-poor condition for both Cu_v (1) and Cu_v (2) as because at rich-condition of Cu, all Cu vacancy in Cu-Cy-X gives positive vaules. For the poor condition, the defect formation energy for all Cu-Cy-X are negative which means vacancies are more probable to be formed.

As it is mentioned above Cu-rich and Cu-poor, Cu-rich means Cu metal is rich in the environment where Cu-Cy is synthesizing. However, if we have less Cu, this will be Cu-poor condition.

Second point, we can see from the calculated Cu_v defect formation energies, the Cu (1) vacancy is more probable to form than the Cu (2). This also support the thermodynamic stability trend of the pristine Cu-Cy-X when higher stability was determined by the strength of the Cu (1)-X ionic bonds. Given the fact that Cu (1) is more prone to create vacancy than Cu (2), implies that Cu (1)-X bond would be broken easily, and hence, within the Cu-Cy-X family the strength of the Cu (1)-X bond can be a determining factor of its stability.

Last point to note, from the defect formation energies of Cu_v, it is more probable to form Cu vacancy in Cu-Cy-F than in Cu-Cy-Cl, Cu-Cy-Br and Cu-Cy-I. We can see that Cu-Cy-Cl has the highest stability comparing to Cu-Cy-I and Cu-Cy-Br where Cl bond breaking needs more energy than the other halogens. To explain this trend of formation energies, we need to consider the effect of electron's gain from Cu which is higher for Cu-Cl than Cu-Br and Cu-I due to the high electronegativity of Cl.

3.2.5.2. Formation Defect (Halogen Vacancy) GGA Calculation

We have done GGA calculations on Cu-Cy-X with halogens vacancy to see how the halogen vacancy affects the stability of the system.

In order to examine the stability of Cu-Cy-X with X_v, we need to obtain the total energy of individual elements in their ground state (bulk) phase as well the total energy of pristine structures using GGA functional.

Hence, we have done GGA calculation to get the total energy of individual elements in their ground state and we considered different states; singlet and triplet to determine the ground state of some molecules such as Cl_2, H_2, N_2, I_2, Br_2, and F_2. We have found that singlet state is the ground state of all of them. Table 3.10 presents the energy per atom for the elements calculated by GGA functional.

Table 3.10. Total energy of individual elements in their ground state (bulk) phase calculated by GGA functional

Element	E/atom (eV)
C	-9.303
S	-4.127
Cu	-3.715
N	-8.316
H	-3.385
I	-1.328
Br	-1.497
F	-1.858
Cl	-1.879

We have calculated the total energy of pristine Cu-Cy-X structures using GGA functional which is needed to calculate the formation defect. As usual, we have fully the relaxed the structure and then obtained the lattice parameters considering singlet and triplet states. The lattice parameters and the angles can be found in Appendix A (Table A.1 and A.2).

Point to notice that the results with GGA functional show same trend as what we have seen when we used hybrid functional on pristine structure of Cu-Cy-X where Cu-Cy-F has the lowest lattice parameters, following by Cu-Cy-Cl and Cu-Cy-Br which are in the middle and last Cu-Cy-I which has the highest lattice parameters because I has the highest atomic radius comparing to the other halogens.

Also, from the total energy calculation, we have seen similar trend of what we found in the hybrid calculation. We found that singlet has lower energy, and the difference between singlet and triplet state is ranging from 2.2 to 2.5 eV. Total energy of singlet and triplet state of Cu-Cy-X calculated by GGA functional can be found in Appendix A (table A.3).

We have calculated the formation energy of singlet pristine Cu-Cy-X structure shown in Table 3.11 as it will be used when we calculate the formation defects of Cu vacancy and halogen vacancy.

Table 3.11. Formation enthalpy of pristine Cu-Cy-X structures calculated by GGA functional

Structure	ΔH_f (eV)
Cu-Cy-F	-15.944
Cu-Cy-Cl	-13.789
Cu-Cy-Br	-13.594
Cu-Cy-I	-12.863

After the full relaxation of the Cu-Cy-X structures with X vacancy, we obtained the total energy of X_v in Cu-Cy-X. Total energy of X_v in Cu-Cy-X calculated by GGA functional can be found in Appendix A (table A.4). We have calculated the Defect formation energy using equation (3.3) in the computational method considering both rich and poor conditions which are given by equation (3.4) and (3.5). The formation energy for X_v defects in Cu-Cy-X strucutres calculated by GGA functional can be found in Appendix A (table A.5).

From Figure 3.17, we can see at rich condition of X vacancy in Cu-Cy-X, it is less probable to form X vacancy in Cu-Cy-X in all cases. However, in poor condition, it is more probable to form X vacancy as the system does not have enough X. Also, it can be seen that Cl vacancy is more probable to form in Cu-Cy-Cl followed by Br in Cu-Cy-Br and F vacancy is the least probable to form in Cu-Cy-F. Second, comparing X vacancy with Cu vacancy shown in previous section, it can be seen that X vacancy is more probable to be formed in Cu-Cy-X than Cu vacancy.

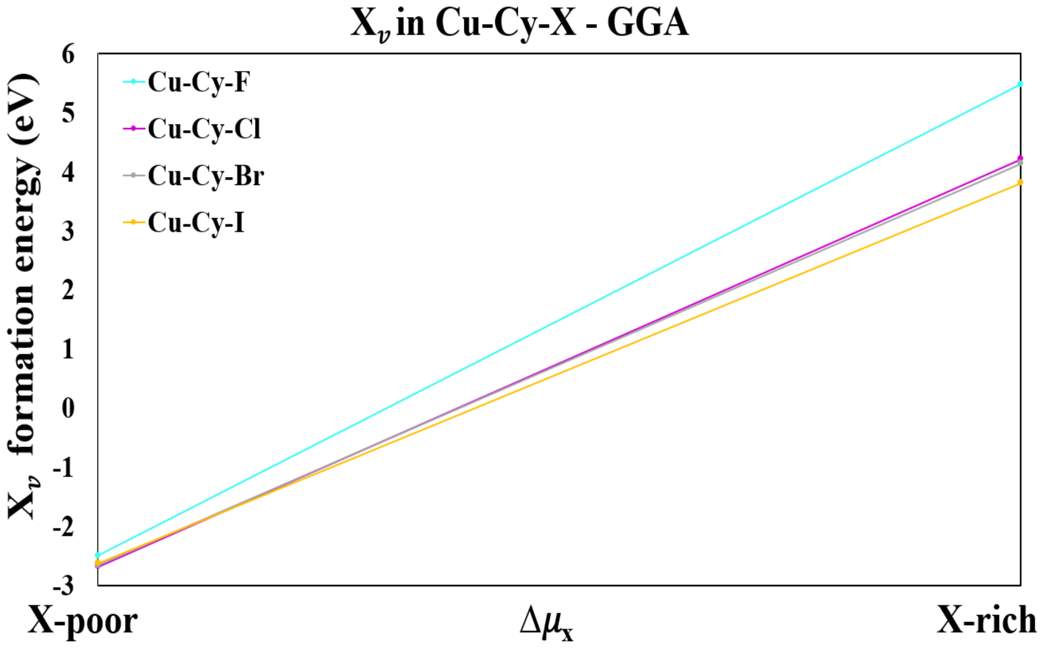

Figure 3.17. Defect formation energy with X_v (1) at X-poor and X-rich conditions in Cu-Cy-X.

3.2.6. Bader Charge of Cu-Cy-X Pristine and Cu$_v$ (1) and Cu$_v$ (2) in Cu-Cy-X

We have calculated the Bader charge of pristine Cu-Cy-X and when Cu$_v$ is made in Cu-Cy-X using the code which is provided by the Henkelman group and using equation (3.6) to see the change of charges' distribution with and without Cu vacancy.

To clarify the arrangement of the atoms, first S atom and forth S atom are connected to Cu (1) atom where we make the Cu vacancy (Cu$_v$ (1)). Cu (2) connects to S number 2,3 and S number 4 and it connects as well to N number 2.

From Table 3.12, Table 3.13, and Table 3.14, first point to notice in the pristine structure, the electron's gains by the Cl atom from Cu atom is higher than Br and I due to high electronegativity of Cl, and the charge of halogen is distributed almost equally for both. Also, we can see that the give up (donation) of Cu atoms that bond to halogens is higher in I than Br and Cl.

Also, in the pristine, we can see electron's gain by anion S atoms from Cu (1) is almost same within the structure and it is also almost same when we compare electron's gain of S atoms in all Cu-Cy-X structures. We have seen all Cu (2) have same charges as it connects to same atoms of N and S and that can be seen in all Cu-Cy-X structures.

However, in the defect structure where Cu (1) and Cu (2) vacancy are made, the distribution in the charges of Cu atoms are not equal. It increases when the Cu atom absences in both cases of Cu (1) and Cu (2) vacancy. Also, we can see the electron's gain of the halogens that is bond to Cu (1)-vacancy was higher than the other one, and Cl has higher gain comparing to I and Br.

The charges of N atoms in Cu-Cy-Cl, Cu-Cy-Br and Cu-Cy-I can be found in Appendix A (Table A.6, A.7 and A.8).

Table 3.12. Bader charge of Cl, S and Cu atoms in Cu-Cy-Cl

Atom	Pristine	Cu1-vacancy	Cu2-vacancy
Cl	-0.717083	-0.696896	-0.703019
Cl	-0.717083	-0.788785	-0.72141
S	-0.453609	-0.403487	-0.426756
S	-0.454245	-0.457582	-0.41885
S	-0.453535	-0.457582	-0.438735
S	-0.454286	-0.403757	-0.421274
Cu1	0.441813	0.50064	0.54699
Cu1	0.441813	-	0.54937
Cu2	0.497901	0.53353	0.56967
Cu2	0.497901	0.5325	0.48705
Cu2	0.497901	0.55791	0.51371
Cu2	0.497901	0.55927	-

Table 3.13. Bader charge of Br, S and Cu atoms in Cu-Cy-Br

Atom	Pristine	Cu1-vacancy	Cu2-vacancy
Br	-0.655348	-0.646275	-0.629584
Br	-0.65535	-0.752381	-0.656164
S	-0.451965	-0.386677	-0.415094
S	-0.451964	-0.444586	-0.427479
S	-0.451325	-0.444586	-0.445366
S	-0.451326	-0.387228	-0.417332
Cu1	0.403194	0.4563	0.43625
Cu1	0.403193	-	0.464
Cu2	0.498183	0.52929	0.55212
Cu2	0.498183	0.52819	0.549
Cu2	0.498182	0.55881	0.5747
Cu2	0.498182	0.56016	-

Table 3.14. Bader charge of Br, S and Cu atoms in Cu-Cy-I

Atom	Pristine	Cu1-vacancy	Cu2-vacancy
I	-0.564582	-0.575125	-0.544478
I	-0.564581	-0.699615	-0.575091
S	-0.452023	-0.39418	-0.421553
S	-0.452023	-0.428371	-0.420351
S	-0.452087	-0.428371	-0.444311
S	-0.452088	-0.393834	-0.410275
Cu1	0.37457	0.40782	0.38627
Cu1	0.37457	-	0.4148
Cu2	0.50811	0.52201	0.55191
Cu2	0.50877	0.52086	0.54173
Cu2	0.50877	0.55646	0.58047
Cu2	0.50811	0.55789	-

3.2.7. Bulk Modulus of Cu-Cy-X Structures

We have calculated the bulk modulus of Cu-Cy-X using GGA functional to see which of these structures is the softest and which one is the hardest. We have expanded the lattice parameters and as a result the volume get increased and do the other way by reducing the lattice and as a result the volume get decreased. We kept the cell volume fixed but we allowed the atoms to move freely without any constraint. Then, we obtained the total energy and get V-E plot. We have used Birch-Murnaghan equation of state to obtain the bulk modulus of Cu-Cy-X. Table 3.15 shows the volume and energy of Cu-Cy-X structures we obtained to get E-V plots which are shown in Figure 3.18. so, we can calculate the bulk modulus.

Table 3.15. The volume and energy of Cu-Cy-X structures GGA calculations to calculate the bulk modulus using Birch-Murnaghan equation

Cu-Cu-F		Cu-Cy-Cl		Cu-Cy-Br		Cu-Cy-I	
V (Å^3)	E (eV)	V (Å^3)	E (eV)	V (Å^3)	E (eV)	V (Å^3)	E (eV)
1633.65	-985.3123837	1737	-977.5601935	1791.1	-973.4524851	1886.94	-968.0456883
1657.38	-985.8446207	1761.32	-978.0134781	1815.89	-973.8628953	1912.68	-968.5042093
1681.3	-986.2974119	1785.83	-978.4398107	1840.87	-974.196324	1938.63	-968.8723166
1705.42	-986.6620182	1810.54	-978.6995818	1866.06	-974.5094097	1964.78	-969.1744593
1729.74	-986.9550214	1835.46	-978.8707954	1891.45	-974.7419426	1991.14	-969.3748441
1754.26	-987.1285533	1860.57	-979.0124029	1917.04	-974.8840171	2017.7	-969.5242385
1778.97	-987.2737982	1885.88	-979.0740152	1942.83	-974.9321143	2044.47	-969.6361392
1803.89	-987.3196377	1911.4	-979.0696173	1968.83	-974.9099135	2071.45	-969.6560852
1829.01	-987.2765435	1937.11	-978.9838881	1995.03	-974.8318412	2098.64	-969.6197536
1854.33	-987.2048463	1963.04	-978.8316832	2021.43	-974.6528391	2126.03	-969.5185279
1879.85	-987.0881919	1989.16	-978.541449	2048.04	-974.4645687	2153.63	-969.3941281

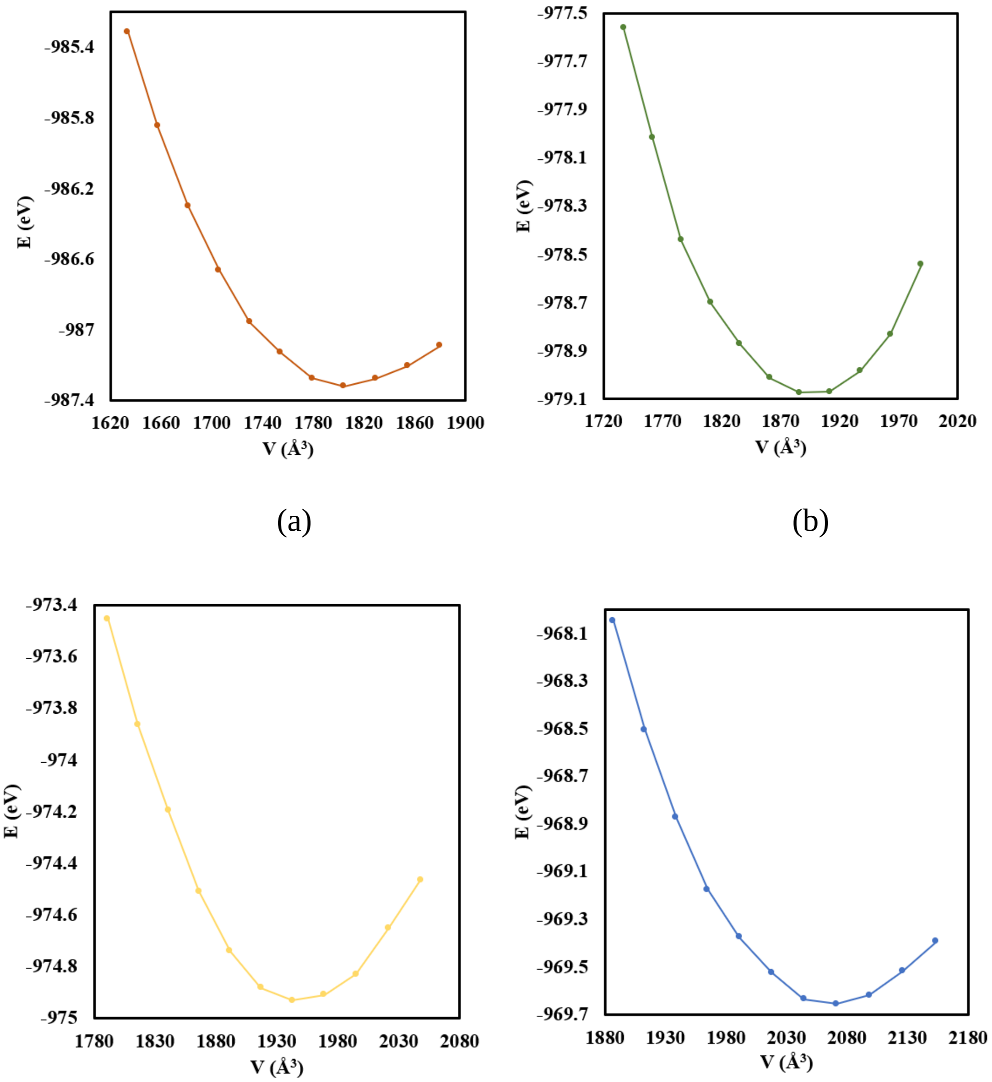

(a) (b)

(c) (d)

Figure 3.18. The E-V plot to calculate the bulk modulus of Cu-Cy-X structures (a) Cu-Cy-F (b) Cu-Cy-Cl (c) Cu-Cy-Br and (d) Cu-Cy-I.

Table 3.16 shows the bulk modules of Cu-Cy- X calculated by GGA functional. We can see from theortical calculations that Cu-Cy-Cl has the highest bulk modulus and Cu-Cy-Br has the second highest bulk modulus and the lowest bulk modulus belongs to Cu-Cy-I. This means Cu-Cu-Cl is the hardest material while Cu-Cu-Cy-I is the softest one.

Table 3.16. Bulk modules of Cu-Cy- X calculated by GGA functional

Structure	Bulk modulus (GPa)
Cu-Cy-F	30.142104
Cu-Cy-Cl	35.294791
Cu-Cy-Br	34.312845
Cu-Cy-I	26.427592

3.2.8. Surface Calculation of Cu-Cy-Cl and Cu-Cy-I Structures

As the experimental data shows there was Cu leaching when Cu-Cy-X is in aqueous solution after certain time, we have hypothesized when Cu atom in leaching out of the system, it will be through surface. Hence, we have calculated the diffusion barrier for Cu atoms to escape out of the surface of Cu-Cy-X to mimic the experimental observation.

We have made five layers of Cu-Cy-I and we have increased the bond length between one of the Cu atoms which bonds to I atom in the top layer and its equivalent Cu atom in the bottom layer by around 0.3 Å as shown in Figure 3.19. These steps are done also on Cu-Cy-Cl. Figure 3.19 shows the relaxed structures of Cu-Cy-I until two of Cu atoms that bond to I become completely out of the system and shown in the vacuum.

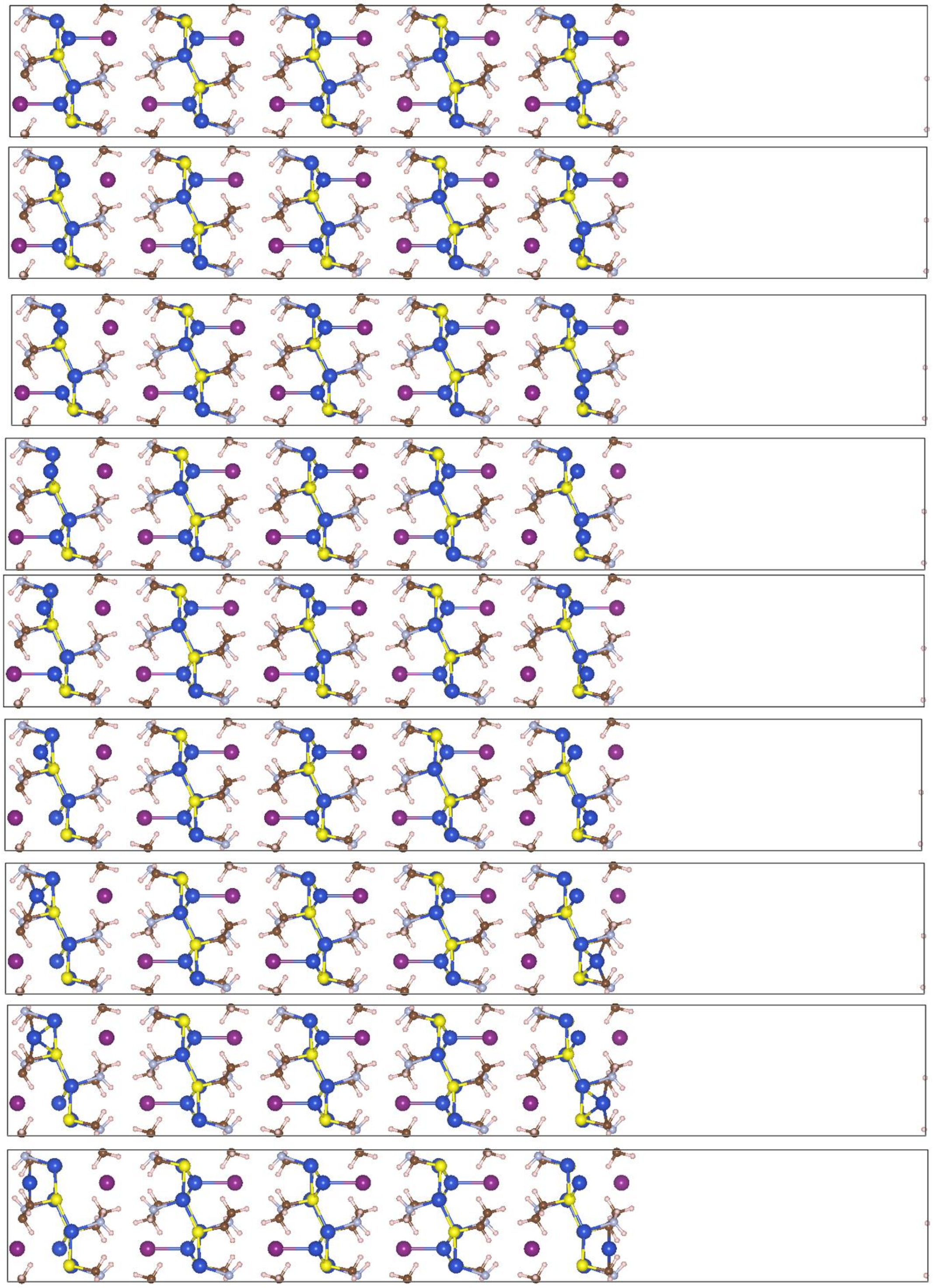

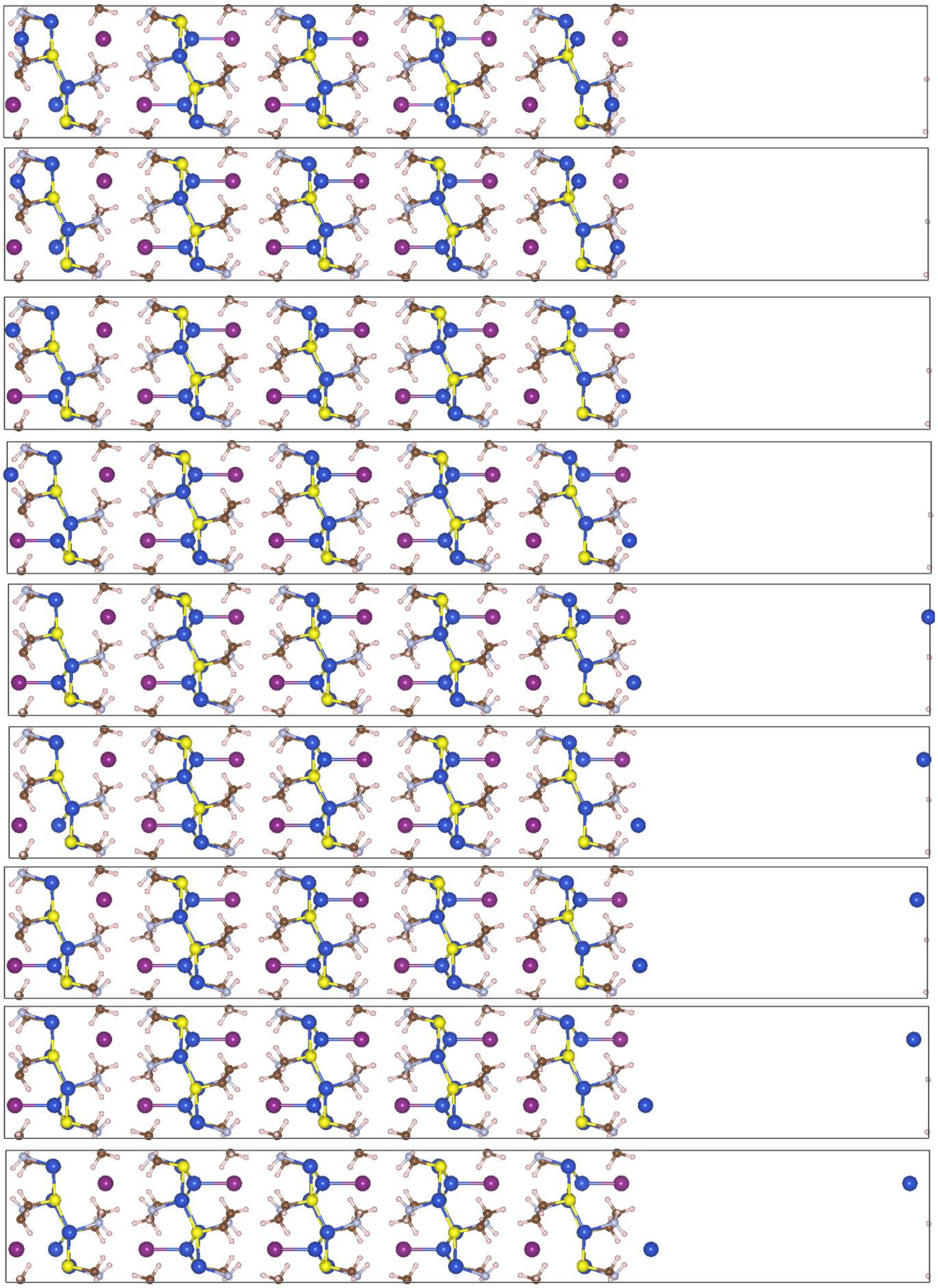

Figure 3.19. Relaxed structures of Cu-Cy-I where Cu atom, which was initially resided in the mid-Cu layer and bonded with the X atom of the other side, is moving toward the vacuum until it becomes out of system and presented in the vacuum from both sides.

We relaxed the structures of Cu-Cy-X (X = Cl and I) fully, and then we calculate the total energy of the structure. By calculating the energy difference between the pristine structure of Cu-Cy-X and the structure where we increase the bond length of two of the Cu atoms which bond to X to take it out of the layer, we can obtain the diffusion barrier for Cu atom to escape out of the surfaces of Cu-Cy-X.

Table 3.17 presents the bond length between Cu and X (X= Cl and I) after the relaxation and the relative energy of Cu atom in Cu-Cy-Cl and Cu-Cy-I. We can see that the total energy is increasing as we increase the bond length between Cu and X atom and as we increase it further, it reaches the highest energy that Cu needs to go out of the system. Then, after some points, the energy is decreased because Cu atoms are out of the system. Then, when these two Cu atoms are in the vacuum, the energy become almost same where it makes straight line due to the fact that they do not interact with system as well as they do not see each other in the vacuum. This can be seen in both Cu-Cy-Cl and Cu-Cy-I. However, we can see that Cu atoms in Cu-Cy-I need to face higher energy barrier to be out of the system comparing to Cu-Cy-Cl. This means Cu leaching out of Cu-Cy-I is less comparing to Cu leaching from Cu-Cy-Cl which is in a good agreement with the experimental observation. Figure 3.20 shows the rection barrier of Cu to be out of the systems in Cu-Cy-Cl and Cu-Cy-I.

Table 3.17. Bond length between Cu and X (X= Cl and I) after the relaxation and the relative energy of Cu atom in Cu-Cy-Cl and Cu-Cy-I

Cu-Cy-Cl		Cu-Cy-I	
Bond length (Å)	Relative energy (eV)	Bond length (Å)	Relative energy (eV)
2.40455	0	2.72122	0
2.70706	0.32723177	3.03127	0.31784177
3.00956	0.97559932	3.34131	0.95475705
3.31207	1.78794315	3.65135	1.82617941
3.61458	2.68104501	3.96139	2.86217801
3.91708	3.6035045	4.27142	3.98052293
4.2196	4.59761022	4.58146	5.14229333
4.5221	5.66941547	4.8915	6.27088758
4.82461	6.68574755	5.20154	7.31378972
5.12712	7.55614353	5.51157	8.20647646
5.42962	8.25967598	5.82161	8.74320938
5.73213	8.5936014	6.13165	8.70135997
6.03464	8.44964962	6.44168	8.31719983
6.37732	8.09844871	6.75172	8.02143327
6.63965	7.87349505	7.06176	7.68636853
6.94216	7.59044402	7.37179	7.61305485
7.24467	7.55008137	7.68183	7.64398696
7.54717	7.56093054	7.99187	7.71308621

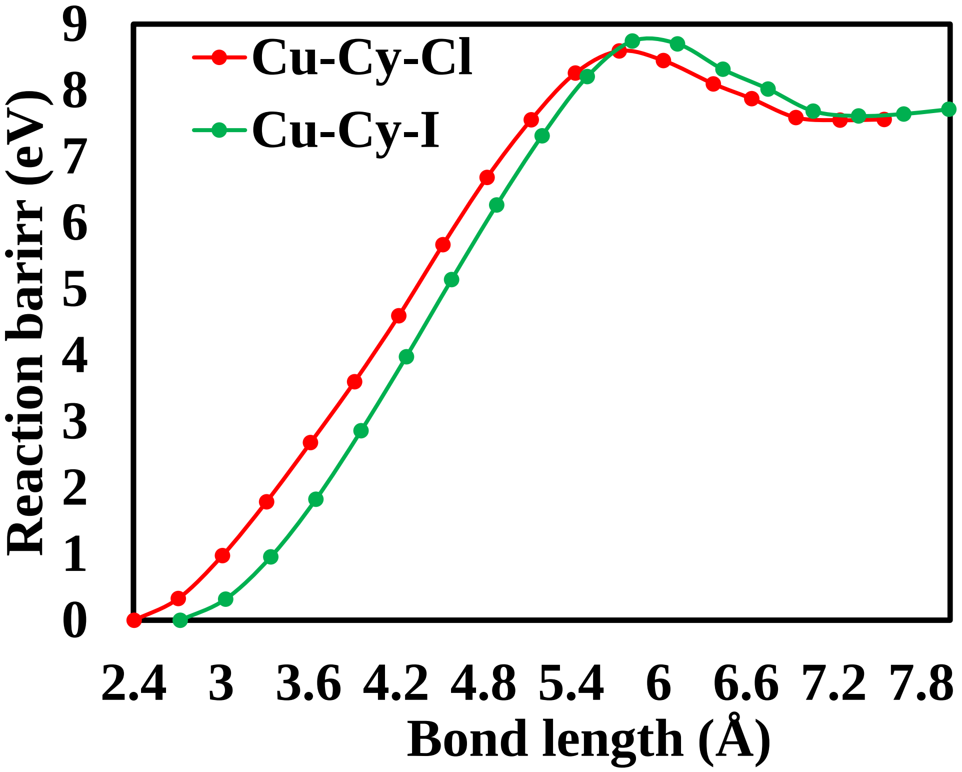

Figure 3.20. Reaction barrier of Cu atoms in Cu-Cy-CL and Cu-Cy-I.

Chapter 4

Mixed Halogens in Cy-Cy (Cu-Cy-X1_n-X2_m)

As we have found that the experimental synthesis of all Cu-Cy-X samples structures contained Cl as impurity, hence, it is imperative to understand the effect of Cl in the stability and properties of Cu-Cy-X. Here, we have used studied the mixed halogen in Cu-cysteamine Cu-Cy-X1_n-X2_m (X_1 =Cl and X_2 = F, Br, and I) and (n = 1,4, and 7 and m = 8 – n). We have studied the stability of Cu-Cy-X1_n-X2_m structures and their electronic and optical properties and see in what ways mixing of the halogens affect these properties.

4.1. Computational Method

The theoretical calculations of this work are based on the density functional theory (DFT) as implemented in Vienna ab initio simulation package (VASP) [123, 124]. Generalized gradient approximation (GGA) functional [113], the Perdew–Burke–Ernzerhof (PBE) [127] as an exchange-correlation functional is used. Core electrons in the calculation are treated with the projector augmented wave (PAW) method [125, 126]. The Heyd–Scuseria–Ernzerhof (HSE06) [120] hybrid function is utilized to determine properties such as the optical gaps. The kinetic cut-off energy for plane wave basis set is 500 eV. The convergence criterion, which is the global break condition for the electronic self-consistent loop, is 10^{-06} eV. The structures were relaxed until the Hellman–Feynman force equal to or less than -0.01 eV/Å. Crystal structures are optimized without any symmetry constraint, and all calculations are spin polarized. VESTA (visualization for electronic and structural analysis) [128] is used to visualize all the crystal structures. The Brillouin zone for the supercells was sampled by 1× 1×1 gamma centered k-mesh to relax the structures taking the size of the cell into account and by 5× 1×1 gamma centered k-mesh to calculate the total energies. C: $2s^2 2p^2$, Cu: $3d^{10} 4s^1$, F: $2s^2 2p^5$, Cl: $3s^2 3p^5$, Br: $4s^2 4p^5$, I: $5s^2 5p^5$, N: $2s^2 2p^3$, H: $1s^1$, S: $3s^2 3p^4$ are the valence electron configurations considered in this work. Due to the weak inter-layer interactions, we included the Van der Waals [130-136] corrections to the DFT Hamiltonian for proper structural relaxations and total energy calculations. In addition, as for spin-multiplicity, singlet and triplet states were considered for all structures

We have validated our theoretical approach in chapter 3 by comparing the lattice parameters and the angles which are calculated using hybrid functional with the data extracted from the X-ray diffraction experiments on the Cu–Cy crystals. The Comparison shows that the largest deviation was found for the Cu(2)–S(3) bond that was 2% from the experimental data which is in reasonable range, and the overall agreement is reasonable [49].

Formation enthalpies were calculated to examine the thermodynamic stability of the structures thermodynamically by following formula:

$$\Delta H_f\left(A_i B_j C_k D_l\right) = E_{total}\left(A_i B_j C_k D_l\right) - i\,E(A) - j\,E(B) - k\,E(C) - l\,E(D) \tag{4.1}$$

where A, B, C, D and D represent the elements and $i, j, k,$ and l are the total number of atoms, respectively, in the crystal cell considered for calculations. Also, ΔH_f is the formation enthalpy, E_{total} is the total energy of the structure, $E(A)$ present the energy per atom of element A in its ground state (bulk) phase.

A negative number of the formation enthalpy implies a thermodynamically stable configuration where more negative binding energy means more stable structure.

The optical absorptions are calculated for all Cu-Cy-Cl_n-$X2_m$ structures by using the frequency dependent complex dielectric function $\varepsilon(\omega) = \varepsilon_1(\omega) + i\,\varepsilon_2(\omega)$ which is calculated in the independent particle picture using VASP; here ε_1 and ε_2 are the real and imaginary parts of the dielectric constants, respectively, and ω is the frequency of the incident photon [139-141].

4.2. Results and Discussion

4.2.1 Stability of Cu-Cy-Cl$_n$-X2$_m$

The stability of Cu-Cy-Cl$_n$-X2$_m$ (X2 = F, Br, I) and (n = 1, 4, and 7 and m = 8 – n) materials have been studied with DFT by considering periodic structures of Cu-Cy-Cl$_n$-X2$_m$. Figure 4.1 shows the relaxed supercell structures of Cu-Cy-Cl$_n$-X2$_m$: (a) Cu-Cy-Cl$_n$-F$_m$, (b) Cu-Cy-Cl$_n$-Br$_m$, and (c) Cu-Cy-Cl$_n$-I$_m$ where we have 32 atoms of C, 24 atoms of Cu, 96 atoms of H, 16 atoms of N, 16 atoms of Sulfur and 8 atoms of X1 and X2. In this structure we have two different types of Cu atoms Cu (1), which bonds to two sulfur atoms and one of Cl or X2 atom, and the second one Cu (2), which binds to 4 other atoms in the crystal, three sulfurs and one N.

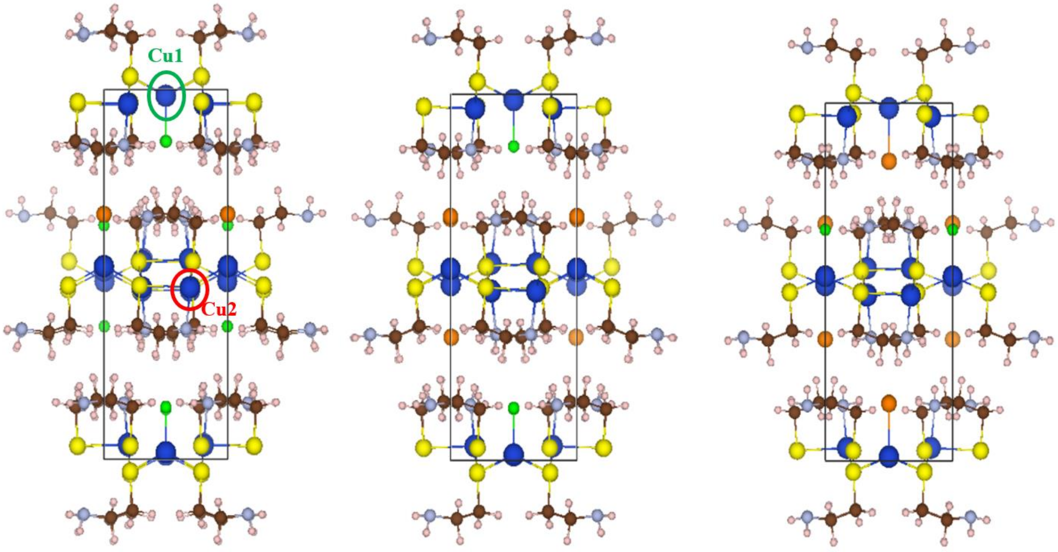

(1a) (2a) (3a)

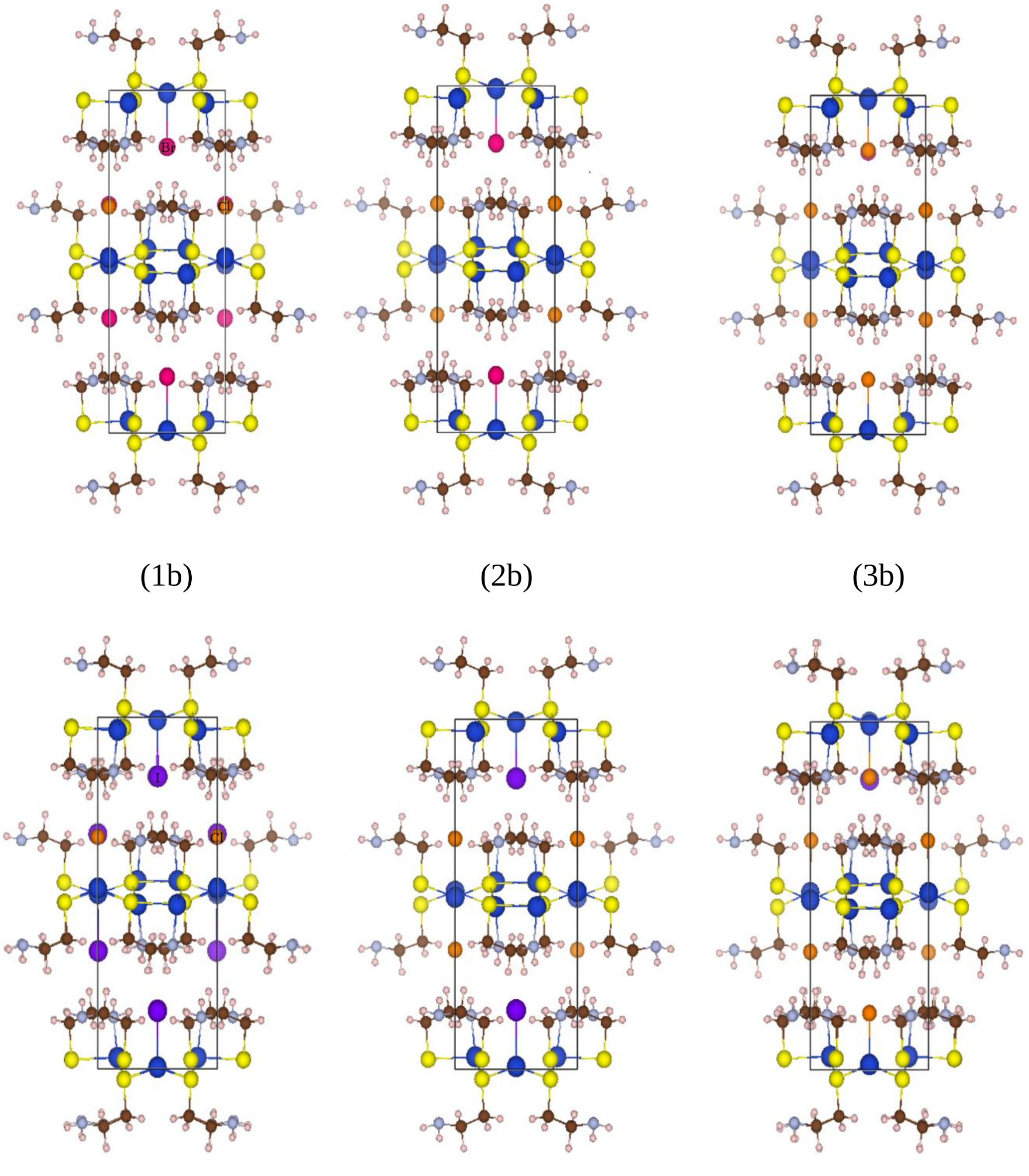

(1b) (2b) (3b)

(1c) (2c) (3c)

Figure 4.1. Relaxed supercell strucutres of Cu-Cy-Cl$_n$-X2$_m$: (1a) Cu-Cy-Cl$_1$-F$_7$, (2a) Cu-Cy- Cl$_4$-F$_4$, (3a) Cu-Cy- Cl$_7$-F$_1$, (1b) Cu-Cy-Cl$_1$-Br$_7$, (2b) Cu-Cy- Cl$_4$-Br$_4$, and (3b) Cu-Cy- Cl$_7$-Br$_1$, (1c) Cu-Cy-Cl$_1$-I$_7$, (2c) C Cu-Cy- Cl$_4$-I$_4$, and (3c) Cu-Cy- Cl$_7$-I$_1$. F atoms are represented in green, Cl in orange, Br in dark pink, I in purple, S in yellow, Cu in dark blue, C in brown, N in light blue and H in light pink.

We have changed the concentration of Cl and X2 = F, Br, and I with respect to the atomic weight % which is highest for I and lowest for F. The atomic weight of the elements in Cu-Cy-X1$_n$-X2$_m$ can be found in Appendix B (Table B.1, B.2 and table B.3).

In the present study, we consider three different mixed of Cl and X2 halogens. For example, we start with highest number of X2, such as we have 7 atoms of Br in Cu-Cy-Cl$_1$-Br$_7$ that is 16.76% and only one atom of Cl that is 1.06%. The opposite end mix would be making Cu-Cy-Cl$_7$-Br$_1$ structure with 7 atoms of Cl that is 8.08% and only one atom of Br that is 2.60%. The last mixer we examine is when we have same number of atoms of Cl and X2 where we have 4 atoms of Cl which is 4.43% and 4 atoms of Br which is 9.97% in Cu-Cy-Br$_4$-Cl$_4$. We have done same structures with Cu-Cy-Cl$_n$-F$_m$, and Cu-Cy-Cl$_n$-I$_m$ and the atomic weight of each structure can be found in the Appendix B (Table B.1, B.2 and table B.3). It can be seen that the atomic weight of the halogens is given in order of I > Br > Cl > F.

After relaxing Cu-Cy-Cl$_n$-X2$_m$ structures fully using GGA functional, and we calculated the total energies for all structures using (HSE06) hybrid functional as well as their optical absorptions and density of states. Calculations with hybrid functionals usually improved the band gaps values as compared to the GGA calculations. As Cu-Cy-X is a molecular solid, and it can stabilize in different spin-multiplicities, we consider singlet and triplet state. Table 4.1 and Figure 4.2 show the difference in energy between singlet and triplet states. The total energies for singlet states of all Cu-Cy-Cl$_n$-X2$_m$ structures are lower than the total energy of triplet state by about 3 eV. This indicates that singlet state in the ground state for all Cu-Cy-Cl$_n$-X2$_m$ structures.

Table 4.1. Total energies of Cu-Cy-X1$_n$-X2$_m$ structures singlet and triplet state

Structure	Singlet state	Triplet state
Cu-Cy- Cl$_1$-F$_7$	-1232.435	-1229.478
Cu-Cy- Cl$_4$-F$_4$	-1227.469	-1224.664
Cu-Cy- Cl$_7$-F$_1$	-1222.883	-1219.860
Cu-Cy- Cl$_1$-Br$_7$	-1215.528	-1212.488
Cu-Cy- Cl$_4$-Br$_4$	-1217.925	-1214.996
Cu-Cy- Cl$_7$-Br$_1$	-1220.433	-1217.403
Cu-Cy- Cl$_1$-I$_7$	-1208.400	-1205.522
Cu-Cy- Cl$_4$-I$_4$	-1213.682	-1210.853
Cu-Cy- Cl$_7$-I$_1$	-1219.367	-1216.427

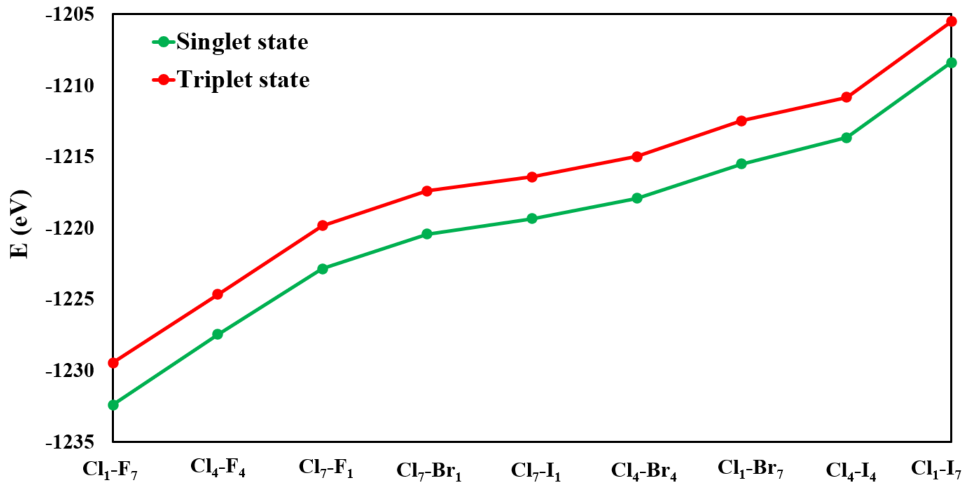

Figure 4.2. Total energies of Cu-Cy-Cl$_n$-X2$_m$ structures of singlet and triplet state.

Table 4.2 shows the lattice parameters and the lattice angles for singlet state for all Cu-Cy-Cl_n-$X2_m$ structures. We can see as we increase the concentration of Cl in Cu-Cy-Cl_n-F_m, the lattice expanded and as a result, the volume of the strucutres increased. Also, as we increase the conisntration of I in Cu-Cy-Cl_n-I_m, the volume of the cell increases from Cu-Cy-Cl_7-I_1 to Cu-Cy-Cl_1-I_7 implying that the average lattice constants are increasing to accommodate the larger atomic radius of I comparing to the other halogens.

Table 4.2. Lattice parameters of Cu-Cy-$X1_n$-$X2_m$ structures of singlet state calculated by GGA functional

Structure	a (Å)	b (Å)	c (Å)	α (°)	β (°)	γ (°)
Cu-Cy- Cl_1-F_7	6.232	16.874	16.902	90	93.98	90
Cu-Cy- Cl_4-F_4	6.360	16.708	17.039	90	94.94	90
Cu-Cy- Cl_7-F_1	6.542	16.588	17.130	90	96.18	90
Cu-Cy- Cl_1-Br_7	6.623	16.766	17.289	90	95.96	90
Cu-Cy- Cl_4-Br_4	6.589	16.697	17.255	89.99	96.01	90.01
Cu-Cy- Cl_7-Br_1	6.568	16.628	17.193	89.99	96.03	90
Cu-Cy- Cl_1-I_7	6.679	17.143	17.540	90	96.08	90
Cu-Cy- Cl_4-I_4	6.622	16.860	17.400	89.99	96.13	89.99
Cu-Cy- Cl_7-I_1	6.586	16.647	17.226	89.99	96.29	89.97

We calculated the formation enthalpies of Cu-Cy-Cl_n-$X2_m$ structures to compare the thermodynamic stability of all structures. To calculate the formation enthalpies of Cu-Cy-Cl_n-$X2_m$, total energy of individual elements in their ground state (bulk) phase are calculated using the hybrid functional which can be found in chapter 3 Table 3.4.

Table 4.3 shows the formation enthalpies of Cu-Cy-Cl_n-$X2_m$ structures for singlet state. First point to notice, when we compare the Cu-Cy-Cl_n-$X2_m$ strucutres, the lowest formation enthalpy belongs to the strucutre with highest concentration of F atoms in Cu-Cy-Cl_n-F_m that means Cu-Cy-Cl_1-F_7 is most stable structure thermodynamically following by Cu-Cy- Cl_4-F_4. Also, we have seen that Cu-Cy-Cl_n-F_m structures have lower formation enthalpy comparing to Cu-Cy-Cl_n-Br_m and Cu-Cy-Cl_n-I_m. Also, note that among the Br and I containing Cu-Cy, structures with higher concentration of Cl are thermodynamically more stable than the structures which have lower concentration of Cl. In general, the order of stability of these cysteamines follows Cu-Cy-Cl_n-F_m > Cu-Cy-Cl_n-Br_m > Cu-Cy-Cl_n-I_m. The trend can be correlated to the electronegativity of the halogens where F has the highest electronegativity and I has the lowest electronegativity. The higher electronegativity makes the ionic bonding part stronger and hence higher the thermodynamic stability of the structure. Hence, we can propose that the presence of Cl can help in increasing the thermodynamic stability of Cu-Cy-Cl_n-Br_m and Cu-Cy-Cl_n-I_m.

Table 4.3. The formation enthalpies of Cu-Cy-Cl_n-$X2_m$ structures of singlet state

Structure	ΔH_f (eV)
Cu-Cy- Cl_1-F_7	-20.812
Cu-Cy- Cl_4-F_4	-20.112
Cu-Cy- Cl_7-F_1	-19.508
Cu-Cy- Cl_1-Br_7	-18.926
Cu-Cy- Cl_4-Br_4	-19.064
Cu-Cy- Cl_7-Br_1	-19.230
Cu-Cy- Cl_1-I_7	-17.989
Cu-Cy- Cl_4-I_4	-18.486
Cu-Cy- Cl_7-I_1	-19.084

4.2.2. Optical Absorption

We have calculated the absorption spectra theoretically by calculating the optical absorption coefficients considering periodic structures of Cu-Cy-X and Cu-Cy-Cl_n-$X2_m$ structures shown in Figure 4.3. The optical absorptions are calculated for singlet states as the singlet state is the ground state of Cu-Cy-Cl_n-$X2_m$ structures where we divided the optical absorption plot into two regions I, and II.

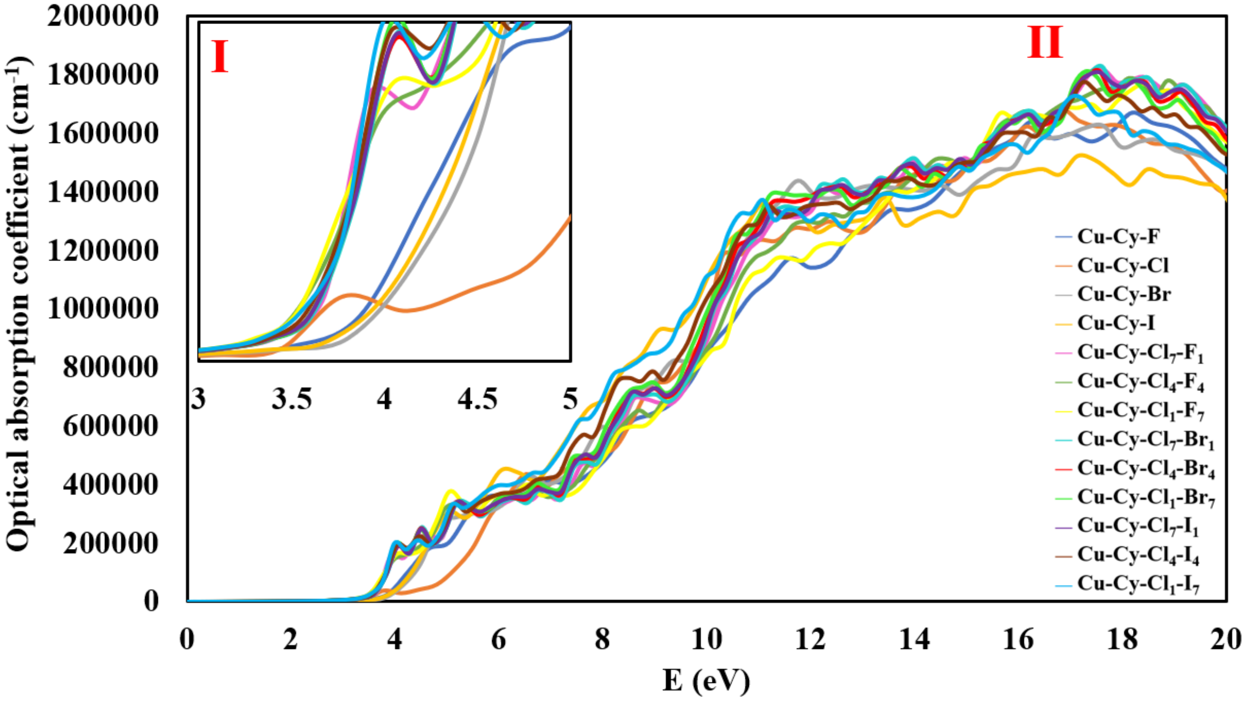

Figure 4.3. Optical absorption coefficients of Cu-Cy-X and Cu-Cy-X1$_n$-X2$_m$ using hybrid functional.

In region I, there is strong similarity in the onset of the optical absorptions for the mixed-halogens Cu-Cy-Cl$_n$-X2$_m$ structures. Also, it is noticeable that the increasing of the optical gaps started earlier for mix of halogens structures than the Cu-Cy-X pristine structures. We can estimate the optical gaps of the Cu-Cy-Cl$_n$-X2$_m$ structures which are ranged from 3.35 to 3.5 eV, and for Cu-Cy-X structures from 3.2 eV to 3.6 eV. Note that the gaps here were calculated from DFT using hybrid functional, so it would be very close to the experimental gaps which we will show when we compare our optical gaps with the experimental optical absorption.

Nevertheless, the difference in the optical gaps between all mixed halogens structures are low. This can be explained by the fact that all the halogens considered here has same valance electron. Thus, their contribution on the top of valance band and in the minimum of conduction band are similar.

In region II, we have noticed that the pristine cysteamine group are similar to the mix of halogens cysteamine group and we can still see the similar features in the optical absorptions within the Cu-Cy-Cl_n-$X2_m$ group itself as in the first region, the dominant and higher peaks belong to Cu-Cy-Cl_n-$X2_m$ structures comparing to pristine Cu-Cy-X structures. We have seen also in region II around 17 eV that the highest peaks belong to Cu-Cy-Cl_7-$X2_1$ structures (X2 = F, Br, and I), and the lowest peaks belong to the Cu-Cy-Cl_1-$X2_7$ structures which means Cu-Cy-Cl_7-$X2_1$ structures have highest absorption in very high energy range around 17 eV. This implies that higher Cl content resulted in higher absorption in the mixed halogen cysteamine.

Next, we compare the calculated optical absorptions of Cu-Cy-Cl_n-$X2_m$ structures with the experimental data [147]. It was found that there was significant unintended Cl impurity in all Cu-Cy-X. From the atomic weight percentages in Cu-Cy-Cl-X in Appendix B (Table B.1, B.2, and table B.3), the closest theoretical structures with the experimental ones are the following: Cu-Cy-Cl_7-F_1, Cu-Cy-Cl_1-Br_7, and Cu-Cy-Cl_1-I_7. For example, the experimental EDS results for Cu-Cy-Br sample shows 22.36 atomic weight % of Br is and 1.69 atomic weight % for Cl, whereas in our theoretical structure, we have 16.75 atomic weight % for Br and 1.06 for Cl.

The theoretical optical gap for Cu-Cy-Cl_7-F_1 structure is 3.50 eV which is close to the experimental value that was 3.42 eV, and for Cu-Cy-Cl_1-Br_7, we have 3.48 eV where the experimental gap was 3.40 eV and last Cu-Cy-Cl_1-I_7 structure, we got 3.48 eV theoretically which is in a good agreement with the experimental value that was 3.46 eV [147].

4.2.3. Density of States of Cu-Cy-Cl_n-I_m

Herein, we will discuss the contributions to the density of states (DOS) form Cu atoms as well as the halogen atoms in Cu-Cy-Cl_n-I_m. First, for Cu-Cy-Cl_1-I_7, we see in Figure 4.4 that the Cu1-3d orbital (that bonded with I) contributes at the valance band maximum (VBM), whereas the first noticeable DOS peak for Cu1 that is bonded with Cl comes at a slightly lower energy, at about around -0.4 eV. Nevertheless, there is slight contribution of it around -0.17 eV but not high as the ones which bond to I. Also, we notice that Cu2-3d orbital has high contribution near VBM that is around -0.17 eV. At the conduction band minima (CBM), there is contributions from Cu2-s and Cu2-3d as well as small contribution from Cu1-p (from Cu-Cl) but not as high as the contribution from Cu-3d orbitals in VB. Also, there similar contributions to the DOS from Cu1-3d orbital that bond to Cl with Cu1-3d orbital that bond to I.

Now, for the halogens' contributions to DOS, there is slight contribution from I-p orbital near fermi level and then at the slightly lower energy, the peak of the Cl-p starts to rise. The contribution from Cl-p orbital starts in the deep of the valance region at about -2 eV. The contribution from Cl-s orbital and I-s is not dominant as I-p and C-p orbital. Also, we can see that there is a tiny contribution from I-p orbital and Cl-p orbital in the CBM and they are behaving similarly 3.5 eV above Fermi level. At the conduction band minimum, at about 3 eV above the Fermi level, contributions from Cl and I are negligible.

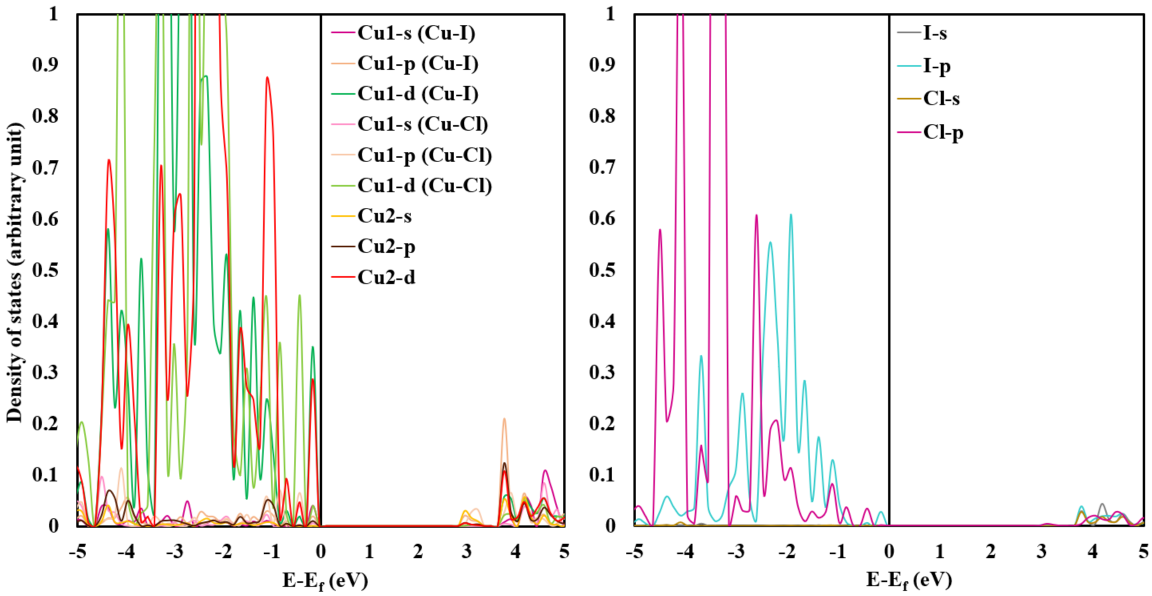

Figure 4.4. Partial density of states (DOS) of singlet state (S_0) Cu-Cy-Cl_1-I_7 calculated with hybrid density functional theory (HSE06) from Cl- and I- s and p orbitals as well as Cu (1) (Cu-Cl), Cu (1) (Cu-I) and Cu (2) s, p, and d orbitals. The top of the valence band is scaled to 0 eV, which is called Fermi level. For singlet state (S_0) only spin-up DOS is plotted.

Now, for the DOS plot of Cu-Cy-Cl_4-I_4, which is shown in Figure 4.5, we can compare the partial DOS of Cu atoms as following: Cu1-d orbital which bonds to Cl atom (Cu-Cl) has contribution at fermi level around -0.06 eV. On the other hand, there is a higher contribution from Cu1-d orbital which bonds to I (Cu-I) around -0.2 eV. It can be seen all three Cu-d orbitals have higher contribution near fermi level and Cu1-d (Cu-I) orbital and Cu2-d orbital have similar contribution. The presence of Cu orbitals on the top of the VB and the minimum of CB will provide the SOC [49]. In the CBM, there is some contribution from Cu1-p orbital which bonds to Cl (Cu-Cl).

Now, we can compare the contribution from Cl and I which can be seen from the partial DOS of Cl and I from both s and p orbitals. We can see near fermi level, there is almost no contribution from s- orbital of both the Cl and I. However, the contribution from I-p orbital is higher than Cl-p orbital in the deep region of valence band (VB).

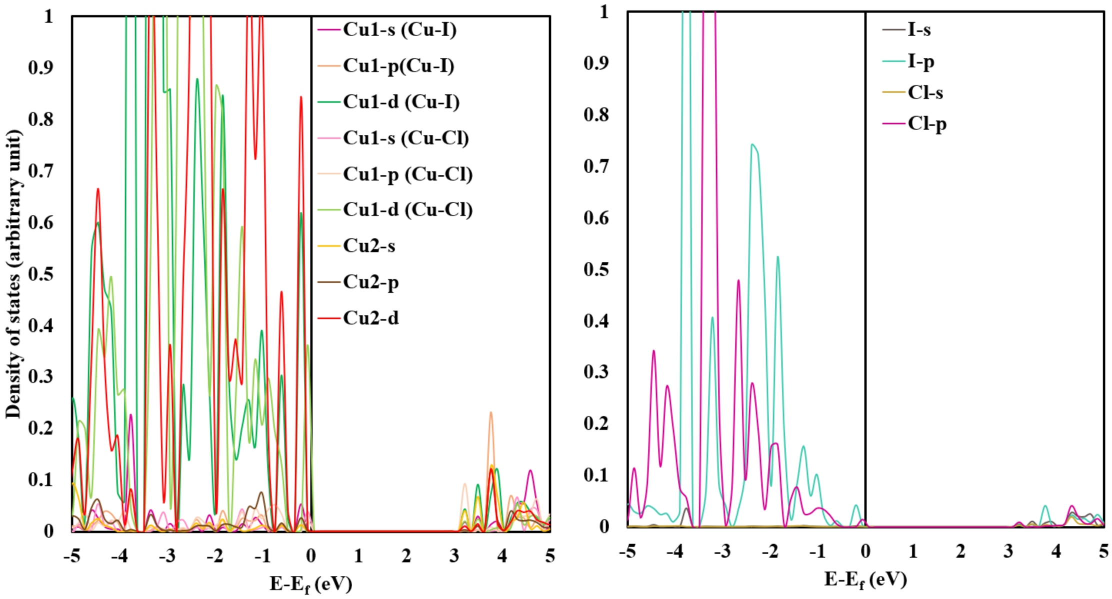

Figure 4.5. Partial density of states (DOS) of Cl, and I s and p orbitals, Cu (1) (Cu-Cl), Cu (1) (Cu-I), Cu (2) s, p, and d orbitals for the singlet state (S$_0$) in Cu-Cy-Cl$_4$-I$_4$ calculated with hybrid functional (HSE06).

Last, For Cu-Cy-Cl$_7$-I$_1$, the DOS plot is shown in Figure 4.6, we can see form the partial DOS of Cu atoms that the top of the valence band is dominated by Cu2-3d orbital, and the second dominant contribution is from Cu1-3d orbital that bonds to I atom, which behaves similarly as Cu2-3d orbital. Also, we can see that Cu1-3d (Cu-I) is not as dominant here in Cu-Cy-Cl$_7$-I$_1$ structure as it was in Cu-Cy-Cl$_4$- I$_4$ and Cu-Cy-Cl$_1$-I$_7$ structure.

From the partial DOS of Cl and I in Cu-Cy-Cl$_7$-I$_1$, the contributions of Cl-s orbital and I-s orbital are negligible in upper part of the VB (closer to the Fermi level) comparing to Cl-p orbital and I-p orbital. Also, there is small contribution from I-p orbital as well from Cl-p orbital on top of the valance band near fermi level, and after that the contribution is increasing for both I-p orbital and Cl-p orbital but it is higher for I-p orbital. Moreover, we have noticed similar features at the bottom of CB around 4 eV between I-p orbital and Cl-p orbital as well as between I-s orbital and Cl-s orbital.

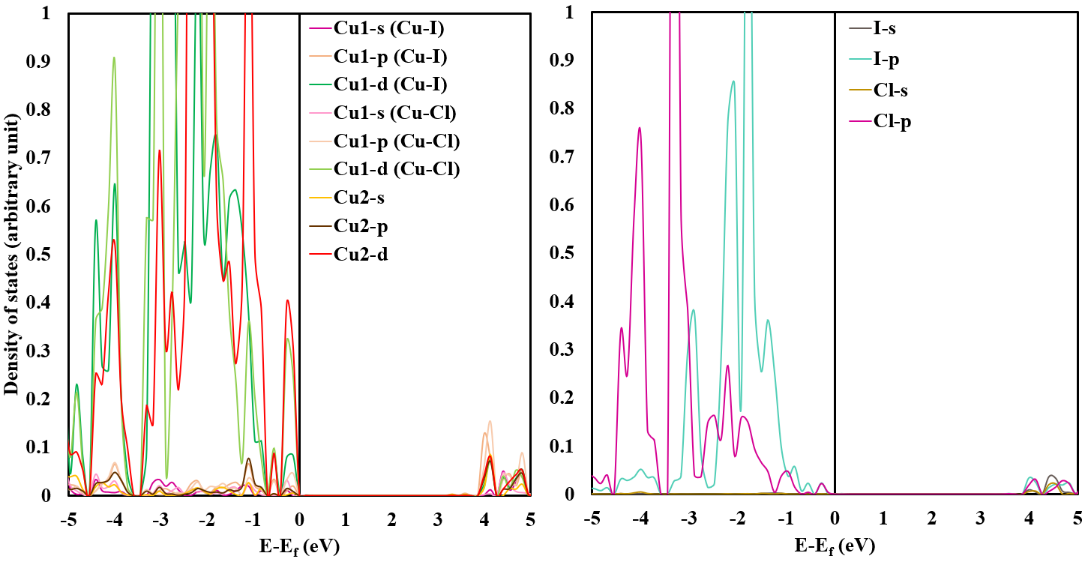

Figure 4.6. Partial density of states (DOS) of Cl, and I s and p orbitals as well as Cu (1) (Cu-Cl), Cu (1) (Cu-I), and Cu (2) s, p, and d orbitals for the singlet state (S_0) in Cu-Cy-Cl_7-I_1 calculated with hybrid functional (HSE06).

Last point to notice, as we know that the atom which has higher electronegativity will have lower contribution near fermi level, hence, I will have higher contribution on the top of VB than Cl atom which are seen in the DOS plots. Also, we have seen that as we increase the concentration of I, the Cu that bonds to I is more dominant in top of VB.

We have performed the DOS calculations for all Cu-Cy-Cl_n-$X2_m$ structures, and we have found that they all show similar behavior from Cu atoms as well as from the halogen atoms (DOS plots of Cu-Cy-Cl_n-F_m and Cu-Cy-Cl_n-Br_m as well Cu-Cy-Cl_n-I_m of all atoms can be found in Appendix B, (Figure B.1, B.2, B.3, B.4, B.5, B.6, B.7, B.8, and B.9).. In summary, we can conclude that 3d-orbitals from all type of Cu atoms Cu1 (Cu-Cl1), Cu1 (Cu-X2) and Cu2 have significant contributions to both valance bands and conduction bands where the spin-orbit-coupling can be important [49]. Besides, note that Cl and X2 show similar behavior in VB region as well in CB region in some of the mix of halogens structures as the halogens have same valance electrons configurations.

4.2.4. Bulk Modulus of Cu-Cy-X1$_n$-X2$_m$

We have calculated the bulk modulus of Cu-Cy-Cl$_n$-X2$_m$ using GGA functional. We have expanded the lattice parameters and as a result the volume get increased and do the other way by reducing the lattice and as a result the volume get decreased. We kept the cell volume fixed but we allowed the atoms to move freely without any constraint. Then, we obtained the total energy and get V-E plots.

The volume and energy of Cu-Cy-X1$_n$-X2$_m$ structures to calculate the bulk modulus can be found in Appendix B (Table B.4, B.5, and B.6) as well as the E-V plots of Cu-Cy-Cl$_n$-F$_m$ and Cu-Cy-Cl$_n$-Br$_m$ (Figure B.10, and B.11). We present here the E-V plots of Cu-Cy-Cl$_n$-I$_m$ structures which are shown in Figure 4.7. We have used Birch-Murnaghan equation of state to obtain the bulk modulus of Cu-Cy-Cl$_n$-X2$_m$ structures.

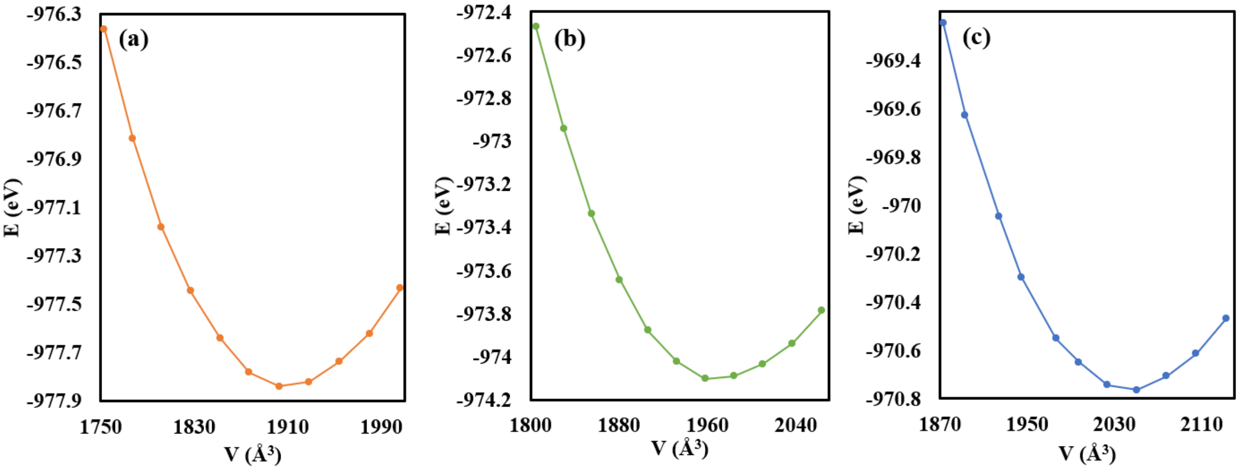

Figure 4.7. E-V plots of Cu-Cy- Cl$_n$-I$_m$ (a) Cu-Cy-Cl$_7$-I$_1$, (b) Cu-Cy-Cl$_4$-I$_4$ and (c) Cu-Cy-Cl$_1$-I$_7$.

Table 4.4 lists the bulk modulus of Cu-Cy-X and Cu-Cy- Cl_n-$X2_m$ structures. It can be clearly seen that Cu-Cy-Cl has the highest bulk modulus within Cu-Cy-X structures as well as compared to the mixed halogens structures. Also, we have seen that Cu-Cy-I has the lowest bulk modulus comparing to Cu-Cy-X structures implying that Cu-Cy-I is the softest material within Cu-Cy materials group. Moreover, we can see that for mixed halogens structures, the structures with higher concentration of Cl (Cu-Cy- Cl_7-$X2_1$) have higher bulk modulus. These results suggest that the presence of Cl in Cu-Cy-X2 (X2 = F, Br, and I) can help to make the material harder than when we have only one type of halogen such as F, Br, and I in Cu-Cy.

Table 4.4. Bulk modules of Cu-Cy-X and Cu-Cy-Cl_n-$X2_m$ calculated by GGA functional

Structure	Bulk modulus (Gpa)
Cu-Cy-F	30.142
Cu-Cy-Cl	35.295
Cu-Cy-Br	34.313
Cu-Cy-I	26.428
Cu-Cy- Cl_1-F_7	29.758
Cu-Cy- Cl_4-F_4	26.357
Cu-Cy- Cl_7-F_1	32.165
Cu-Cy- Cl_1-Br_7	31.727
Cu-Cy- Cl_4-Br_4	30.611
Cu-Cy- Cl_7-Br_1	32.765
Cu-Cy- Cl_1-I_7	27.328
Cu-Cy- Cl_4-I_4	28.872
Cu-Cy- Cl_7-I_1	30.154

Chapter 5

Transition Metal Cysteamine with Halogens (M-Cy-X; M = Co, Zn, Ag and Au)

Beside the transition metal Cu, we have decided to explore other possible cysteamine structures with different transition metals where some of them have same number of valance electrons as Cu such as Ag and Au, and other transition metals which have different number of valance electrons such as Co, and Zn. We have studied transition metal cysteamine with halogens using the following methodology.

5.1. Computational Method

The calculations are performed within density functional theory (DFT) as implemented in Vienna ab initio simulation package (VASP) [123, 124]. For the exchange-correlation functional, generalized gradient approximation (GGA) [113] as formulated by Perdew–Burke–Ernzerhof (PBE) [127] is utilized for structural relaxations. The core electrons are treated in this work with the projected augmented wave (PAW) method [125, 126]. The Heyd–Scuseria–Ernzerhof (HSE06) [120] hybrid function has been used to determine properties such as total energy, density of state and optical gaps. The following valence electron configurations are considered: C: $2s^2 2p^2$, F: $2s^2$ $2p^5$, Cl: $3s^2$ $3p^5$, Br: $4s^2 4p^5$, I: $5s^2 5p^5$, N: $2s^2$ $2p^3$, H: $1s^1$, S: $3s^2 3p^4$, Co: $3d^7 4s^2$, Cu $3d^{10}$ $4s^1$, Zn: $3d^{10}$ $4s^2$, Ag: $4d^{10} 5s^1$ and Au: $5d^{10} 6s^1$. The kinetic cut-off energy for plane wave basis set is 500 eV. The convergence criteria for the electronic self-consistent loop is 10^{-06} eV. Geometry optimizations are performed without any symmetry constraint, and the structures are fully relaxed until the Hellman–Feynman force equal to or less than -0.01 eV/Å. The calculations are spin polarized. The tetrahedron method is used to obtain total energy as well as for density of states (DOS) calculations [129]. VESTA (visualization for electronic and structural analysis) [128] is utilized to visualize the crystal structures before and after the relaxation. The Brillouin zone for the unit cell was sampled by 11× 11×11 gamma centered k-mesh in GGA calculations to relax the structures, to obtain total energy and for density of states calculations. For hybrid calculation, it was sampled by 1× 1×1 gamma centered k-mesh to relax the structures and by 3× 3×3 gamma centered k-mesh to calculate the total energies, optical absorption and for density of states calculations. Van der Waals [130-136] corrections to the DFT Hamiltonian is included for proper structural relaxations and total energy calculations due to weak inter-layer interactions. In addition, as for spin-multiplicity, singlet and triplet states were considered for all structures to obtain the ground state of the M-Cy-X structures.

The validation of the theoretical method has been done in our previous paper [49] as well as in chapter 3. We have compared the lattice parameters which are calculated by hybrid functional with the experimental data of the Cu–Cy crystals. The Comparison demonstrated that the overall agreement is reasonable [49], where the highest deviation was for the Cu–S bond which was 2% from the experimental data.

The formation enthalpies were calculated to examine the thermodynamic stability of the structures by following formula:

$$\Delta H_f\left(A_iB_jC_kD_l\right) = E_{total}\left(A_iB_jC_kD_l\right) - i\,E(A) - j\,E(B) - k\,E(C) - l\,E(D) \tag{5.1}$$

where A, B, C, D and D present the elements and $i, j, k,$ and l present the total number of atoms, respectively, in the crystal cell considered for calculations. Also, ΔH_f is the formation enthalpy, E_{total} is the total energy of the pristine structure, $E(A)$ present the energy per atom of element A in its ground state (bulk) phase. A negative number of the formation enthalpy implies a thermodynamically stable configuration where more negative binding energy means more stable structure.

The optical absorptions are calculated for all M-Cy-X structures by using the frequency dependent complex dielectric function $\varepsilon(\omega) = \varepsilon_1(\omega) + i\,\varepsilon_2(\omega)$ which is calculated in the independent particle picture using VASP; here ε_1 and ε_2 are the real and imaginary parts of the frequency dependent dielectric constants respectively, and ω is the frequency of the incident photon [139-141]. Bader charge analyses are performed using the code which is provided by the Henkelman group [142-146]. Bader net charge Q_{net} is defined as

$$Q_{net} = Q_{VASP} - Q_{Bader} \tag{5.2}$$

where Q_{VASP} is the valence charge which considered in the calculation, and Q_{Bader} is the calculated Bader atomic charge. Q_{net} can help to estimate the oxidation states of the atoms.

A DFT+U approach [148, 149] is used to better account for d-electron localization and correct for the known underestimation of gap energies which calculated by GGA functionals. An effective U of 4 eV has been applied to Co 3d orbitals as an on-site Coulomb correlation.

5.2. Results and Discussion

5.2.1. Stability of M-Cy-X

We have studied the stability of M-Cy-X with density functional theory by considering periodic structures of M-Cy-X where M= Co, Ag, Au, and Zn and X = F, Cl, Br, and I. First, we started with GGA calculations, and we relaxed the structures fully. Figure 5.1 shows the GGA relaxed structures of M-Cy-Cl where (a) Co-Cy-Cl, (b) Cu-Cy-Cl, (c) Ag-Cy-Cl, (d) Au-Cy-Cl, and (e) Zn-Cy-Cl. In the unit cell of M-Cy-X, we have 8 C atoms, 24 H atoms, 4 N atoms, 4 S atoms, 2 atoms of X (X= F, Cl, Br, I) and 6 atoms of M. As in Cu-Cy-X, the unit cell shows there are two different types of M atoms M (1), which is coordinated by two sulfur atoms and a X atom, and the second one M (2), which binds to 4 other atoms in the crystal, three sulfurs and one N. M-Cy-F, M-Cy-Br and M-Cy-I relaxed strucutres can be found in Appendix C (Figure C.1).

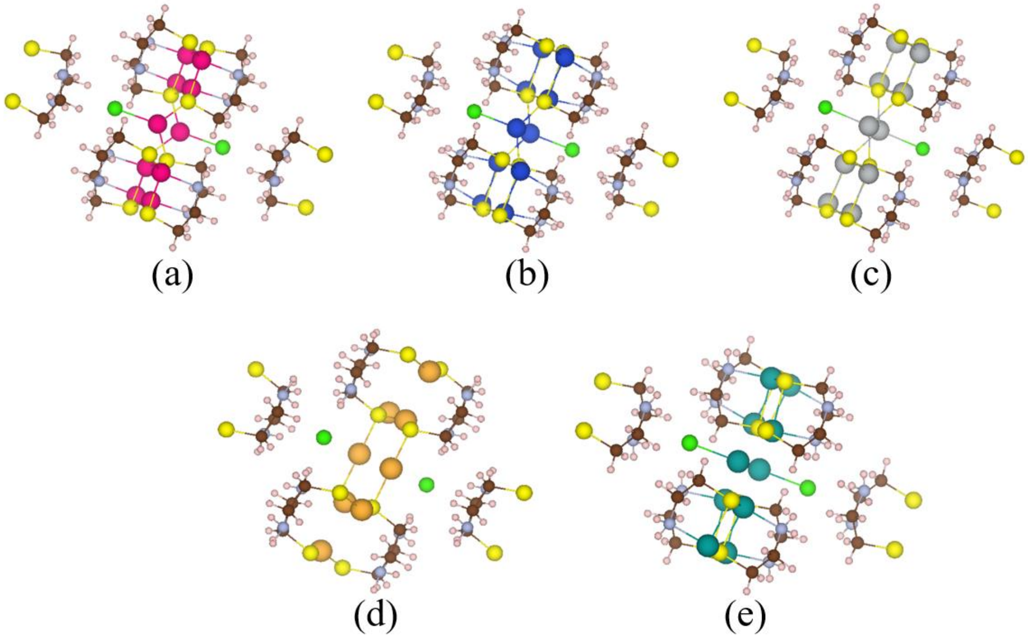
(a) (b) (c) (d) (e)

Figure 5.1. GGA relaxed structures of M-Cy-Cl (a) Co-Cy-Cl, (b) Cu-Cy-Cl, (c) Ag-Cy-Cl, (d) Au-Cy-Cl, and (e) Zn-Cy-Cl. Cl atoms are represented in green, S in yellow, Co in dark pink, Cu in blue, Ag in silver, Au in gold, Zn in dark green, C in brown, N in light blue and H in light pink.

Table 5.1 shows the GGA lattice parameters and angles for pristine Ag-Cy-Cl structure with and without VDW interactions and without specifying the state as singlet or triplet state shown in the first two rows and then with VDW interaction considering singlet and triplet state. Note that VDW potential plays a significant role in minimizing the lattice parameters, which can be seen in Table 5.2. Hence, based on our theoretical data, it is important to include the VWD potential for the other transition metals cysteamine structures.

Table 5.1. Lattice parameters and angels of pristine Ag-Cy-Cl structure with and without VDW of singlet and triplet state calculated by GGA functional

Structure	a (A^o)	b (A^o)	c (A^o)	α (^{o})	β (^{o})	γ (^{o})
Ag-Cy-Cl - without VDW (Without defending singlet or triplet state)	9.453	9.453	9.221	93.90	93.90	131.98
Ag-Cy-Cl - with VDW (Without defending singlet or triplet state)	9.301	9.301	9.087	93.16	93.16	133.43
Ag-Cy-Cl - with VDW - singlet	9.301	9.301	9.087	93.16	93.16	133.43
Ag-Cy-Cl - with VDW - triplet	9.314	9.314	9.447	92.37	92.37	136.50

Table 5.2. Total energy of pristine Ag-Cy-Cl structure with and without VDW of singlet and triplet state calculated by GGA functional

Structure	Total energy (eV)	ΔH_f (eV)
Ag-Cy-Cl - without VDW (Without defending singlet or triplet state)	-234.128	-7.972
Ag-Cy-Cl - with VDW (Without defending singlet or triplet state)	-238.449	-12.293
Ag-Cy-Cl - with VDW - singlet	-238.449	-12.293
Ag-Cy-Cl - with VDW - triplet	-236.038	-9.882

We can see that Co-Cy-Cl, and Ag-Cy-Cl structures remain mostly same as Cu-Cy-Cl, but Zn-Cy-Cl and Au-Cy-Cl are different from Cu-Cy-Cl where that can be seen from Figure 5.1. Au-Cy-Cl has different structural features than Cu-Cy-Cl shown in Figure 5.1 (d) where Au and Cl bond is missing, and Au is bonded only with two S atom. Also, Au1 is making linear bonding with S atoms in the middle layers which was not the case in Cu-Cy-Cl. This can be explained by the fact that the bond between Au and S is very strong, and meta-stability of Au(I)Cl compound [150].

Figure 5.1(e) shows Zn-Cy-Cl structure where Zn1 atoms (bonded to Cl) are not bonded with the nearby S atoms, instead Zn-Cl make a detached sub-layer. This can be explained by the fact that Zn2 has two extra electrons which can be given to S atoms in the middle layer, thus S can get enough from the other Zn2 atoms that bond to S and N atoms and does not need any from Zn1 that bonds to Cl. Besides, as the electronegativity of Cl is higher than S, the probability that Cl will get more electrons from Zn1 that attached to is higher than S to get from Zn1.

we have calculated the lattice parameters and the angles of all M-Cy-X where M = Co, Cu, Ag, Au, and Zn and X = F, Cl, Br, and I. Here we will present the lattice parameters and angles of M-Cy-Cl. The lattice parameters and angles of M-Cy-F, M-Cy-Br and M-Cy-I can be found in Appendix C (Table C.1, C.2 and C.3).

Table 5.3 shows the lattice parameters of M-Cy-Cl structures of singlet and triplet state calculated by GGA functional. It can be seen that the lattice parameter c is larger in both singlet and triplet state of Zn-Cy-Cl and c is larger for triplet state only in Ag-Cy and Au-Cy.

Table 5.3. Lattice parameters and angles of M-Cy-Cl structures of singlet and triplet state calculated by GGA functional

Structure	a (A^o)	b (A^o)	c (A^o)	α (^{o})	β (^{o})	γ (^{o})
Co-Cy-Cl /singlet	9.008	9.008	8.1059	92.67	92.67	140.21
Co-Cy-Cl /triplet	9.042	9.042	8.128	92.49	92.49	140.17
Cu-Cy-Cl /singlet	9.233	9.233	7.674	95.89	95.89	132.00
Cu-Cy-Cl /triplet	9.339	9.339	7.634	95.79	95.79	132.64
Ag-Cy-Cl /singlet	9.301	9.301	9.087	93.16	93.16	133.43
Ag-Cy-Cl /triplet	9.314	9.314	9.447	92.37	92.37	136.50
Au-Cy-Cl /singlet	9.207	9.207	8.502	97.48	97.48	127.15
Au-Cy-Cl /triplet	9.119	9.119	9.331	93.59	93.59	132.46
Zn-Cy-Cl /singlet	8.711	8.710	11.468	85.86	85.86	137.48
Zn-Cy-Cl /triplet	9.242	9.242	11.324	86.82	86.82	142.13

After the full relaxation, we obtained the total energies in singlet and triplet state which are shown in Table 5.4. It can be seen that singlet state of Ag-Cy-X, and Au-Cy-X structures has lower energy comparing to triplet state which means singlet state is the ground state of them. Hence, Ag-Cy-X and Au-Cy-X have the same ground state as Cu-Cy-X structure. However, the total energy of Co-Cy-X structure is lower for triplet state than singlet state which means Co-Cy-X stabilizes in triplet state; implying its optical transition mechanisms will be different from that of Cu-Cy-X.

The absorption for Co-Cy will start from triplet state. Lastly, in Zn-Cy-X, the difference between singlet and triplet state is very small with highest difference around 0.3 eV for the unit cell. Zn-Cy-F, Zn-Cy-Br and Zn-Cy-I are stabilized in singlets state. On the other hands, Zn-Cy-Cl stabilizes in triplet state.

Table 5.4. Total energy of singlet and triplet state of M-Cy-X (X= F, Cl, Br, and I), (M= Co, Cu, Ag, Au and Zn)

Structure	F		Cl		Br		I	
	Singlet	Triplet	Singlet	Triplet	Singlet	Triplet	Singlet	Triplet
Co-Cy	-264.419	-264.894	-261.464	-262.026	-260.210	-260.777	-258.713	-259.291
Cu-Cy	-247.386	-245.140	-245.267	-242.757	-244.314	-241.916	-243.245	-240.866
Ag-Cy	-240.475	-238.457	-238.449	-236.038	-237.673	-235.254	-236.753	-234.321
Au-Cy	-242.771	-240.901	-240.011	-237.954	-239.195	-237.266	-238.237	-236.183
Zn-Cy	-232.182	-232.178	-229.747	-229.840	-228.896	-228.585	-227.961	-227.656

As because some of the transition metal cysteamine stabilize in singlet state and some in triplet state, we have calculated the formation enthalpy of M-Cy-X for both states as shown in Table 5.5. First point to notice, when we compare the stability of M-Cy-X with respect to the halogens X, the M-Cy-X structures with F atoms are the most stable structures thermodynamically comparing the other halogens. M-Cy-X structures with Cl atoms is the second most stable structures, following by M-Cy-Br structures and the least thermodynamically stable structures are M-Cy-I. Second point, when we compare the stability of structures with respect to the transition metal M, we can see that Cu-Cy-X is the most stable structures thermodynamically. The stability of other transition metal is given in order of Zn-Cy-X > Ag-Cy-X > Au-Cy-X > Co-Cy-X.

Table 5.5. Formation enthalpy of singlet and triplet state of M-Cy-X (X= F, Cl, Br, and I), and (M= Co, Cu, Ag, Au and Zn)

Structure	F		Cl		Br		I	
	Singlet	Triplet	Singlet	Triplet	Singlet	Triplet	Singlet	Triplet
Co-Cy	-12.619	-13.094	-9.622	-10.184	-9.132	-9.699	-7.973	-8.551
Cu-Cy	-15.944	-13.698	-13.783	-11.273	-13.594	-11.196	-12.863	-10.484
Ag-Cy	-14.361	-12.343	-12.293	-9.882	-12.281	-9.862	-11.699	-9.267
Au-Cy	-13.987	-12.117	-11.185	-9.128	-11.133	-9.204	-10.513	-8.459
Zn-Cy	-15.512	-15.508	-13.035	-13.128	-12.948	-12.637	-12.351	-12.046

In the following, the rest of the calculations on transition metals with Cl atoms as because the transition metals Co, Ag, Au and Zn cysteamine with the other halogens show similar trend of stability as what we found in Cu-Cy-X (X=F, Cl, Br, and I). Also, Cu-Cy-Cl was the first structure to be synthesized and studied experimentally and theoretically.

5.2.2. Bader Charge of M-Cy-Cl

As some of transition metals we considered here have different number of valance electrons such as Zn which has one extra electron comparing to Cu; and there are six Zn atoms in a unit cell. Hence, there will be extra six electrons that are distributing to the other atoms around it. Thus, we have decided to calculate Bader charges for M-Cy-Cl to see the charge distribution in the metal cysteamine systems. The Bader charges of M-Cy-Cl were calculated by the code provided by the Henkelman group and using equation (5.2)

Table 5.6 presents the Bader charges of Cl, M, N and S atoms in M-Cy-Cl, calculated with their respected ground state. First, we will compare the charges of Cl atoms in different transition metal cysteamine. The Cl atoms in Au-Cy-Cl structure has the highest charge comparing to the Cl atoms in the other transition metal cysteamine structures. On the other hand, Au atoms, have the lowest charges comparing to the other metals specially for Au atoms which bond to the Cl atoms. This means Au atoms give more charges to Cl atoms than the other metals even though it is not "apparently" bonded to it within Au-Cy-Cl structure, as shown in Figure 5.1 (d). S atoms has the lowest gain of charge in Au-Cy-Cl even though Au is bonded to S in Au-Cy-Cl. Also, we have seen that the second highest gain of charge for Cl atoms is in Zn-Cy-Cl. However, the gain of charges for Cl atoms in Co-Cy-Cl, Cu-Cy-Cl, Ag-Cy-Cl and Zn-Cy-Cl are very close to each other.

Also, we have notice that even though Cl gain more charge in Zn-Cy-Cl than Co-Cy-Cl, Cu-Cy-Cl and Ag-Cy-Cl, Zn has the highest charge comparing to the other metals which can be explained by the fact that Zn has +2 oxidation state while other transition metals have +1 oxidation state. On the other hand, S atoms is gaining more charges from Zn comparing to all other metals where we expect that due to the fact that ZnS is very stable material and Zn atom is interacting more with S atom. Also, it is noticeable that Zn by itself is retaining more charge because Zn has higher valance electrons comparing to the other metals. The highest charge of Zn atoms can be seen for Zn2 which are bonded with S and N but not for Zn1 atoms which are bonded with Cl and S as Zn is giving charges to Cl and S.

Comparing the Bader charges between Co-Cy-Cl and Cu-Cy-Cl, Co atoms tend to give more to charges Cl atoms than Cu, as Cu has higher electronegativity than Co. Also, we have noticed that Cl atoms in Co-Cy-Cl and Cu-Cy-Cl have similar charge. When we compare the charges of S atoms in Co-Cy-Cl and Cu-Cy-Cl, that S has lower charge in Co-Cy-Cl. Last, we have notice that N atoms has similar charges in all M-Cy-Cl structures. Charge of H and C atoms in M-Cy-X can be found in Appendix C (Table C.4).

Table 5.6. Bader charges of Cl, M, N and S atoms in M-Cy-Cl calculated in their ground state

Singlet	Co-Cy-Cl	Cu-Cy-Cl	Ag-Cy-Cl	Au-Cy-Cl	Zn-Cy-Cl
Cl	-0.67751	-0.67256	-0.6856	-0.74682	-0.68719
Cl	-0.67751	-0.67256	-0.68561	-0.74682	-0.68719
M	0.488553	0.466266	0.383445	0.194289	0.597398
M	0.487151	0.465068	0.382592	0.192705	0.597399
M	0.487031	0.464959	0.382592	0.192702	0.597389
M	0.488434	0.466157	0.383453	0.194289	0.597389
M	0.394756	0.429937	0.348059	0.146074	0.207187
M	0.394755	0.42996	0.34804	0.146094	0.207188
S	-0.40355	-0.44739	-0.34148	-0.0883	-0.46043
S	-0.40353	-0.44739	-0.34144	-0.08828	-0.46048
S	-0.40353	-0.44739	-0.34144	-0.08828	-0.46072
S	-0.40355	-0.44739	-0.34148	-0.08831	-0.46066
N	-1.14444	-1.13856	-1.13376	-1.13999	-1.09799
N	-1.14445	-1.13856	-1.13376	-1.14001	-1.09799
N	-1.14445	-1.13856	-1.13374	-1.14001	-1.09799
N	-1.14444	-1.13856	-1.13374	-1.13999	-1.09799

As the main goal of studying Cu-Cy-X structures is to be used in light absorption, so it is important to study the electronic and optical properties to get the band gap and the optical gap of M-Cy-Cl. Hence, we have done density of states DOS and optical absorption calculations.

5.2.3. Density of States of M-Cy-Cl

We have calculated the orbital projected partial and total density of states (DOS). It is known GGA functionals underestimate the localization of the orbitals, that is it cannot localize the electrons properly. Hence, we have done orbital projected partial density of states using hybrid functional. However, as because Co-Cy-Cl shows the metallic behavior, hybrid calculation cannot work well for metallic system. Hence, here we are presenting only GGA calculation for Co-Cy structure. The GGA calculation of orbital projected partial and total density of states of other cytemine can be found in Appendix C (Figure C.2, C.3, C.4, and C.5). Here, we will present the partial DOS of the transition metals to show their behaviors in VB and CB and how they differ from each other. Also, we have presented the partial DOS of Cl atom as well as S atom because these atoms are bonded with Cu atoms and has higher contribution in the DOS. The partial DOS of all other atoms can be found in Appendix C (Figure C.6, C.7, and C.8).

Figure 5.2 shows the density of states of Co-Cy-Cl where (a) presents the partial DOS of singlet state and (b) is the DOS plot of triplet state of Co-Cy-Cl calculated with GGA functional. Spin-polarized calculations were performed, but for singlet state only spin-up DOS is plotted. However, for triplet state, we have presented spin up and spin down where spin-up and spin-down channels are presented along the positive and negative vertical axes, respectively. It is noticable that the most contribution in both VB and CB is coming from Co1-d orbital, Co2-d orbital and some contribution from S-p orbital. These continuous band in VBM and CBM indicates that Co-Cy-Cl does not have gap implying it shows metallic behavior. However, interestingly the Co-Cy-Cl structure remains as cysteamine structure. We have applied DFT + U theory by applying U = 4 eV on 3-d orbital of Co atoms, however, it unable to opne any gap near the Fermi level. Figure 5.3 and figure 5.4 show the partial DOS of Co1-d orbital and Co2-d orbital in Co-Cy-Cl where (a) is

DOS plot of singlet state calculated with GGA functional and (b) is the DOS plot of singlet state calculated with DFT+ U (U = 4 eV). In singlet state, around -2 to -2.5 eV, the bands remain almost same for both DOS except for the height which is reduced with DFT + U. In triplet state, we can see that Co1-d orbital shows continuous band more than what it was without U. Co-Cy-Cl may work as a catalyst because it has peak near fermi level but not at the fermi level and usually a good catalyst or good reactive material has high density of state at fermi level. The partial density of states plots of all other atoms in Co-Cy-Cl which are calculated by DFT+ U can be found in Appendix C (Figure C.2).

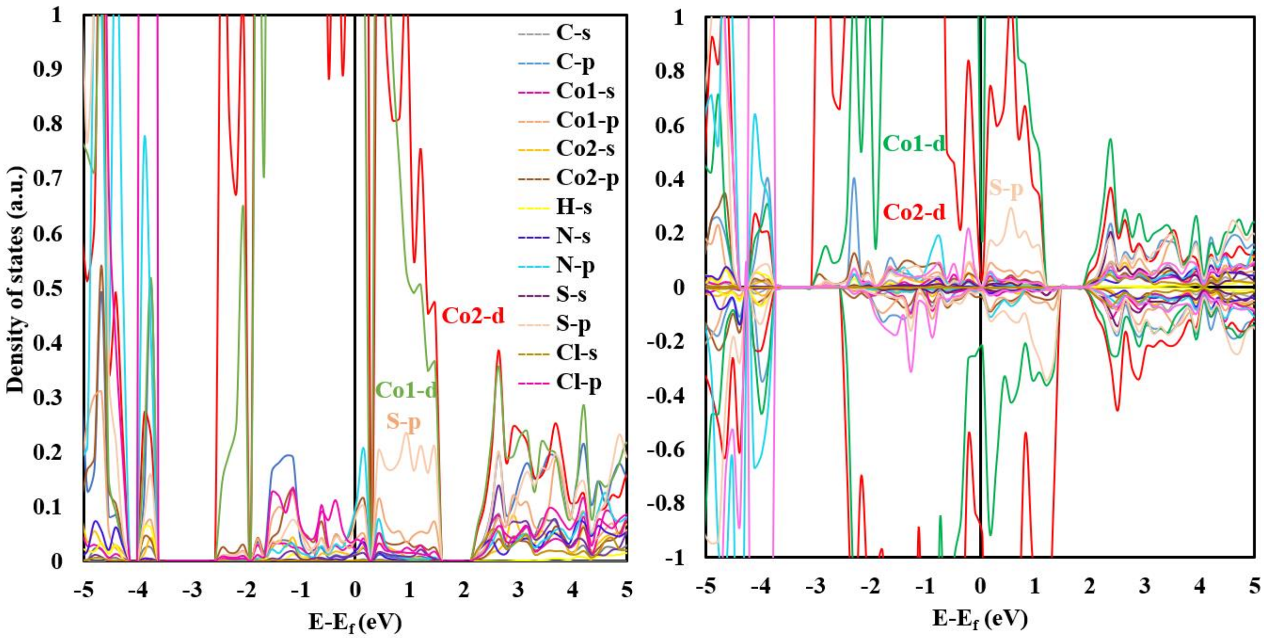

(a) Co-Cy-Cl singlet

(b) Co-Cy-Cl triplet

Figure 5.2. Density of states (partial DOS) (a) singlet state and (b) triplet state of Co-Cy-Cl calculated with GGA functional. The top of the valence band is scaled to 0 eV, which is called Fermi level. Spin-polarized calculations were performed, but for singlet state only spin-up DOS is plotted. For triplet state, the spin-up channel is presented by positive density of states and spin-down channels by the negative density of states.

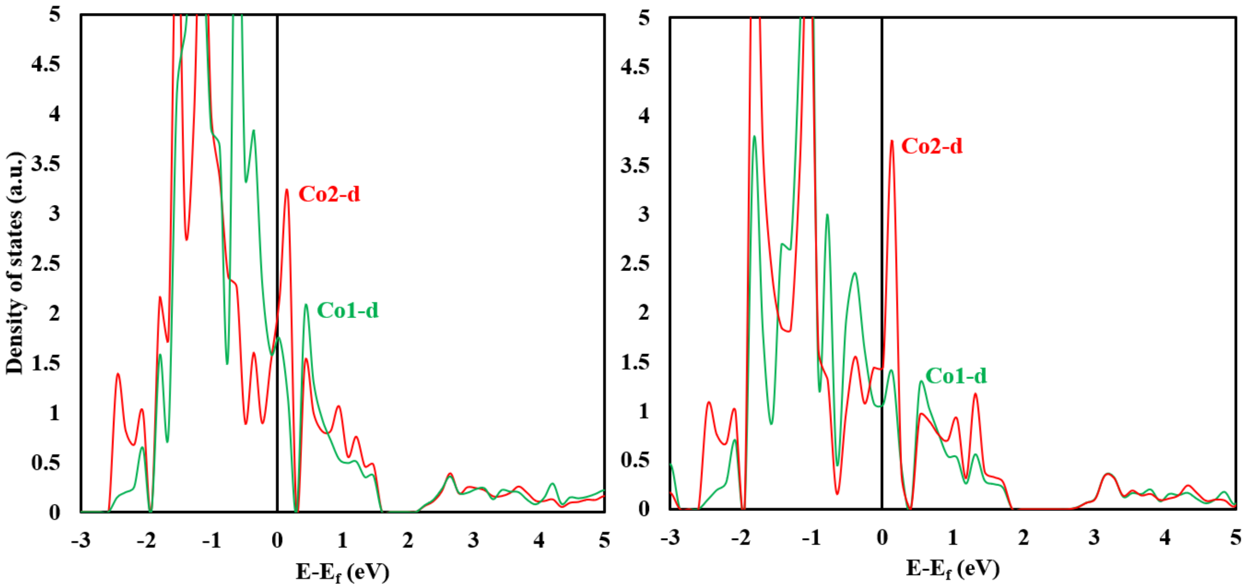

(a) Co-Cy-Cl singlet

(b) Co-Cy-Cl singlet DFT+ U (U = 4 eV)

Figure 5.3. Partial DOS of Co1-d orbital and Co2-d orbital in Co-Cy-Cl (a) singlet state calculated with GGA functional and (b) singlet state calculated with DFT+ U (U = 4 eV).

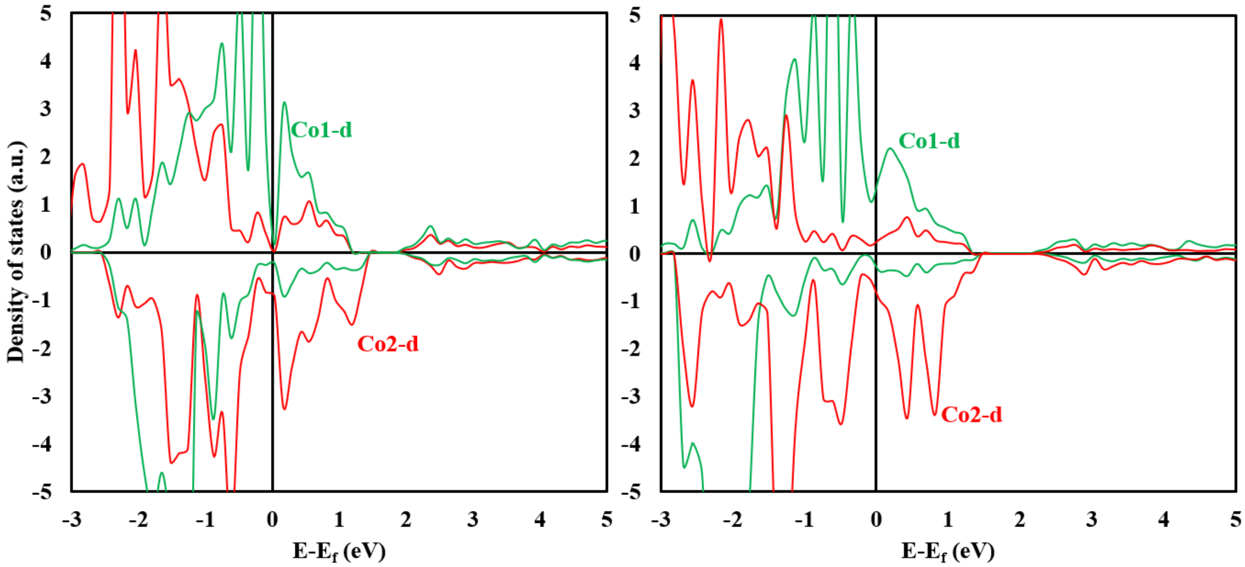

(a) Co-Cy-Cl triplet

(b) Co-Cy-Cl triplet DFT+ U (U = 4 eV)

Figure 5.4. Partial DOS of Co1-d orbital and Co2-d orbital in Co-Cy-Cl (a) triplet state calculated with GGA functional and (b) triplet state calculated with DFT+ U (U = 4 eV).

As we have mentioned above, we have calculated the density of state for Cu-Cy-Cl, Ag-Cy-Cl, Au-Cy-Cl and Zn-Cy-Cl by hybrid functional. Figure 5.5, 5.6, 5.7, and 5.8 presents the partial DOS plots of Cu-Cy-Cl, Ag-Cy-Cl, Au-Cy-Cl and Zn-Cy-Cl respectively in singlet and triplet state. For singlet state, first point to notice is that Ag-Cy-Cl behaves like Cu-Cy-Cl. From the DOS of Ag-Cy-Cl, we can see that it shows band gap in its ground state which is a singlet state as Cu-Cy-Cl. Ag-Cy-Cl has a band gap around 2.707 eV, and Cu-Cy-Cl has gap around 3.181 eV. Also, in Ag-Cy-Cl DOS plot (Figure 5.6) that Ag-d orbital is coming at the top of the valance band, and it is almost separated with S-p from the other bands. And as because Ag-d orbital is there, it brings S-p orbital because Ag is hybridized with S. Also, we can see that Ag1-d and Ag2-d behave similarly. In addition, it is noticeable that the higher contribution form S-p orbital due to the strong hybridization of S-p orbital with Ag1-d and Ag2-d orbital. The feature where Ag-d is at the top of the valance band is distinguishable features of Ag, and one of the reasons is that Ag-d orbital has higher energy than Cu-d. Now, from Cu-Cy-Cl DOS plot, Cu-d is at the top of the valance band, but it is not separated as Ag-d I or Ag-Cy-Cl. Thus, one of the reasons that the band gap is higher in Cu-Cy-Cl comparing to Ag-Cy-Cl is that Ag-d sit at the top of the valance band and that rise the valance band edge slightly. The band gap of Ag-Cy-Cl shows that Ag-Cy-Cl may react in wider range of light, but none of Ag-Cy-Cl and Cu-Cy-Cl will response in red or green light because of the high band gaps they have.

For Au-Cy-Cl singlet state, by comparing DOS shown in Figure 5.7 (a) with Cu-Cy-Cl in Figure 5.5 (a), we can see that Au-Cy-Cl behaves as Cu-Cy-Cl where the band gap that is around 2.774 eV. Also, there are contributions from Au1-d orbital and Au2-d orbital near fermi level. Also, we have notice that Au-Cy-Cl is showing similar behavior as Ag-Cy-Cl where the contribution on the top of the valance band from Au-d orbitals. Hence, the Ag-Cy-Cl and Au-Cy-Cl behave like a semiconductor in their ground state as Cu-Cy-Cl.

As we have seen for Cu-Cy that the emission spectra depend on the electronic structure of triplet state, we have plotted the DOS of triplet state of Au-Cy and Ag-Cy. By comparing triplet state of Ag-Cy-Cl with Cu-Cy-Cl shown in Figure 5.5 (b) and Figure 5.6 (b), we can see in Ag-Cy-Cl, there is a gap in the spin up channel but there is no band gap in down spin channel, and whereas in Cu-Cy-Cl there is visible gap between the mid-gap state and the top of VB in the down spin channel.

Comparing the Au-Cy-Cl DOS plot in Figure 5.7 (b) with Cu-Cy-Cl DOS plots of triplet states, we can see there is no band gap either in spin up channel or the down spin channel. We can conclude that Cu-Cy-Cl, Ag-Cy-Cl and Au-Cy-Cl in their ground state which is singlet state behave like high-gap semiconductor material. In triplet state, Cu-Cy-Cl behaves like a semiconductor with a mid-gap state and the mid gap states; for Ag-Cy-Cl, the triplet state is like half metal as because spin up channel has a gap, but the gap is zero in down spin channel; for Au-Cy-Cl, in triplet state it behaves like a metal because both spin up and down do not show any gap.

As because the difference between singlet and triplet state for example for Au-Cy is very high around 2.411 eV, if we increase the energy by around 2.411 eV, such as with high energy photon, then the semiconductor material with high gap can be a metal.

Now from the DOS plot of Zn-Cy-Cl shown in Figure 5.8, we can see that Zn-Cy-Cl is behaving differently from Co-Cy-Cl, Cu-Cy-Cl, Ag-Cy-Cl and Au-Cy-Cl. It did not give metallic behavior as Co-Cy-Cl even though both Zn-Cy-Cl and Co-Cy-Cl are stabilized in triplet state, and on the other hand, it did not give high gap in singlet state as Cu-Cy-Cl, Ag-Cy-Cl and Au-Cy-Cl.

First, we can start with partial DOS plot of Zn-Cy-Cl triplet state as we have seen earlier that the ground state of Zn-Cy-Cl structure is triplet state. It can be clearly seen that there is slight contribution from Zn (1) and Zn (2) d-orbital in the VBM and CBM, but this contribution is not dominant as Cu (1) and Cu (2) d-orbital in Cu-Cy-Cl. This can be explained by the fact that d-orbital is filled in Zn which implies the contribution from d-orbital can be seen in the deep of VB. When we apply spin-orbit-coupling on Zn in Zn-Cy-Cl, it should not be as Cu in Cu-Cy-Cl because Cu has partially d-orbital occupied, but Zn has filled d-orbital. Also, we can see the highest contribution is coming from S-p orbital in spin up and spin down channel in both CBM as well as in VBM which means Zn-Cy-Cl may not reactive as when d-orbital presents in VB as in Cu-Cy-Cl. We can see also Zn (1) which bonds to Cl try to hybridize with Cl-p, it goes up with Cl-p. In addition, the bands are not continuing in the top of fermi level, fermi level is zero and nothing is occupied above Fermi in both spin up and down. We can see there is a gap in the spin up around 0.810 eV and gap in spin down around 1.754 eV. This means Zn-Cy-Cl in triplet is not metal because there is clear gap, and it behaves like a semiconductor even though it has a mid-gap.

Now, from partial DOS of Zn-Cy-Cl singlet state, we can see the contribution from Zn (1) and Zn (2)-d orbital near fermi level and in the top of valance band VBM as well as in CBM is not high as the contribution from Cu (1) and Cu (2) d-orbital in Cu-Cy-Cl which is same as what we saw in triplet state. Moreover, the highest contribution is coming from S-p orbital which is dominant in both VBM and CBM. Also, it is noticeable that there are bands on the top of the VBM from S-p orbital as well as from Zn (1) and Zn (2) atoms. This means Zn-Cy-Cl in singlet state behaves like a metal. Point to be noticed, the metallic does not necessary imply the material does not have catalytic behavior.

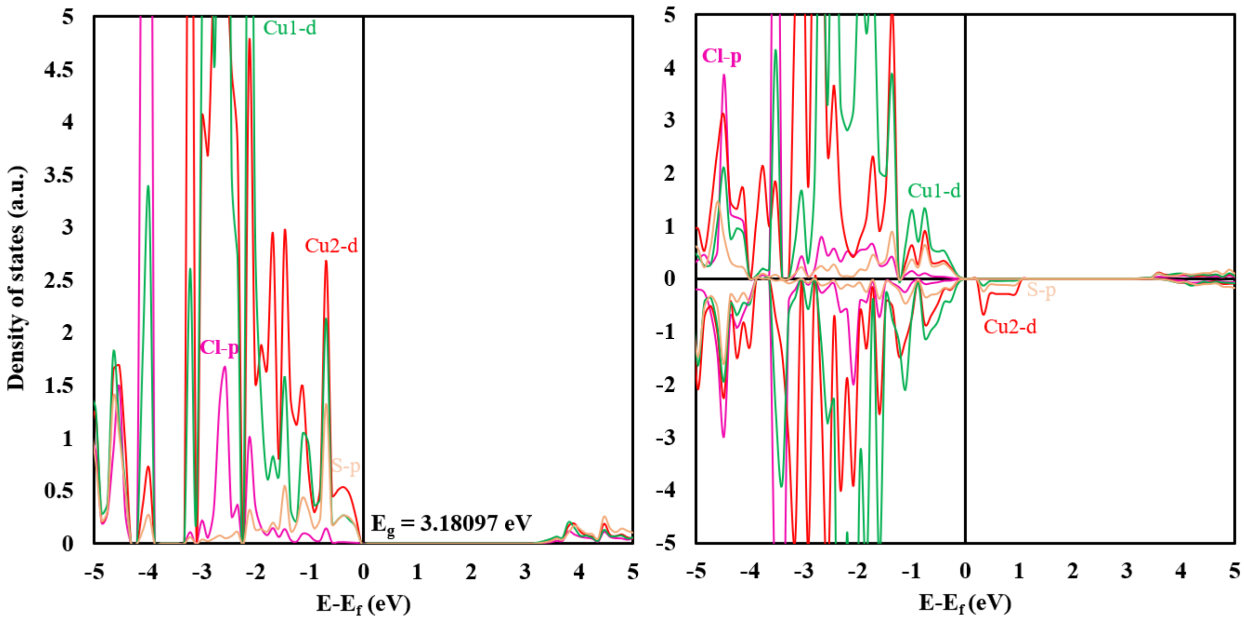

(a) Cu-Cy-Cl singlet (b) Cu-Cy-Cl triplet

Figure 5.5. Density of states (partial DOS) (a) singlet state and (b) triplet state of Cu-Cy-Cl calculated with hybrid functional (HSE06).

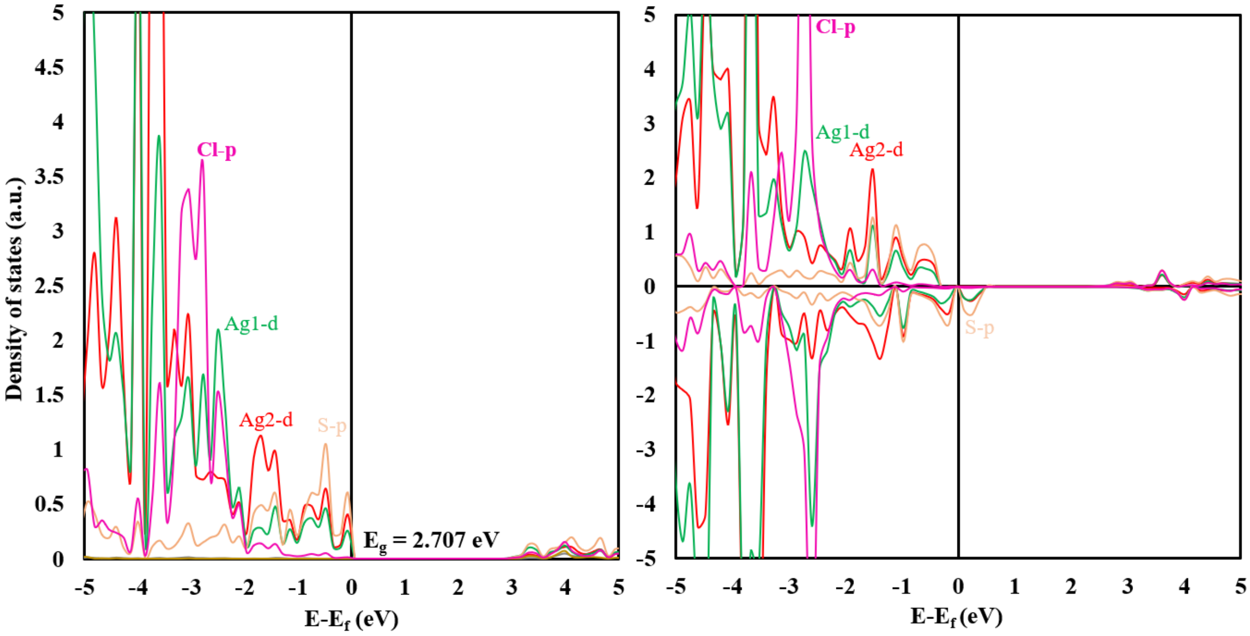

(a) Ag-Cy-Cl singlet (b) Ag-Cy-Cl triplet

Figure 5.6. Density of states (partial DOS) (a) singlet state and (b) triplet state of Ag-Cy-Cl calculated with hybrid functional (HSE06).

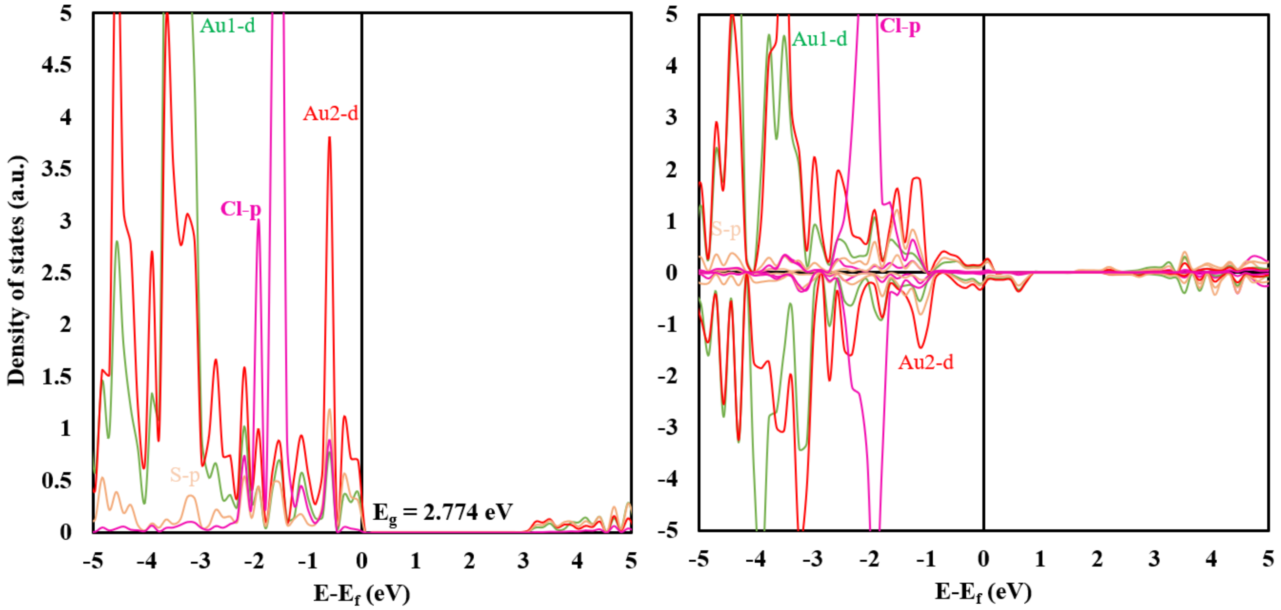

(a) Au-Cy-Cl singlet

(b) Au-Cy-Cl triplet

Figure 5.7. Density of states (partial DOS) (a) singlet state and (b) triplet state of Au-Cy-Cl calculated with hybrid functional (HSE06).

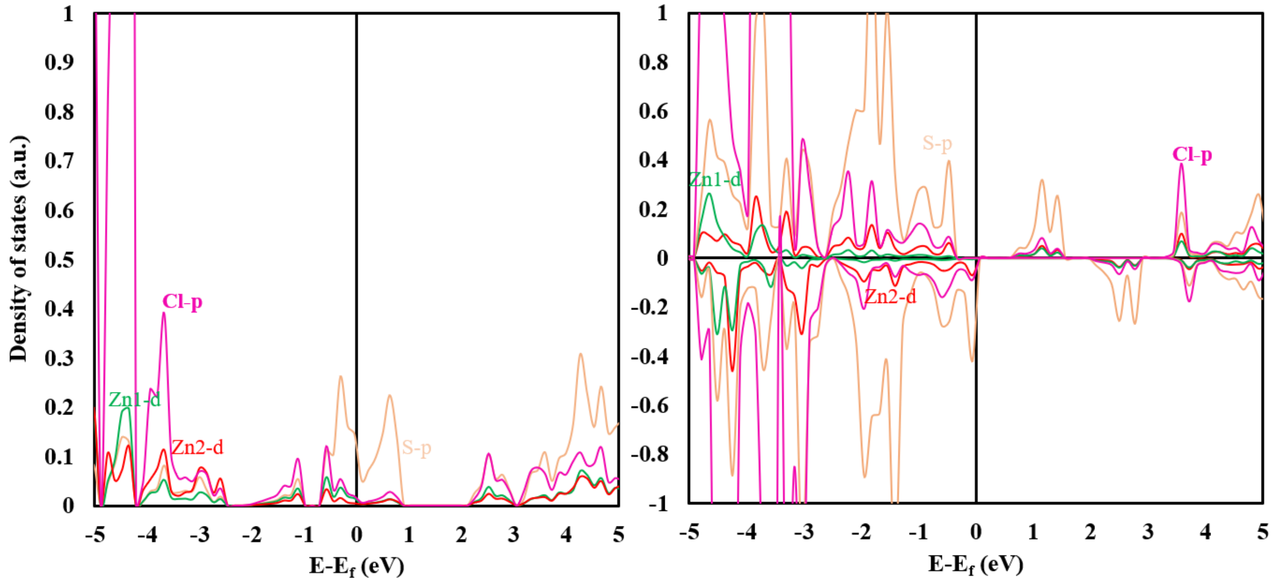

(a) Zn-Cy-Cl singlet

(b) Zn-Cy-Cl triplet

Figure 5.8. Density of states (partial DOS) (a) singlet state and (b) triplet state of Zn-Cy-Cl calculated with hybrid functional (HSE06).

5.2.4. Optical Absorption of M-Cy-Cl

Optical absorption coefficients of M-Cy-Cl structures have been calculated theoretically. We consider both singlet and triplet state as we have seen that triplet state is the ground state of Co-Cy-Cl and Zn-Cy-Cl. We have checked the quality of our theoretical results and the capability of our model to accurately represent the M-Cy-Cl structures by comparing the optical gap of Cu-Cy-Cl with the maximum of the first absorption peak in the experimental spectrum of Cu-Cy-Cl [147]. Our computed optical gap was in a good agreement with the experimental optical absorption [147]. However, the cysteamine structures with other metals are not synthesized yet. As we mentioned earlier that Co-Cy-Cl behaves like a metal, hybrid calculation cannot work well for metallic system. Hence, we have calculated the optical absorption coefficients of Co-Cy-Cl with GGA functional which is presented in Figure 5.9 for both singlet and triplet state. We can see clearly in singlet state there is no optical gap. On the other hand, there is slight gap around 0.9 eV in triplet state which is the ground state of Co-Cy-Cl structure.

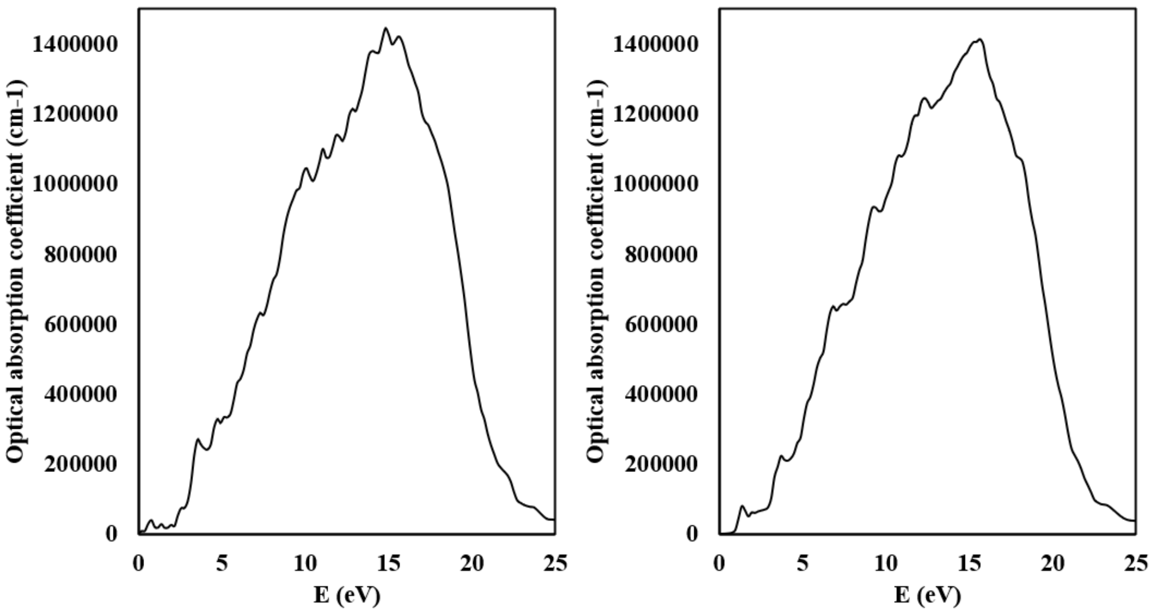

Figure 5.9. Optical absorption coefficients of Co-Cy-Cl triplet state calculated with GGA functional.

We have calculated the optical absorption coefficients of Cu-Cy-Cl, Ag-Cy-Cl, Au-Cy-Cl and Zn-Cy-Cl structures with hybrid (HSE06) functional for both singlet and triplet state shown in Figure 5.10 and Figure 5.11, respectively.

From the calculated optical absorption coefficients of singlet state in Figure 5.10, we can see that the initial absorption of Cu-Cy-Cl is 3.40 eV (364.66 nm) and this absorption energy is matching well with the experimental one that is 3.46 eV (358 nm) [147]. Also, we have seen for Ag-Cy-Cl, the optical gap is around 3.2 eV, and it is around 3.08 eV for Au-Cl-Cl.

For Zn-Cy-Cl, the optical gap is around 0.4 eV even though it did not show any gap from singlet state DOS plot.

As we have seen that triplet state is ground state of Zn-Cy-Cl, we have calculated the optical absorption coefficients of Zn-Cy-Cl of triplet state which is shown in Figure 5.11. It is noticeable that there is an optical gap around 2 eV which is slightly higher than the fundamental gap we got from the DOS plot that was in spin down around 1.754 eV.

Although triplet state is not the ground state of Cu-Cy-Cl, Ag-Cy-Cl and Au-Cy-Cl, we have calculated the optical absorption coefficients of them in triplet state which is shown in Figure 5.11. We can see that there is no optical gap in Ag-y-Cl which emphasis that the optical was calculated for spin down channel in Ag-Cy-Cl as we have seen from our DOS plot triplet state. Also, we have notice that the optical gap of Cu-Cy-Cl is higher than Au-Cy-Cl which is in a good agreement with what we found from the fundamental gap calculated from DOS plot that Cu-Cy-Cl has higher gaps than Au-Cy-Cl.

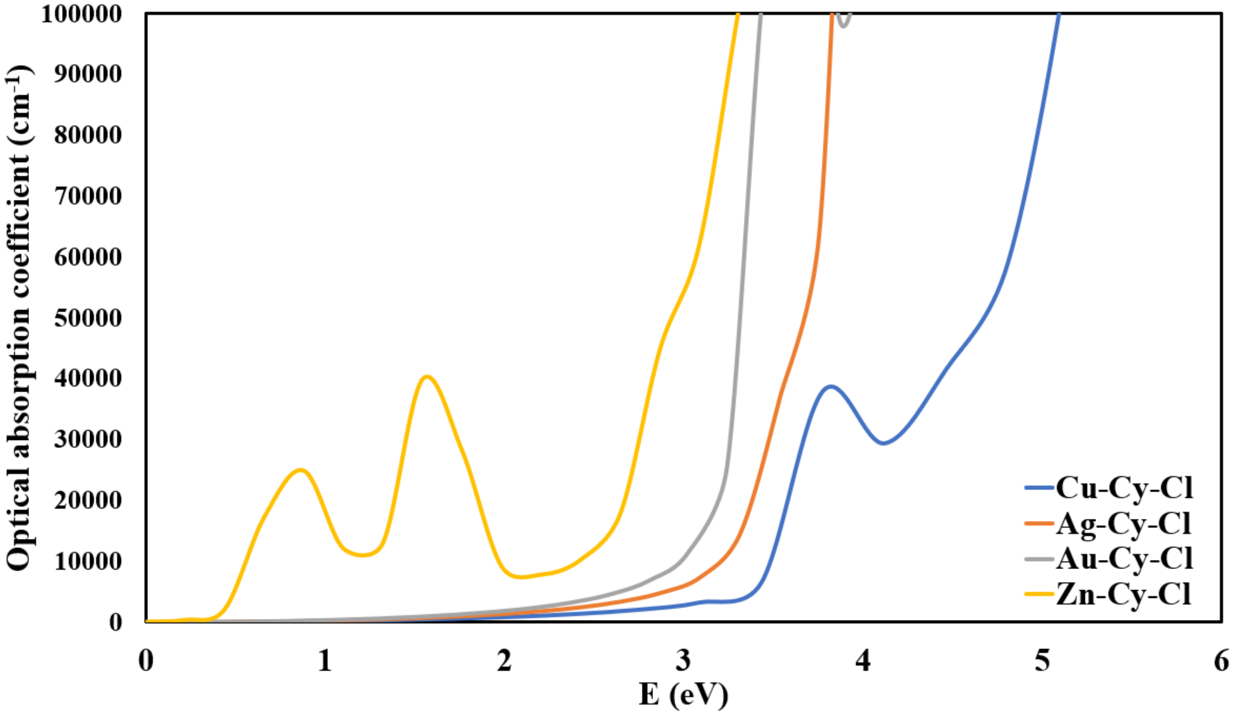

Figure 5.10. Optical absorption coefficients of M-Cy-Cl of singlet state calculated with hybrid functional (HSE06).

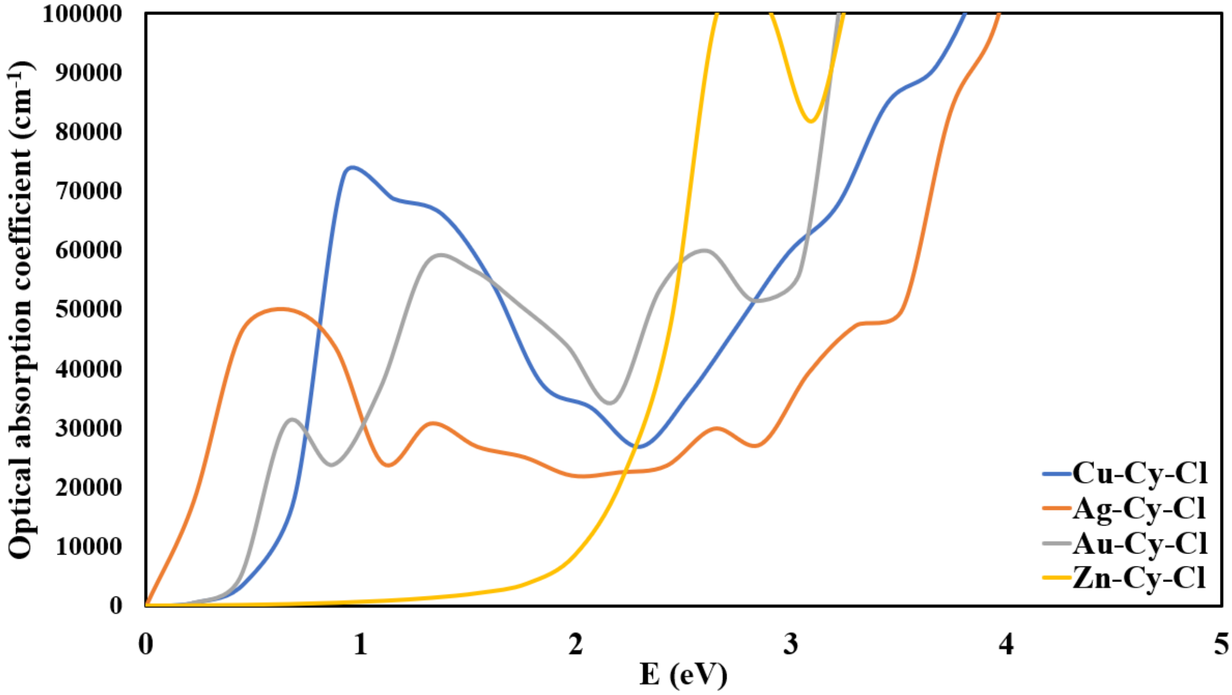

Figure 5.11. Optical absorption coefficients of M-Cy-Cl of triplet state calculated with hybrid functional (HSE06).

Chapter 6

Conclusion and Future Directions

6.1. Summary

The aim of this dissertation was to explore the possible transition metal cysteamine systems with halogens (M-Cy-X) which can be used in various applications such as technological and medical applications and as decontamination of the water from microbes and dye molecules. The study in this dissertation was performed with density functional theory (DFT).

In the first part of this dissrtation, we have studied Cu-Cy-X (X=F, Cl, Br and I) theortically and found that all Cu-Cy-X structures stabilize in singlet state. Our results indicate that Cu-Cy-F is the most stable structure thermodynamically and the stability of these Cu-Cy-X is given in order of Cu-Cy-F > Cu-Cy-Cl > Cu-Cy-Br > Cu-Cy-I. Also, we found that Cu atom in molecular solid can provide spin-orbit-coupling (SOC) which reported to be lager for Cu^{1+}, and the presense of Cu orbitals on the top of VB and the bottom of CB in DOS will help to provide spin-orbit-coupling (SOC) to the system when it is needed for non-radiative transition. This SOC allows the non-radiative transition from singlet state to triplet state to happen which is brohibited without SOC due to the diffrence in the their magnetic moments. In addition, it allows the fliping in the spin from up to dwon. Also, the reuslts show that the initial absorption leads the system to the first excited state (S_1), and after non-radiative transitions, the emission will take place from the triplet excited state (T_1). The electronic structure study of the initial and final states in the absorption and emission processes indicate that the nature of the excited states involved in these processes is mostly from Cu1 and Cu2 atoms. We have calculated the reaction barrier of Cu atoms to be out of the middle layer in all Cu-Cy-X strucutres to mimic the Cu leaching which was observed expermintally. We have found that Cu atom in Cu-Cy-I strucutres needs to face higher energy barrier in order to be out while Cu in Cu-Cy-F needs lower nergy, and the reaction barrier energy is given in order of Cu-Cy-I > Cu-Cy-Br >Cu-Cy-Cl > Cu-Cy-F. This result is in a good agreement with Cu leaching which was found expermintally. We have considered also defects in Cu-Cy-X strucutres such as Cu_v ,and X_v. At rich condition, it is less probable to form Cu_v and X_v. However, at poor condition, it is more probable to form these vacancies due to the fact that the system does not have enough atoms. We have found that in Cu-Cy-F, it less probable to form F_v ,but it is more probable to form Cu_v.

As the experimental synthesis of all Cu-Cy-X samples structures contained Cl as impurity, it is imperative to understand the effect of Cl in the stability and properties of Cu-Cy-X. In the second part of this distraction, we have studied the mixed halogen in Cu-cysteamine Cu-Cy-X1$_n$-X2$_m$ (X1 =Cl and X2 = F, Br, and I) and (n = 1,4, and 7 and m = 8 – n). We have studied the stability of Cu-Cy-X1$_n$-X2$_m$ structures and their electronic and optical properties and see in what ways mixing of the halogens affect these properties. First, we have seen that all Cu-Cy-X1$_n$-X2$_m$ structures stabilize in singlet state as the prisitne strucutre of Cu-Cy-X. We have found that mixing Cu-Cy-Br and Cu-Cy-I with Cl can increase the stability of the structures thermodynamically. However, the presence of Cl in Cu-Cy-F lower the thermodynamic stability. In addition, we have explored that the presence of Cl in Cu-Cy-X2 (X2 = F, Br, and I) may help in making the material harder than when we have pure Cu-Cy-X (X = F, Br, and I) structure.

In the last part of this dissertation, we have discovered other possible transition metals cysteamine systems such as Ag and Au which have same number of valance electrons and Co, and Zn which have different number of valance electrons. We have studied the stability of M-Cy-X materials where M= Co, Ag, Au, Zn and X = F, Cl, Br, and I.

We have seen that Ag-Cy-X, and Au-Cy-X structures are stabilized in singlet state as Cu-Cy-X while Co-Cy-X and Zn-Cy-X stabilize in triplet state. This indicates that the excitation and emission spectra of Co-Cy-X and Zn-Cy-X will be completely different from Cu-Cy-X structure. By comparing the stability of M-Cy-X structures with respect to the halogens X, the stability is given in order of M-Cy-F > M-Cy-Cl > M-Cy-Br > M-Cy-I. When we compare the stability of structures with respect to the transition metal M, we can see that the stability of M-Cy-X is given in order of Cu-Cy-Cl > Zn-Cy-Cl > Ag-Cy-Cl > Au-Cy-Cl > Co-Cy-Cl. Also, we have seen Cu-Cy-Cl, Ag-Cy-Cl and Au-Cy-Cl in their ground state which is singlet state behave like high-gap semiconductor material. However, in triplet state, Cu-Cy-Cl behaves like semiconductor with a mid-gap state in spin down channel. For, Ag-Cy-Cl, the triplet state behaves like half metal as because spin up channel has a gap, but the gap is zero in down spin channel. For Au-Cy-Cl, it is a metal in triplet state because both spin up and down do not show any gap. Also, we have seen that Ag-Cy-Cl and Au-Cy-Cl have lower gap than Cu-Cy-Cl where the gap of these materials is given in order of Cu-Cy-Cl > Au-Cy-Cl > Ag-Cy-Cl which are 3.18 eV, 2.774 eV and 2.707 respectively. These gaps indicate that Ag-Cy-Cl can be activated by the visible blue light while Cu-Cy-Cl and Au-Cy-Cl can be activated the visible violet light.

6.2. Conclusion

In this dissertation, we were successfully able to explain the optical-emission phenomena when experimental data shows lower emission spectra than the optical absorption. We were capable to show that Cu-Cy-I is kinetically more stable comparing to Cu-Cy-Cl which means it is better to use Cu-Cy-I in application that require materials to stay in aqueous solution for longer time without dissociated. Also, adding small concentration of Cl to Cu-Cy-I can help to make the material harder.

We have discovered that mixed halogens cysteamine strucutres have lower optical gap than pristine structures, and it has very high absorption coefficient. This indicates that mixed halogen cysteamine system is more useful for solar light absorption.

Also, we have reported theoretically for the first time cysteamine systems with other transition metals such as Zn, Ag, and Au that can be used in technological applications. We have found from the stability and optical absorption point view that Ag-Cy-Cl will work as good as Cu-Cy structure as Ag-Cy structure has high thermodynamic stability and the structure remains same as Cu-Cy. Also, the diffusion of Ag in Ag-Cy will be less comparing to Cu in Cu-Cy because Ag is heavier than Cu. In addition, we can propose that Ag-Cy can be a good candidate because it has similar optical profile as Cu-Cy with mixed halogens and Ag is less toxic comping to Cu atom.

We have discovered new metallic compound which is Co-Cy-X. We suggest that Co-Cy may work as a catalyst because usually the good catalyst or good reactive material has high density of state at fermi level. These new discovery of transition metal cysteamine systems and the predicted properties can help to guide the experiment to understand these materials before their synthesis.

6.3. Future Works

To make transition metals cysteamine systems work efficient at sunlight, its reaction kinetics can be improved by cocatalyst. The cocatalyst can be embedded either on the surface of the Cu-Cy particles or in the interlayer gaps. This would open the door for interesting work to be done on M-Cy-X. In addition, as DFT calculations are performed at 0 K, it is imperative to incorporate molecular dynamic on cysteamine systems to predict their dynamical stability and higher temperature effects for these systems. The cysteamine with Co, Ag, Au and Zn metals which are shown in this dissertation are stable at 0 K, but they are not synthesis yet. Hence, further investigation at higher temperature is needed as they are promising to be used in technological applications.

Appendix A

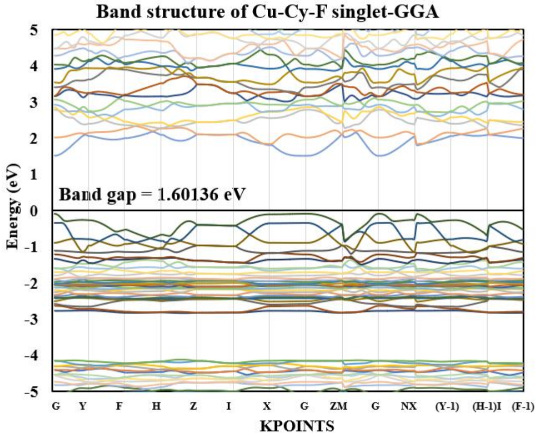

Figure A.1. Band structure of Cu-Cy-F of singlet state calculated by GGA functional.

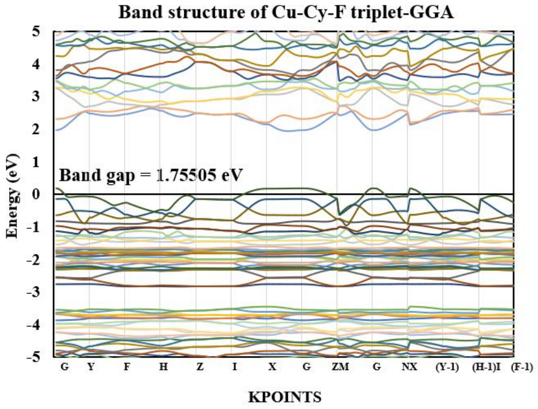

Figure A.2. Band structure of Cu-Cy-F of triplet state calculated by GGA functional.

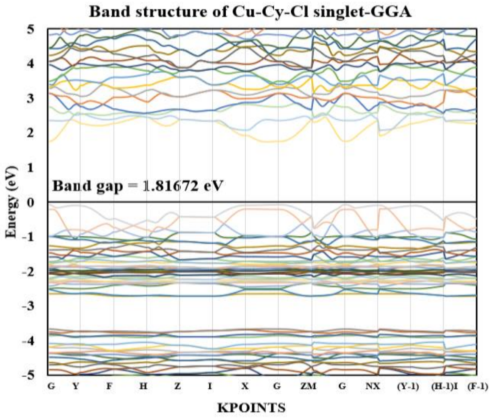

Figure A.3. Band structure of Cu-Cy-Cl of singlet state calculated by GGA functional.

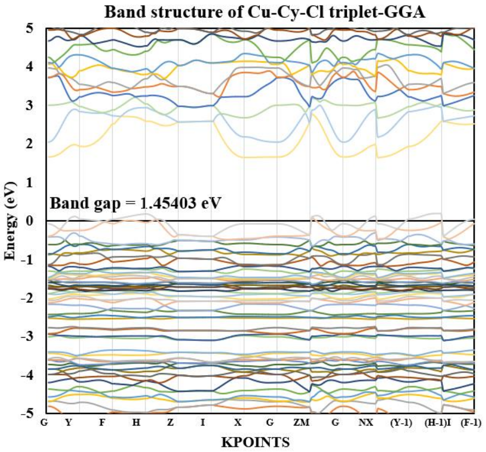

Figure A.4. Band structure of Cu-Cy-Cl of triplet state calculated by GGA functional.

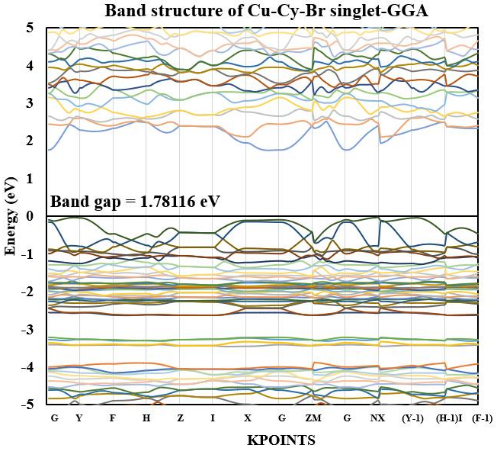

Figure A.5. Band structure of Cu-Cy-Br of singlet state calculated by GGA functional.

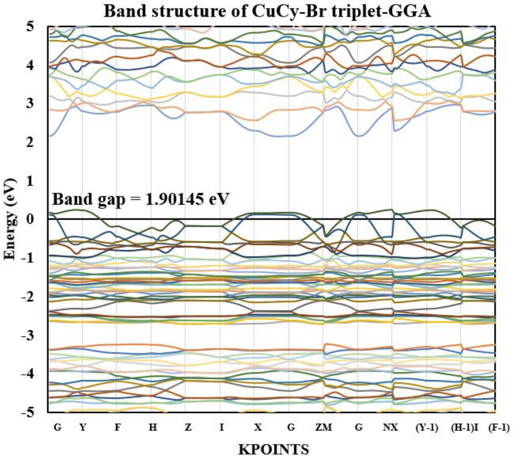

Figure A.6. Band structure of Cu-Cy-Br of triplet state calculated by GGA functional.

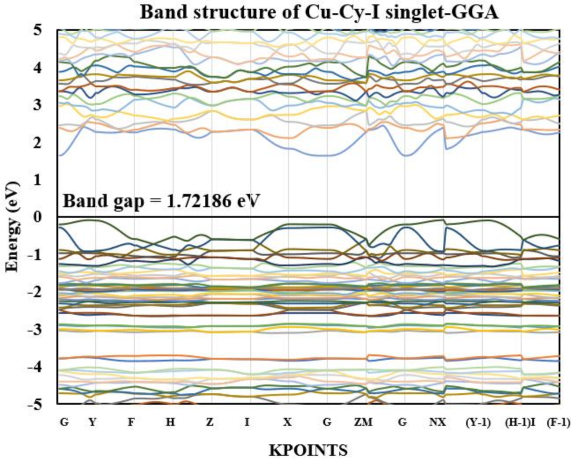

Figure A.7. Band structure of Cu-Cy-I of singlet state calculated by GGA functional.

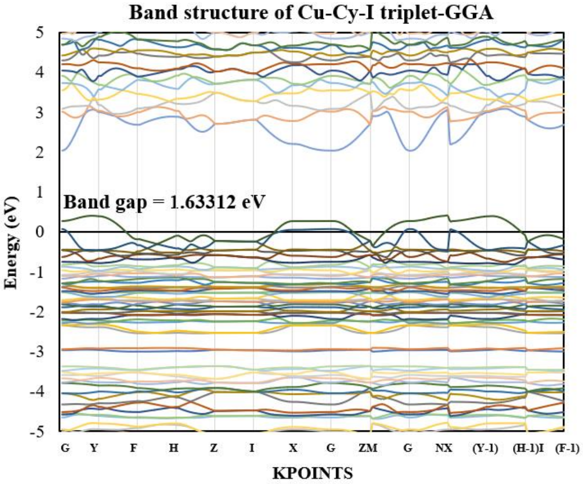

Figure A.8. Band structure of Cu-Cy-I of triplet state calculated by GGA functional.

Table A. 1. Lattice parameters and angels of Cu-Cy-X (X= Cl, Br, and I) of singlet states calculated by GGA functional

GGA/singlet	a (Å)	b (Å)	c (Å)	α (°)	β (°)	γ (°)
Cu-Cy-F	8.68834	8.68834	7.71364	95.6501	95.6501	130.8287
Cu-Cy-Cl	9.21903	9.21903	7.69901	95.5473	95.5473	132.2496
Cu-Cy-Br	9.39036	9.39036	7.66397	95.7979	95.7979	132.1817
Cu-Cy-I	9.71946	9.71946	7.63439	96.0996	96.0996	132.6065

Table A.2. Lattice parameters and angels of Cu-Cy-X (X= Cl, Br, and I) of triplet states calculated by GGA functional

GGA/triplet	a (Å)	b (Å)	c (Å)	α (°)	β (°)	γ (°)
Cu-Cy-F	8.80503	8.80503	7.73776	95.6566	95.6566	132.2702
Cu-Cy-Cl	8.89973	8.89973	8.95392	91.7755	91.7755	138.9621
Cu-Cy-Br	9.54132	9.54132	7.61127	95.9129	95.9129	132.7854
Cu-Cy-I	9.81806	9.81806	7.51806	96.2570	96.2570	132.0116

Table A.3. Total energy of singlet and triplet state of Cu-Cy-X calculated by GGA functional

Pristine/GGA	E (eV) - singlet	E (eV) - triplet
Cu-Cy-F	-247.386	-245.140
Cu-Cy-Cl	-245.273	-242.757
Cu-Cy-Br	-244.314	-241.916
Cu-Cy-I	-243.245	-240.866

Table A.4. Total energy of X_v in Cu-Cy-X calculated by GGA functional

Structure/GGA	X_v
Cu-Cy-F	-240.056
Cu-Cy-Cl	-239.187
Cu-Cy-Br	-238.683
Cu-Cy-I	-238.112

Table A.5. The formation energy for X_v defects in Cu-Cy-X strucutres calculated by GGA functional

Structure	X_v Defect formation energy (eV)	
	rich	poor
Cu-Cy-F	5.472	-2.5
Cu-Cy-Cl	4.207	-2.6875
Cu-Cy-Br	4.134	-2.663
Cu-Cy-I	3.805	-2.6265

Table A.6. Bader charge of N atoms in Cu-Cy-Cl

Atom	Pristine	Cu1-vacancy	Cu2-vacancy
N	-1.231049	-1.248088	-1.221857
N	-1.231049	-1.220181	-1.255888
N	-1.231028	-1.220181	-1.175034
N	-1.231028	-1.248088	-1.192488

Table A.7. Bader charge of N atoms in Cu-Cy-Br

Atom	Pristine	Cu1-vacancy	Cu2-vacancy
N	-1.275731	-1.24613	-1.191522
N	-1.275731	-1.266621	-1.240112
N	-1.275712	-1.266621	-1.245537
N	-1.275713	-1.24613	-1.193069

Table A.8. Bader charge of N atoms in Cu-Cy-I

Atom	Pristine	Cu1-vacancy	Cu2-vacancy
N	-1.246454	-1.211975	-1.25656
N	-1.246454	-1.248163	-1.313846
N	-1.246444	-1.248163	-1.23408
N	-1.246444	-1.211975	-1.222411

Appendix B

Table B.1. Atomic weight % of the elements in Cu-Cy-Cl_n-F_m

Atomic wt %	Cu-Cy- Cl_1-F_7	Cu-Cy- Cl_4-F_4	Cu-Cy- Cl_7-F_1
Cu	52.3769	51.5037	50.6592
F	4.56726	2.56635	0.63107
Cl	1.21757	4.78908	8.24347
C	13.1995	12.9795	12.7667
H	3.32279	3.2674	3.21382
N	7.69655	7.56824	7.44415
S	17.6194	17.3257	17.0416

Table B.2. Atomic weight % of the elements in Cu-Cy-Cl_n-Br_m

Atomic wt %	Cu-Cy- Cl_1-Br_7	Cu-Cy- Cl_4-Br_4	Cu-Cy- Cl_7-Br_1
Cu	45.6874	47.5885	49.6547
Br	16.7557	9.97312	2.60153
Cl	1.06206	4.42502	8.08001
C	11.5137	11.9928	12.5135
H	2.89841	3.01902	3.15009
N	6.71356	6.99292	7.29653
S	15.3691	16.0086	16.7037

Table B.3. Atomic weight % of the elements in Cu-Cy-Cl$_n$-I$_m$

Atomic wt %	Cu-Cy-Cl$_1$-I$_7$	Cu-Cy-Cl$_4$-I$_4$	Cu-Cy- Cl$_7$-I$_1$
Cu	41.5885	44.9515	48.9063
I	24.2242	14.9617	4.06951
Cl	0.96678	4.17982	7.95822
C	10.4807	11.3283	12.3249
H	2.63837	2.85172	3.10262
N	6.11124	6.60542	7.18656
S	13.9902	15.1215	16.4519

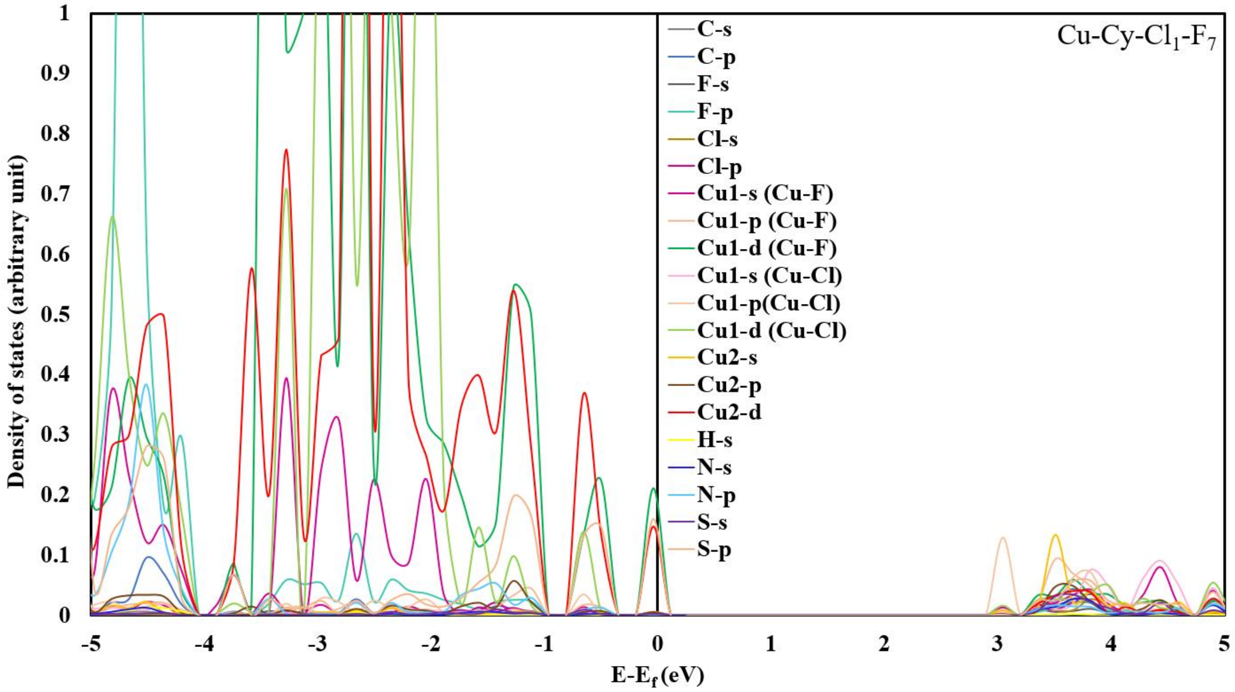

Figure B.1. Partial density of states (DOS) of Cu-Cy-Cl$_1$-F$_7$ of singlet state calculated with hybrid functional (HSE06). The top of the valence band is scaled to 0 eV, which is called fermi level. For singlet state (S_0) only spin-up DOS is plotted.

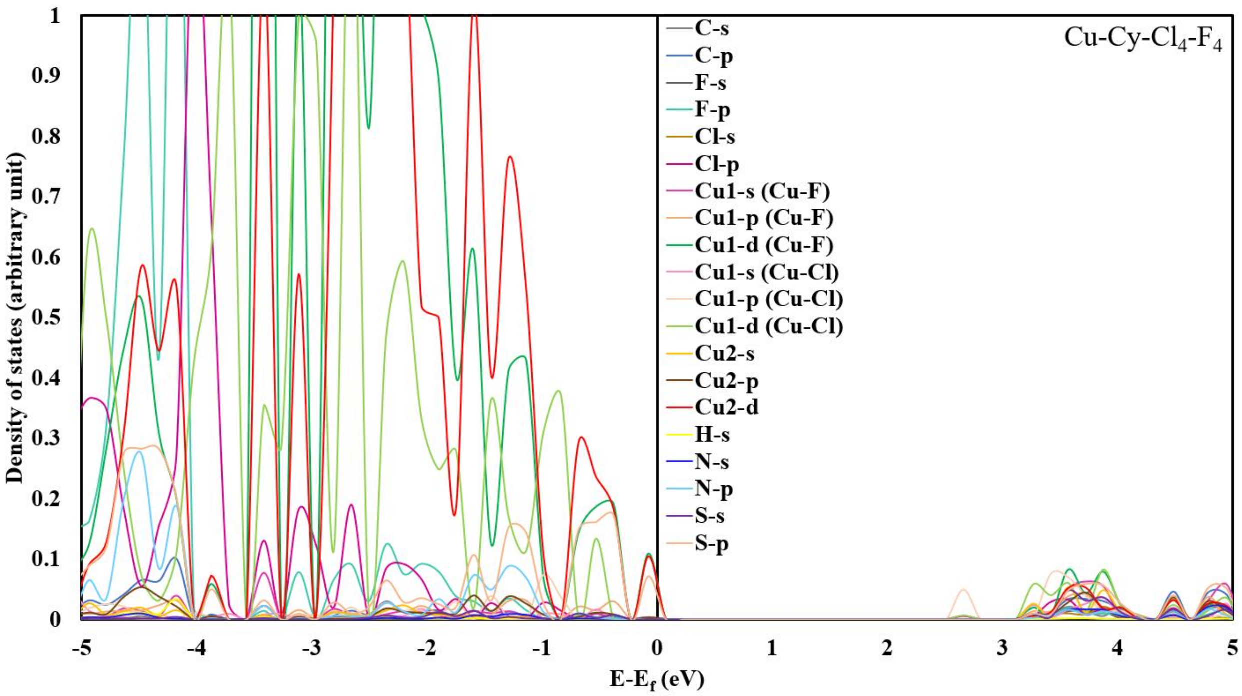

Figure B.2. Partial density of states (DOS) of Cu-Cy-Cl$_4$-F$_4$ of singlet state calculated with hybrid functional (HSE06).

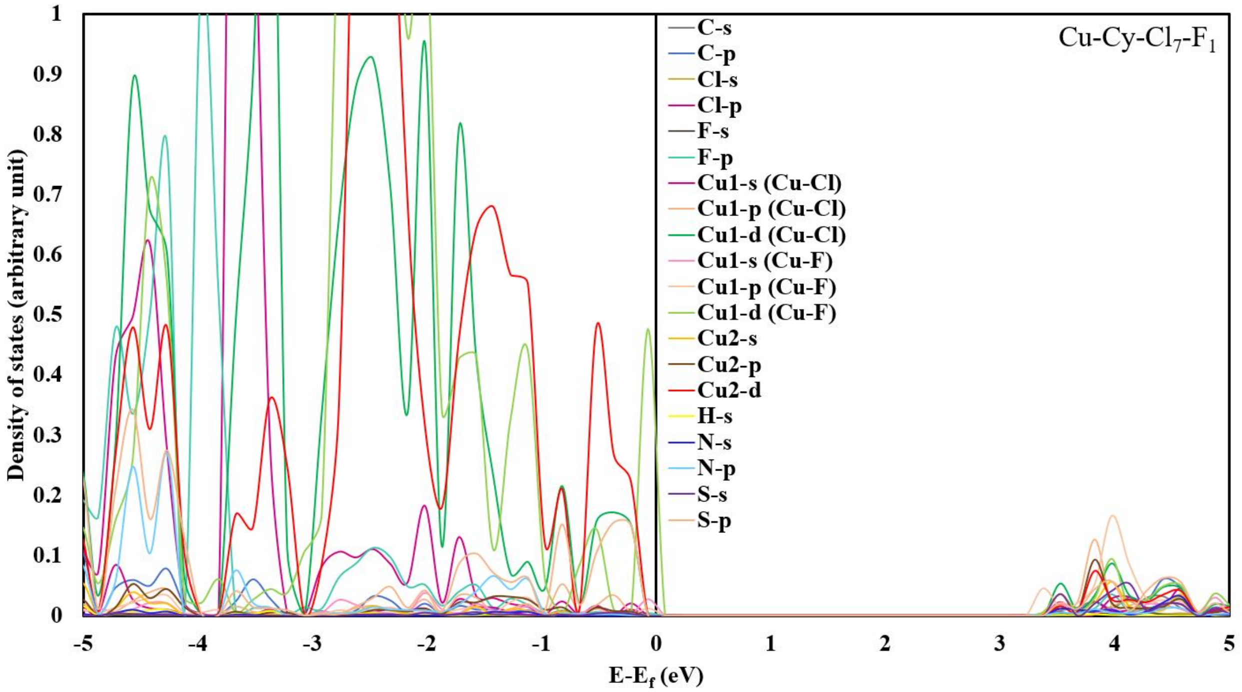

Figure B.3. Partial density of states (DOS) of Cu-Cy-Cl$_7$-F$_1$ of singlet state calculated with hybrid functional (HSE06).

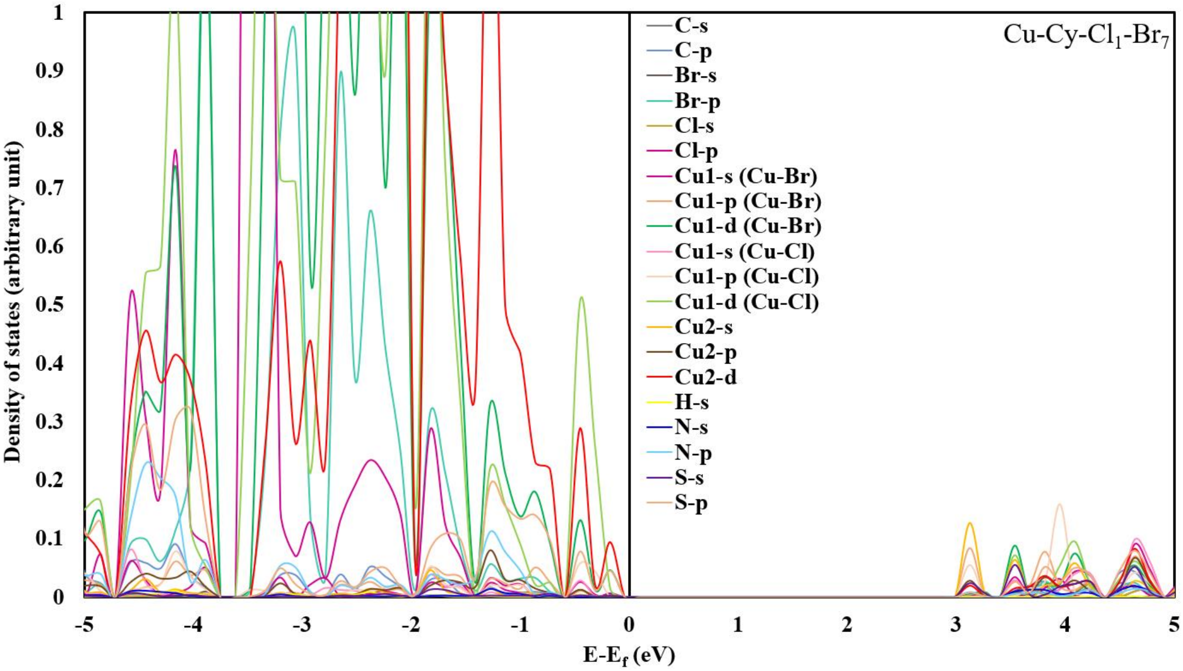

Figure B.4. Partial density of states (DOS) of Cu-Cy-Cl$_1$-Br$_7$ of singlet state calculated with hybrid functional (HSE06).

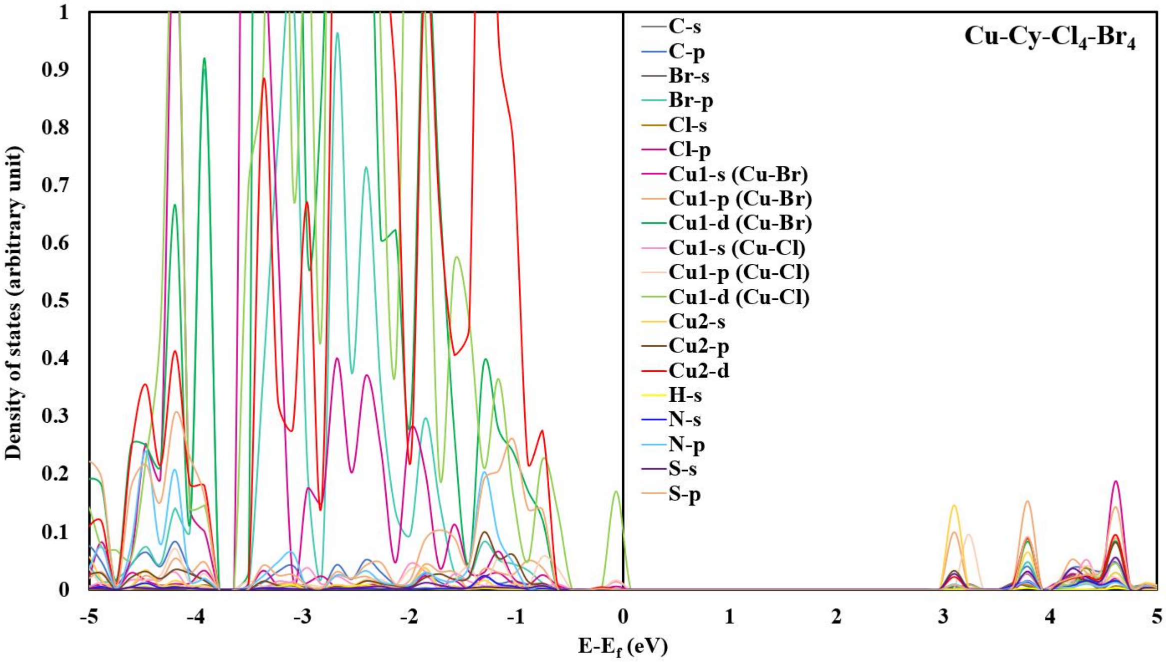

Figure B.5. Partial density of states (DOS) of Cu-Cy-Cl$_4$-Br$_4$ of singlet state calculated with hybrid functional (HSE06).

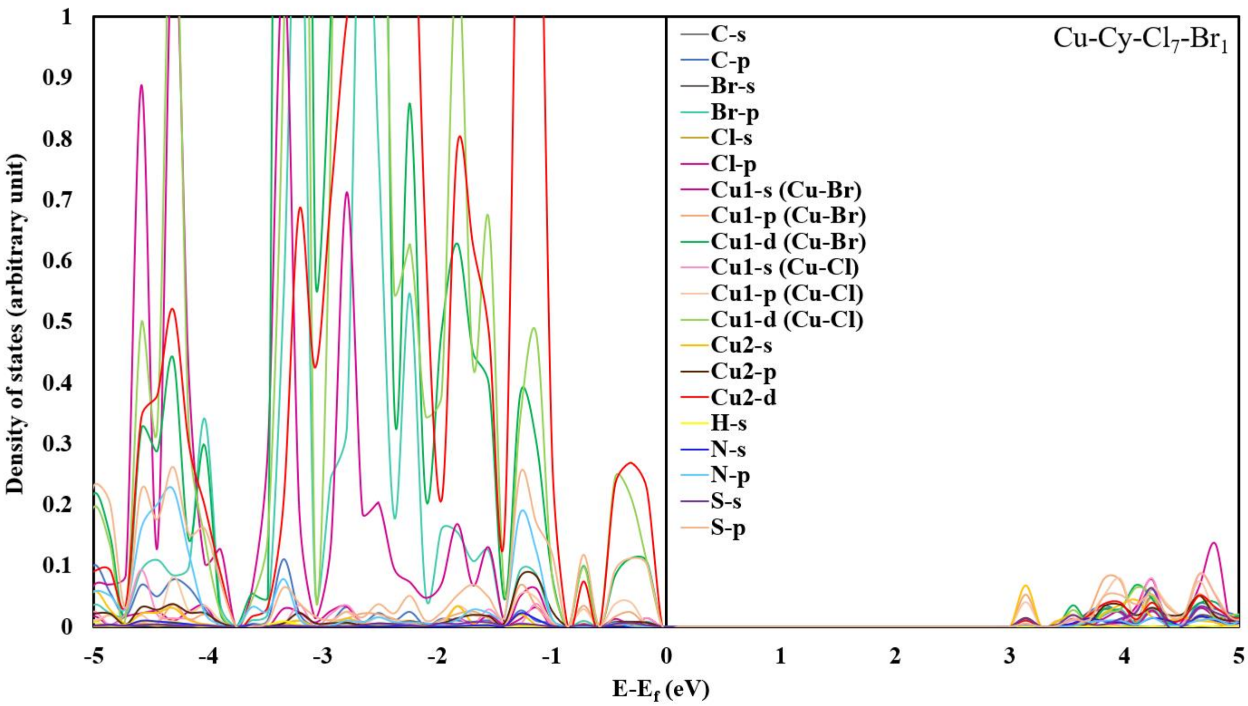

Figure B.6. Partial density of states (DOS) of Cu-Cy-Cl_7-Br_1 of singlet state calculated with hybrid functional (HSE06).

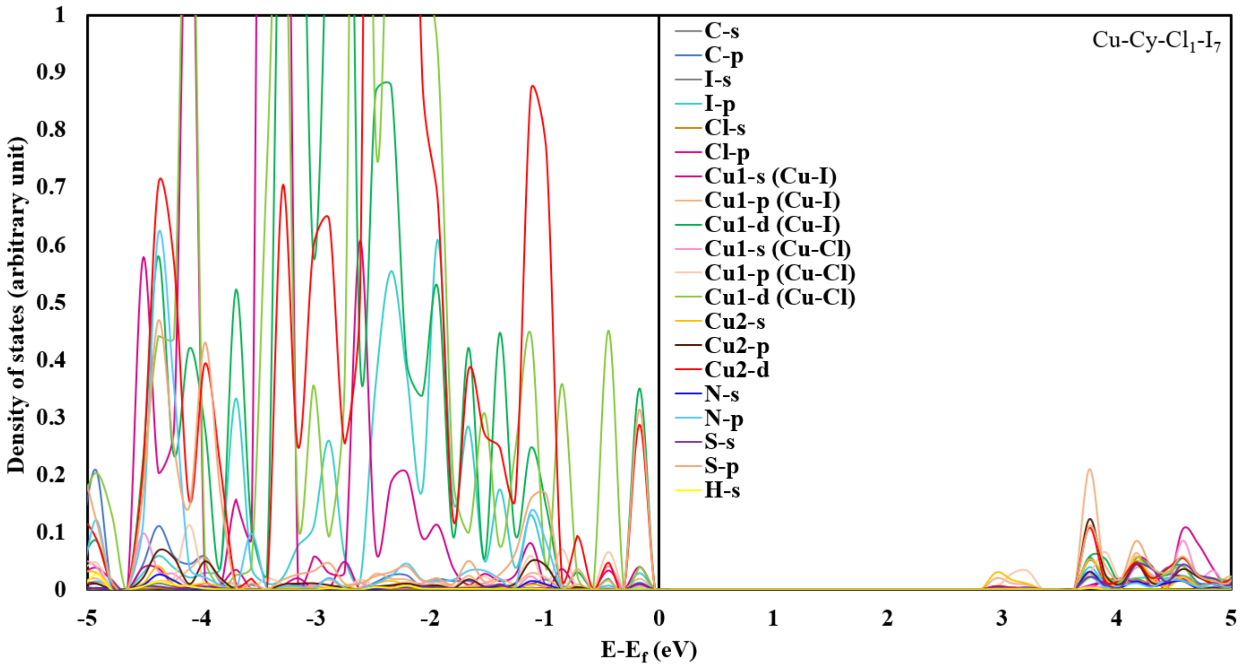

Figure B.7. Partial density of states (DOS) of Cu-Cy-Cl_1-I_7 of singlet state calculated with hybrid functional (HSE06).

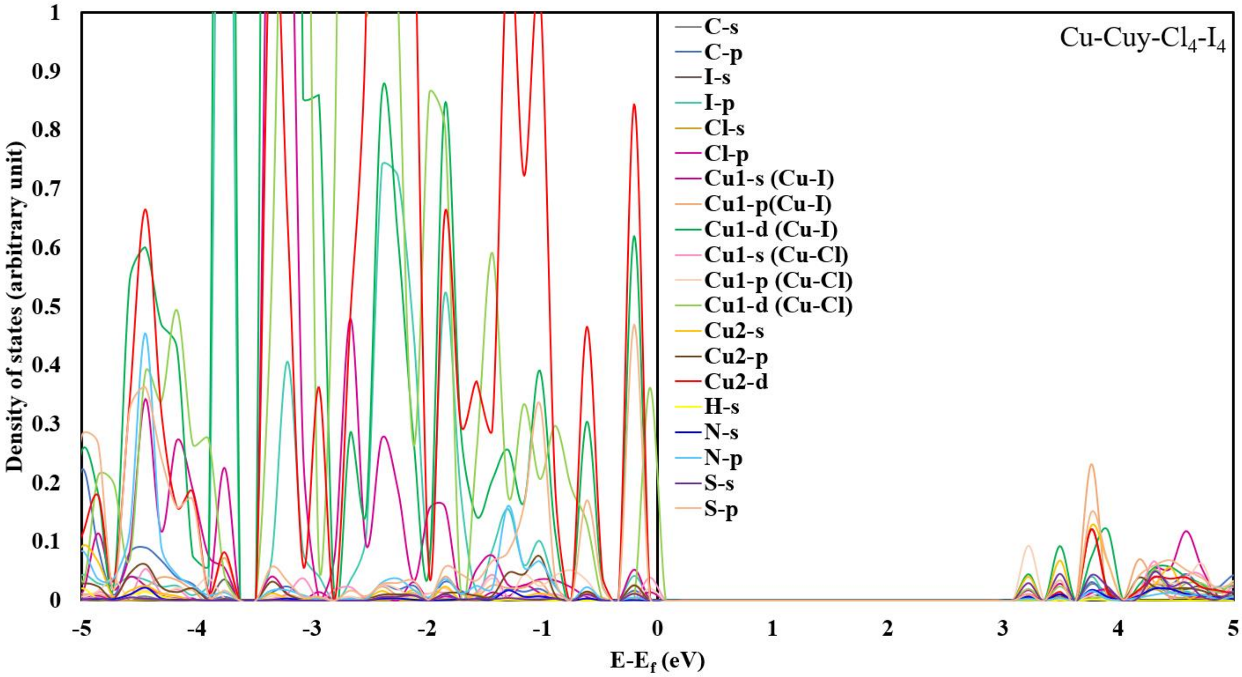

Figure B.8. Partial density of states (DOS) of Cu-Cy-Cl$_4$-I$_4$ of singlet state calculated with hybrid functional (HSE06).

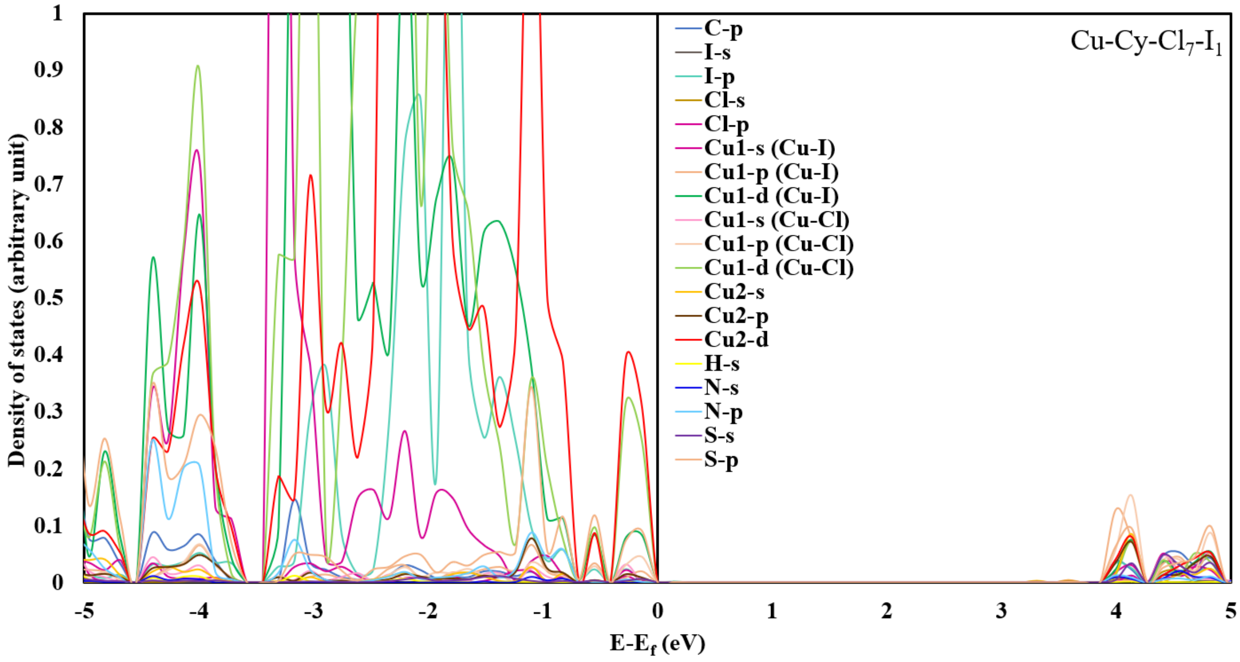

Figure B.9. Partial density of states (DOS) of Cu-Cy-Cl$_7$-I$_1$ of singlet state calculated with hybrid functional (HSE06).

Table B.4. The volume and energy of Cu-Cy-Cl_n-F_m structures GGA calculations to calculate the bulk modulus

Cu-Cy-Cl_7-F_1		Cu-Cy-Cl_4-F_4		Cu-Cy-Cl_1-F_7	
V (Å^3)	E (eV)	V (Å^3)	E (eV)	V (Å^3)	E (eV)
1725.34	-978.6713301	1682.01	-981.4061649	1652.02	-984.4908394
1749.54	-979.1104828	1705.99	-981.8557766	1675.86	-984.9429898
1773.93	-979.4535413	1730.17	-982.248336	1699.89	-985.3278546
1798.53	-979.7342221	1754.54	-982.5377387	1724.12	-985.6594109
1823.32	-979.9425041	1779.12	-982.7095376	1748.55	-985.886013
1848.31	-980.0539542	1803.89	-982.8235076	1773.17	-986.0527896
1873.5	-980.1109312	1828.87	-982.887833	1798	-986.1563107
1898.89	-980.0983492	1854.04	-982.8783133	1823.02	-986.1829667
1924.48	-979.9774621	1879.41	-982.8152837	1848.25	-986.1360537
1950.28	-979.824815	1904.99	-982.7270413	1873.68	-986.0577794
1976.28	-979.6491941	1930.77	-982.5762302	1899.31	-985.9001827

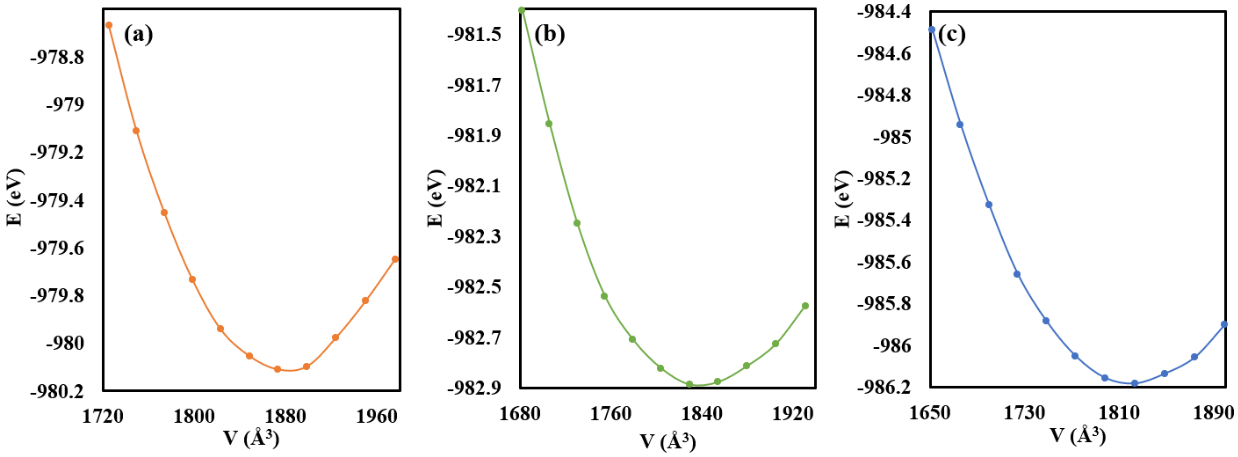

Figure B.10. E-V plots of Cu-Cy- $X1_n$-$X2_m$ (a) Cu-Cy-Cl_7-F_1, (b) Cu-Cy-Cl_4-F_4 and (c) Cu-Cy-Cl_1-F_7.

Table B.5. The volume and energy of Cu-Cy-Cl$_n$-Br$_m$ structures GGA calculations to calculate the bulk modulus

Cu-Cy-Cl$_7$-Br$_1$		Cu-Cy-Cl$_4$-Br$_4$		Cu-Cy-Cl$_1$-Br$_7$	
V (Å^3)	E (eV)	V (Å^3)	E (eV)	V (Å^3)	E (eV)
1743.53	-977.0859074	1763.03	-975.4821108	1783.77	-973.9381887
1767.9	-977.5412	1787.58	-975.9310338	1808.5	-974.3681407
1792.46	-977.9101244	1812.33	-976.2509513	1833.43	-974.7154579
1817.22	-978.1853645	1837.28	-976.5282763	1858.56	-975.0147431
1842.18	-978.3486855	1862.42	-976.7475572	1883.89	-975.2464186
1867.34	-978.4917228	1887.77	-976.8936128	1909.42	-975.3961364
1892.7	-978.5689802	1913.32	-976.9573629	1935.15	-975.4206707
1918.27	-978.5453986	1939.08	-976.9113686	1961.08	-975.3859147
1944.03	-978.3995764	1991.19	-976.6870219	1987.22	-975.3349143
1970	-978.2587821	2044.12	-976.2659998	2013.57	-975.188564
1996.17	-978.068954	2070.9	-975.9924887	2040.12	-975.0035673

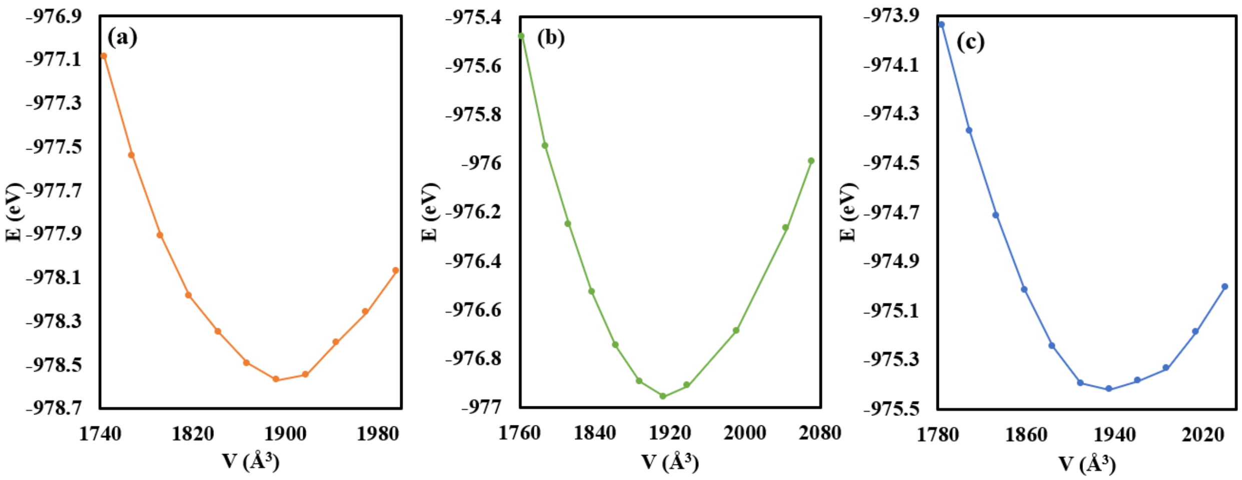

Figure B.11. E-V plots of Cu-Cy- $X1_n$-$X2_m$ (a) Cu-Cy-Cl_7-Br_1, (b) Cu-Cy-Cl_4-Br_4 and (c) Cu-Cy-Cl_1-Br_7.

Table B.6. The volume and energy of Cu-Cy-Cl_n-I_m structures GGA calculations to calculate the bulk modulus

Cu-Cy-Cl_7-I_1		Cu-Cy-Cl_4-I_4		Cu-Cy-Cl_1-I_7	
V (Å^3)	E (eV)	V (Å^3)	E (eV)	V (Å^3)	E (eV)
1752.9	-976.362745	1805.01	-972.4702981	1872.82	-969.2464949
1777.34	-976.8163405	1829.96	-972.9409321	1892.84	-969.6282949
1801.98	-977.1822445	1855.12	-973.3385812	1924.24	-970.0484077
1826.81	-977.4465351	1880.48	-973.6431309	1944.55	-970.2996396
1851.85	-977.6406696	1906.04	-973.8797555	1976.48	-970.5517921
1877.09	-977.7819734	1931.81	-974.0226624	1997.08	-970.650206
1902.53	-977.8400372	1957.77	-974.1040747	2023.65	-970.7444267
1928.17	-977.82144	1983.94	-974.0913518	2050.42	-970.7639347
1954.01	-977.7382116	2010.32	-974.0349454	2077.41	-970.7069008
1980.05	-977.6215906	2036.9	-973.9399172	2104.6	-970.6150137
2006.3	-977.4349729	2063.69	-973.7879087	2132	-970.4709657

Appendix C

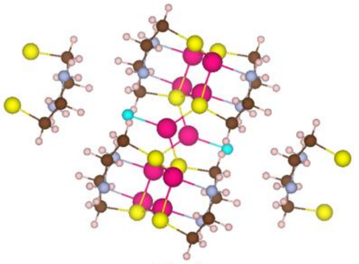
(1a)

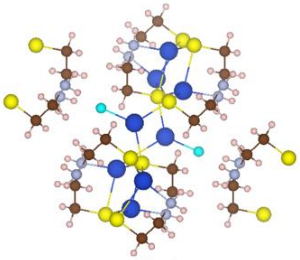
(2a)

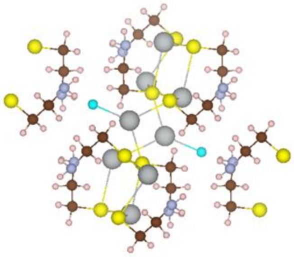
(3a)

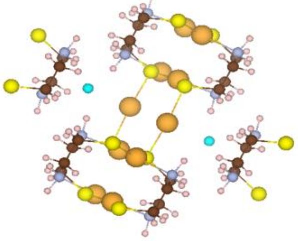
(4a)

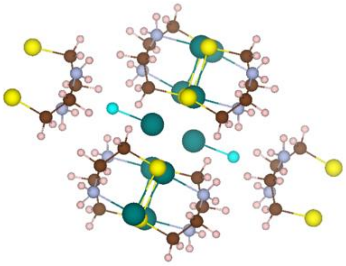
(5a)

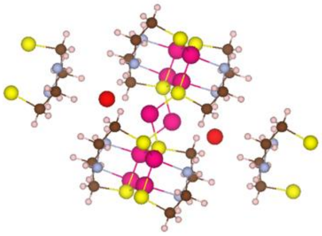
(1b)

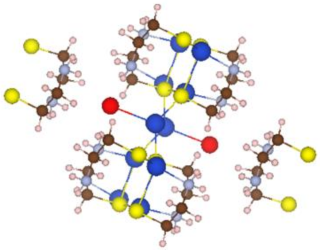
(2b)

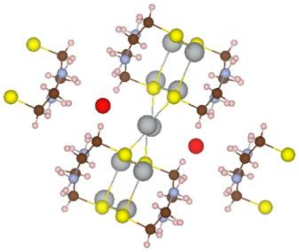
(3b)

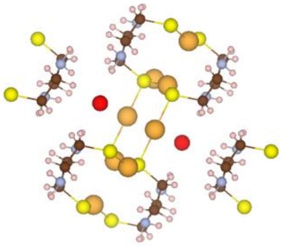
(4b)

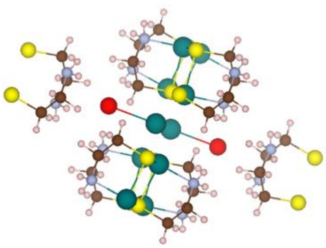
(5b)

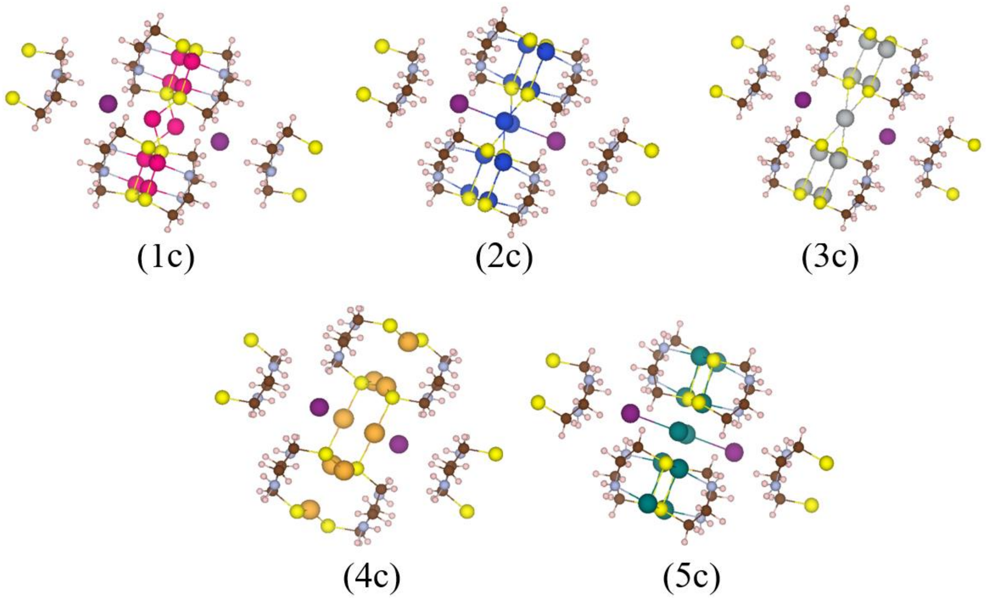

(1c) (2c) (3c)

(4c) (5c)

Figure C.1. GGA relaxed structures of M-Cy-X (1a) Co-Cy-F, (2a) Cu-Cy-F, (3a) Ag-Cy-F, (4a) Au-Cy-F, (5a) Zn-Cy-F, (1b) Co-Cy-Br, (2b) Cu-Cy-Br, (3b) Ag-Cy-Br, (4b) Au-Cy-Br, (5b) Zn-Cy-Br, (1c) Co-Cy-I, (2c) Cu-Cy-I, (3c) Ag-Cy-I, (4c) Au-Cy-I, (5c) Zn-Cy-I. F atoms are represented in light turquoise, Br in red, I in purple, S in yellow, Co in dark pink , Cu in blue, Ag in silver , Au in gold , Zn in dark green , C in brown, N in light blue and H in light pink.

Table C.1. Lattice parameters and angles of M-Cy-F (M= Co, Cu, Ag, Au, and Zn) of singlet and triplet states calculated by GGA functional

Structure	a (A^{o})	b (A^{o})	c (A^{o})	α (^{o})	β (^{o})	γ (^{o})
Co-Cy-F /singlet	9.13740	9.13740	7.80520	92.6942	92.6942	141.8084
Co-Cy-F /triplet	9.12650	9.12650	7.90338	92.2253	92.2253	141.4935
Cu-Cy-F /singlet	8.68834	8.68834	7.71364	95.6501	95.6501	130.8287
Cu-Cy-F /triplet	8.80503	8.80503	7.73776	95.6566	95.6566	132.2702
Ag-Cy-F /singlet	8.97142	8.97142	8.47034	96.2865	96.2865	131.0205
Ag-Cy-F /triplet	9.01366	9.01366	8.85883	96.4904	96.4904	134.4184
Au-Cy-F /singlet	9.23529	9.23529	8.44898	103.5180	103.5180	122.1685
Au-Cy-F /triplet	9.07762	9.07762	8.68721	104.4401	104.4401	120.1797
Zn-Cy-F /singlet	8.24337	8.24337	11.57860	84.5513	84.5513	134.9277
Zn-Cy-F /triplet	7.76139	7.76139	13.28566	84.0069	84.0069	133.8381

Table C.2. Lattice parameters and angles of M-Cy-Br (M= Co, Cu, Ag, Au, and Zn) of singlet and triplet states calculated by GGA functional

Structure	a (A^{o})	b (A^{o})	c (A^{o})	α (^{o})	β (^{o})	γ (^{o})
Co-Cy-Br /singlet	9.18344	9.18344	8.18915	92.5382	92.5382	140.8959
Co-Cy-Br /triplet	9.19608	9.19608	8.21175	92.3908	92.3908	140.6731
Cu-Cy-Br /singlet	9.39036	9.39036	7.66397	95.7979	95.7979	132.1817
Cu-Cy-Br /triplet	9.54132	9.54132	7.61127	95.9129	95.9129	32.7854
Ag-Cy-Br /singlet	9.38998	9.38998	9.08730	93.2015	93.2015	132.7973
Ag-Cy-Br /triplet	9.39642	9.39642	9.50890	92.3030	92.3030	136.0631
Au-Cy-Br /singlet	9.24270	9.24270	8.47285	97.4274	97.4274	126.6052
Au-Cy-Br /triplet	9.12777	9.12777	8.99929	95.9898	95.9898	129.3022
Zn-Cy-Br /singlet	8.85389	8.85389	11.52496	86.3464	86.3464	138.3425
Zn-Cy-Br /triplet	8.84125	8.84125	12.14765	85.4049	85.4049	138.9238

Table C.3. Lattice parameters and angles of M-Cy-I (M= Co, Cu, Ag, Au, and Zn) of singlet and triplet states calculated by GGA functional

Structure	a (A^o)	b (A^o)	c (A^o)	α (^{o})	β (^{o})	γ (^{o})
Co-Cy-I /singlet	9.54247	9.54247	8.3006	92.4642	92.4642	142.1835
Co-Cy-I /triplet	9.56278	9.56278	8.31850	92.3598	92.3598	142.0189
Cu-Cy-I /singlet	9.71946	9.71946	7.63439	96.0996	96.0996	132.6065
Cu-Cy-I /triplet	9.71946	9.71946	7.63439	96.0996	96.0996	132.6065
Ag-Cy-I /singlet	9.61441	9.61441	9.05489	93.2620	93.2620	132.5461
Ag-Cy-I /triplet	9.58844	9.58844	9.65090	92.0137	92.0137	136.6362
Au-Cy-I /singlet	9.40436	9.40436	8.38420	97.3382	97.3382	126.5208
Au-Cy-I /triplet	9.31767	9.31767	8.63336	95.8143	95.8143	128.1918
Zn-Cy-I /singlet	9.05346	9.05346	11.58149	87.2328	87.2328	139.4856
Zn-Cy-I /triplet	9.03673	9.03673	11.78895	86.7010	86.7010	139.0976

Table C.4. Bader charges of H and C atoms in M-Cy-Cl (M= Co, Cu, Ag, Au, and Zn) in their ground state using GGA functional

Singlet	Co-Cy-Cl	Cu-Cy-Cl	Ag-Cy-Cl	Au-Cy-Cl	Zn-Cy-Cl
H	0.449817	0.435128	0.429093	0.448782	0.414134
H	0.449817	0.435128	0.429092	0.448782	0.414134
H	0.449817	0.435128	0.429098	0.448782	0.414134
H	0.449817	0.435128	0.429099	0.44878	0.414134
H	0.412621	0.428606	0.412654	0.450217	0.403545
H	0.412622	0.428606	0.412654	0.450218	0.403544
H	0.41253	0.428606	0.412651	0.450216	0.403544
H	0.41253	0.428606	0.412654	0.450218	0.403544
H	0.023571	0.039307	0.059263	0.090487	0.068684
H	0.023906	0.039307	0.059263	0.090487	0.068684
H	0.023906	0.039308	0.059264	0.090487	0.068684
H	0.023571	0.039308	0.059263	0.090488	0.068684
H	0.08232	0.111719	0.082634	0.096177	0.111277
H	0.08232	0.111719	0.082642	0.096178	0.111291
H	0.082319	0.111719	0.082642	0.096178	0.111291
H	0.08232	0.111719	0.082635	0.096177	0.111277
H	0.040781	0.049658	0.05493	0.073575	0.064555
H	0.040781	0.049658	0.054945	0.073575	0.064555
H	0.041113	0.050172	0.055682	0.072986	0.06605

H	0.041113	0.050172	0.055666	0.072985	0.06605
H	0.06235	0.014804	0.037997	0.024493	0.029993
H	0.062449	0.015095	0.038002	0.024491	0.029992
H	0.062459	0.015095	0.037991	0.024493	0.029981
H	0.06236	0.014804	0.037983	0.024492	0.029981
C	-0.1159	-0.10727	-0.12909	-0.12282	-0.1518
C	-0.11588	-0.10727	-0.12909	-0.12279	-0.15179
C	-0.11589	-0.10745	-0.12909	-0.12279	-0.15179
C	-0.1159	-0.10745	-0.12909	-0.12282	-0.1518
C	0.245653	0.26937	0.313115	0.274525	0.260036
C	0.245653	0.26937	0.313116	0.274524	0.260036
C	0.245653	0.269371	0.313095	0.274526	0.260036
C	0.245653	0.269371	0.31309	0.274527	0.260035

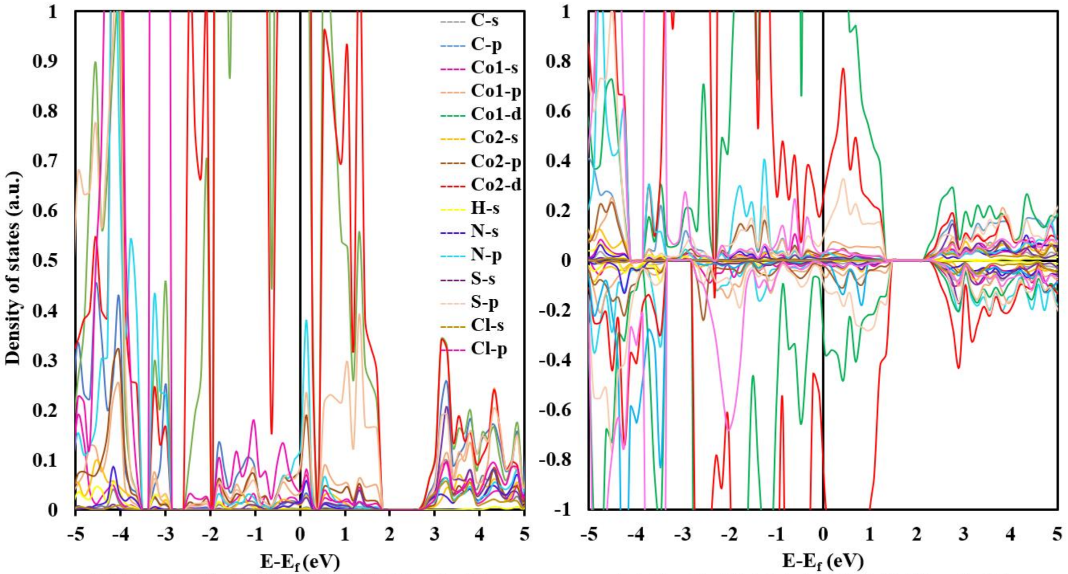

(a) Co-Cy-Cl singlet DFT+ U (U = 4 eV) (b) Co-Cy-Cl triplet DFT+ U (U = 4 eV)

Figure C.2. Density of states (partial DOS) (a) singlet state and (b) triplet state of Co-Cy-Cl calculated with DFT+ U (U = 4 eV). The top of the valence band is scaled to 0 eV, which is called Fermi level. Spin-polarized calculations were performed, but for singlet state only spin-up DOS is plotted. For triplet state, the spin-up channel is presented by positive density of states and spin-down channels by the negative density of states.

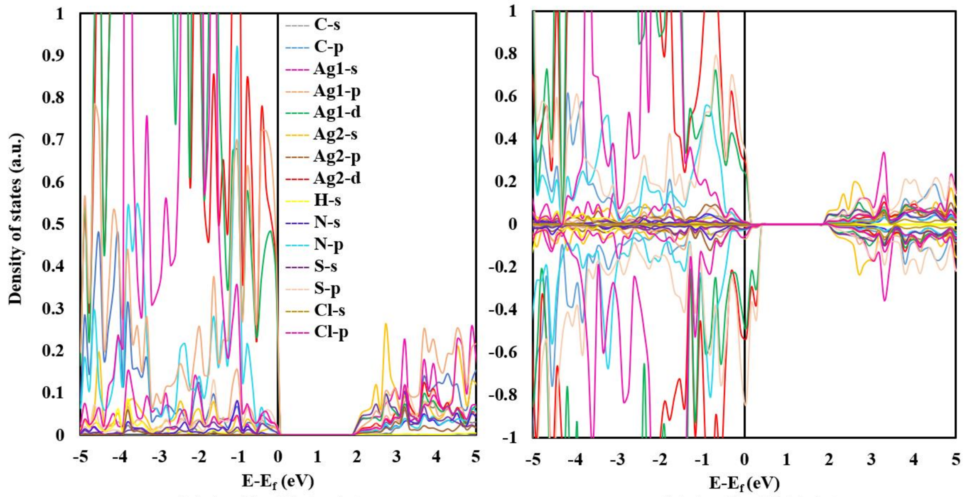

(a) Ag-Cy-Cl singlet (b) Ag-Cy-Cl triplet

Figure C.3. Density of states (partial DOS) (a) singlet state and (b) triplet state of Ag-Cy-Cl calculated with GGA functional.

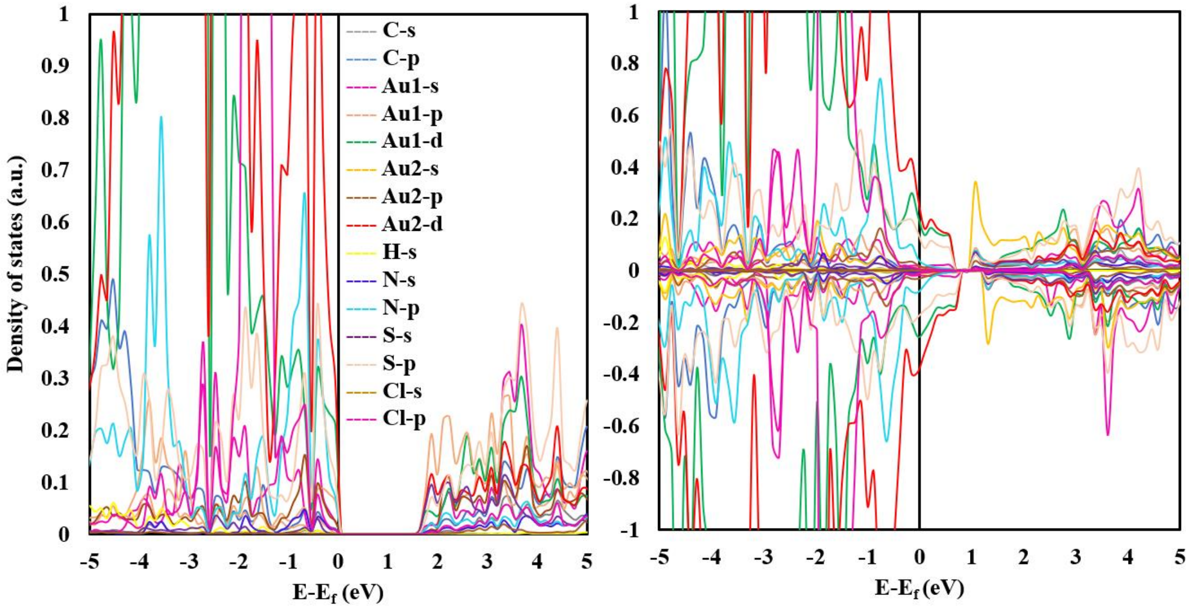

(a) Au-Cy-Cl singlet (b) Au-Cy-Cl triplet

Figure C.4. Density of states (partial DOS) (a) singlet state and (b) triplet state of Au-Cy-Cl calculated with GGA functional.

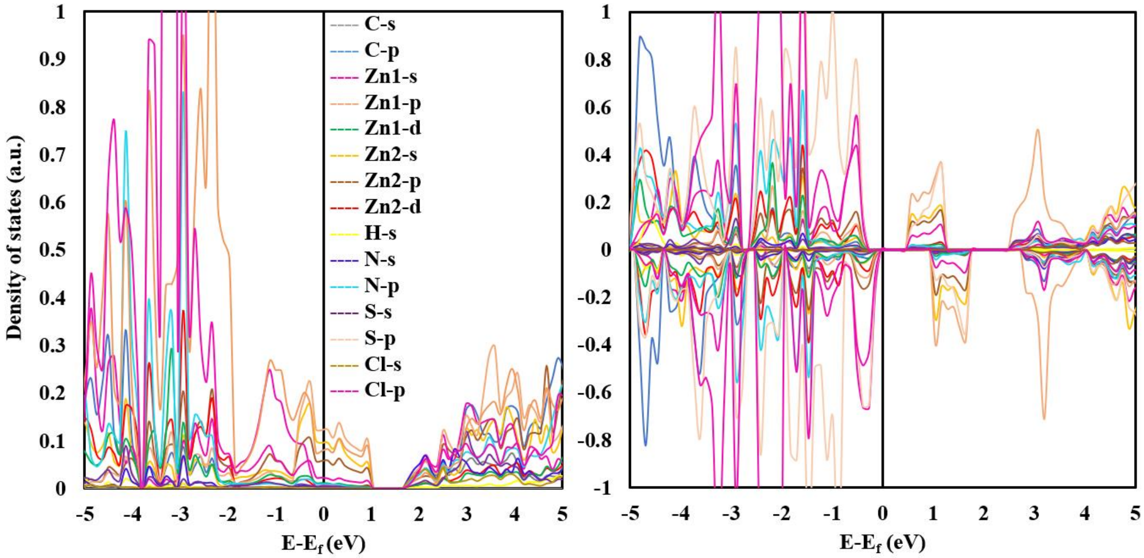

(a) Zn-Cy-Cl singlet (b) Zn-Cy-Cl triplet

Figure C.5. Density of states (partial DOS) (a) singlet state and (b) triplet state of Zn-Cy-Cl calculated with GGA functional.

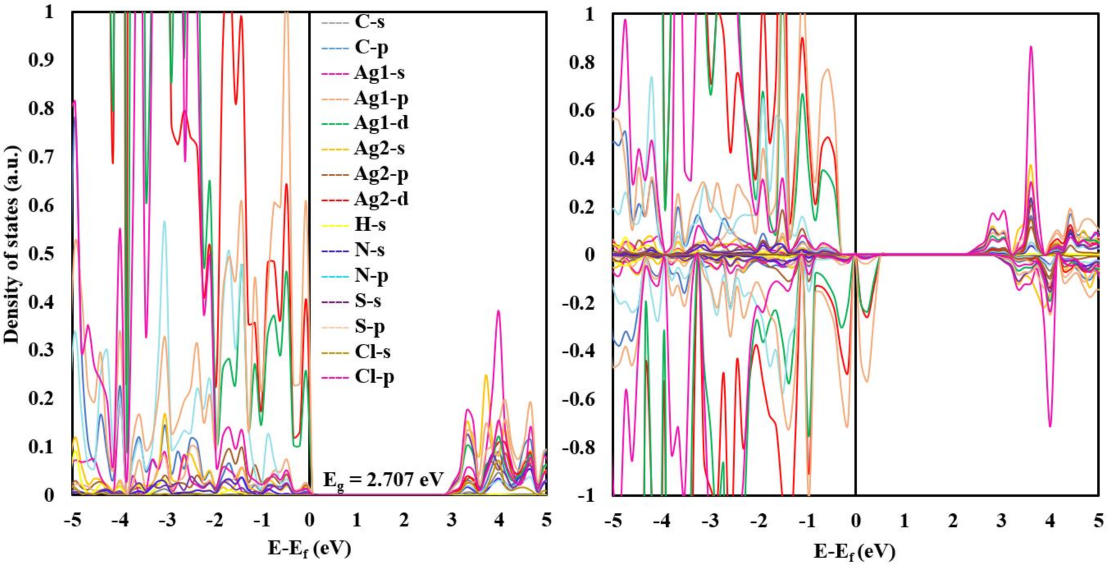

(a) Ag-Cy-Cl singlet

(b) Ag-Cy-Cl triplet

Figure C.6. Density of states (partial DOS) (a) singlet state and (b) triplet state of Ag-Cy-Cl calculated with hybrid functional (HSE06).

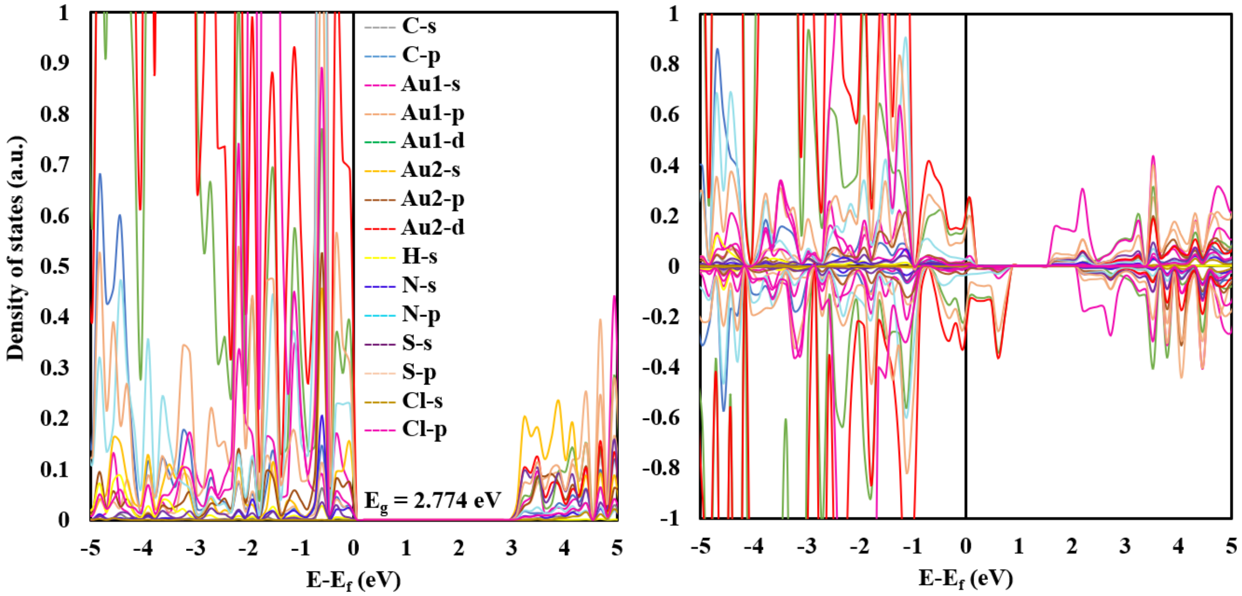

(a) Au-Cy-Cl singlet

(b) Au-Cy-Cl triplet

Figure C.7. Density of states (partial DOS) (a) singlet state and (b) triplet state of Au-Cy-Cl calculated with hybrid functional (HSE06).

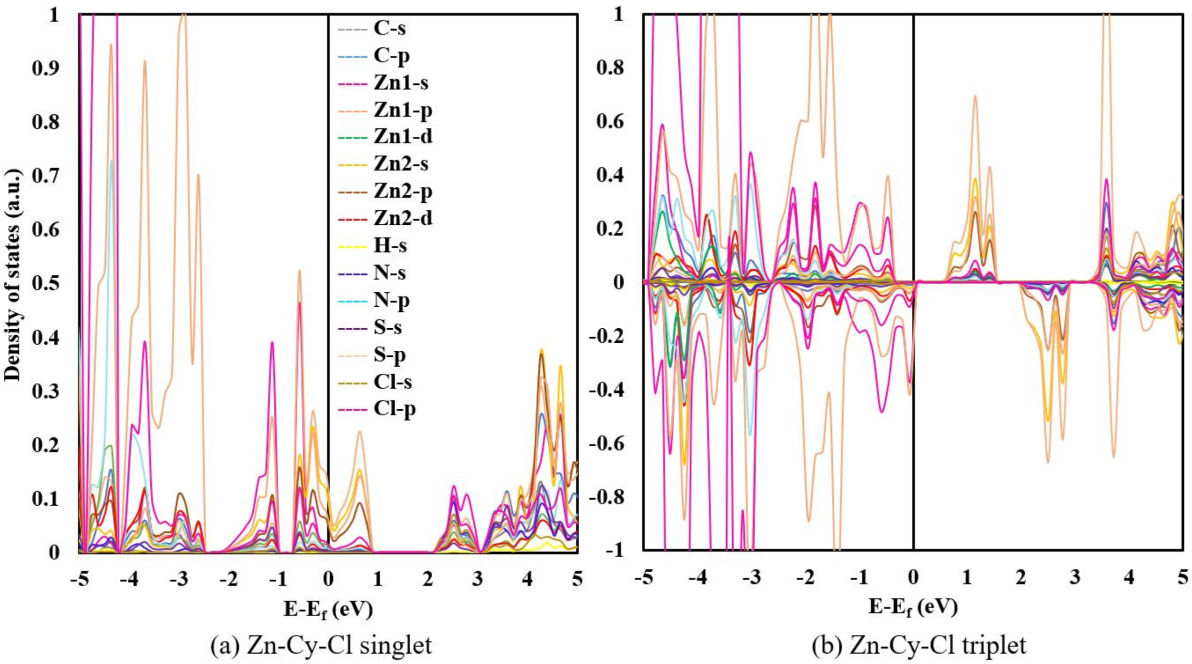

(a) Zn-Cy-Cl singlet (b) Zn-Cy-Cl triplet

Figure C.8. Density of states (partial DOS) (a) singlet state and (b) triplet state of Zn-Cy-Cl calculated with hybrid functional (HSE06).

References

[1] I. Beletskaya, V. S. Tyurin, A. Y. Tsivadze, R. Guilard, and C. Stern, "Supramolecular Chemistry of Metalloporphyrins," *Chemical Reviews,* vol. 109, no. 5, pp. 1659-1713, May 2009, doi: 10.1021/cr800247a.

[2] T. Buttner *et al.*, "A stable aminyl radical metal complex," *Science,* vol. 307, no. 5707, pp. 235-238, Jan 2005, doi: 10.1126/science.1106070.

[3] J. Chin, S. S. Lee, K. J. Lee, S. Park, and D. H. Kim, "A metal complex that binds alpha-amino acids with high and predictable stereospecificity," *Nature,* vol. 401, no. 6750, pp. 254-257, Sep 1999, doi: 10.1038/45751.

[4] R. Mason, "ACTIVATION OF SMALL MOLECULES BY TRANSITION METAL IONS AND THEIR COMPLEXES," *Nature,* vol. 217, no. 5128, pp. 543-&, 1968, doi: 10.1038/217543a0.

[5] R. N. Patel, K. K. Shukla, A. Singh, M. Choudhary, U. K. Chauhan, and S. Dwivedi, "Copper(II) complexes as superoxide dismutase mimics: Synthesis, characterization, crystal structure and bioactivity of copper(II) complexes," *Inorganica Chimica Acta,* vol. 362, no. 14, pp. 4891-4898, Nov 2009, doi: 10.1016/j.ica.2009.07.037.

[6] S. Sen Gupta *et al.*, "Rapid total destruction of chlorophenols by activated hydrogen peroxide," *Science,* vol. 296, no. 5566, pp. 326-328, Apr 2002, doi: 10.1126/science.1069297.

[7] B. Bruni, M. Ferraroni, P. Oriolo, and G. Speroni, "A biologically active gold complex: Trichloro (2-pyridyl)methanol-N gold(III)," *Acta Crystallographica Section C-Crystal Structure Communications,* vol. 52, pp. 1423-1424, Jun 1996, doi: 10.1107/s0108270195008067.

[8] V. Fernandez-Moreira, F. L. Thorp-Greenwood, and M. P. Coogan, "Application of d(6) transition metal complexes in fluorescence cell imaging," *Chemical Communications,* vol. 46, no. 2, pp. 186-202, 2010, doi: 10.1039/b917757d.

[9] K. Kalyanasundaram and M. Gratzel, "Applications of functionalized transition metal complexes in photonic and optoelectronic devices," *Coordination Chemistry Reviews,* vol. 177, pp. 347-414, Oct 1998, doi: 10.1016/s0010-8545(98)00189-1.

[10] D. L. Ma, H. Z. He, K. H. Leung, D. S. H. Chan, and C. H. Leung, "Bioactive Luminescent Transition-Metal Complexes for Biomedical Applications," *Angewandte Chemie-International Edition,* vol. 52, no. 30, pp. 7666-7682, Jul 2013, doi: 10.1002/anie.201208414.

[11] R. W. Y. Sun, D. L. Ma, E. L. M. Wong, and C. M. Che, "Some uses of transition metal complexes as anti-cancer and anti-HIV agents," *Dalton Transactions,* no. 43, pp. 4884-4892, 2007, doi: 10.1039/b705079h.

[12] V. W. W. Yam and K. M. C. Wong, "Luminescent metal complexes of d(6), d(8) and d(10) transition metal centres," *Chemical Communications,* vol. 47, no. 42, pp. 11579-11592, 2011, doi: 10.1039/c1cc13767k.

[13] J. G. Thoene, R. G. Oshima, J. C. Crawhall, D. L. Olson, and J. A. Schneider, "CYSTINOSIS - INTRACELLULAR CYSTINE DEPLETION BY AMINOTHIOLS INVITRO AND INVIVO," *Journal of Clinical Investigation,* vol. 58, no. 1, pp. 180-189, 1976, doi: 10.1172/jci108448.

[14] D. C. Jicha and D. H. Busch, "COMPLEXES DERIVED FROM STRONG FIELD LIGANDS .14. HETEROMETALLIC TRINUCLEAR COMPLEXES OF BETA-MERCAPTOETHYLAMINE," *Inorganic Chemistry,* vol. 1, no. 4, pp. 878-&, 1962, doi: 10.1021/ic50004a035.

[15] C. H. Wei and L. F. Dahl, "STRUCTURAL CHARACTERIZATION OF CRYSTALLINE TETRAKIS(2-AMINOETHANETHIOL)TRINICKEL(II) CHLORIDE, NI NI(NH2CH2CH2S)2!2!CL2 - A NEW BASIC TRINUCLEAR METAL SYSTEM CONTAINING NICKEL(II)-NICKEL(II) INTERACTIONS," *Inorganic Chemistry,* vol. 9, no. 8, pp. 1878-&, 1970, doi: 10.1021/ic50090a018.

[16] M. Mori, J. A. Weil, and J. K. Kinnaird, "PREPARATION AND ELECTRON PARAMAGNETIC RESONANCE SPECTROSCOPY OF DICOBALT PEROXO ANIONS," *Journal of Physical Chemistry,* vol. 71, no. 1, pp. 103-&, 1967, doi: 10.1021/j100860a014.

[17] D. Habibi, E. Ghaemi, and D. Nematollahi, "Synthesis of some novel silver-cysteamine complexes," *Molecules,* vol. 5, no. 12, pp. 1194-1200, Dec 2000, doi: 10.3390/51201194.

[18] M. S. Bharara, C. H. Kim, S. Parkin, and D. A. Atwood, "Synthesis and X-ray crystal structures of dinuclear hydrogen-bonded cadmium and lead 2-aminoethanethiolates," *Polyhedron,* vol. 24, no. 8, pp. 865-871, Jun 2005, doi: 10.1016/j.poly.2005.01.019.

[19] M. S. Bharara, S. Parkin, and D. A. Atwood, "Mercury(II) 2-aminoethanethiolate clusters: Intramolecular transformations and mechanisms," *Inorganic Chemistry,* vol. 45, no. 18, pp. 7261-7268, Sep 2006, doi: 10.1021/ic060863e.

[20] A. Kudelski and W. Hill, "Roman study on the structure of cysteamine monolayers on silver," *Langmuir,* vol. 15, no. 9, pp. 3162-3168, Apr 1999, doi: 10.1021/la9811463.

[21] M. Wirde, U. Gelius, and L. Nyholm, "Self-assembled monolayers of cystamine and cysteamine on gold studied by XPS and voltammetry," *Langmuir,* vol. 15, no. 19, pp. 6370-6378, Sep 1999, doi: 10.1021/la9903245.

[22] H. Z. Yu, J. W. Zhao, Y. Q. Wang, S. M. Cai, and Z. F. Liu, "Fabricating an azobenzene self-assembled monolayer via step-by-step surface modification of a cysteamine monolayer on gold," *Journal of Electroanalytical Chemistry,* vol. 438, no. 1-2, pp. 221-224, Nov 1997, doi: 10.1016/s0022-0728(97)00055-7.

[23] E. Y. Kats and A. A. Solovev, "CHEMICAL MODIFICATION OF PLATINUM AND GOLD ELECTRODES WITH NAPHTHOQUINONES VIA AMINES CONTAINING A SULFHYDRYL OR DISULFIDE GROUP," *Soviet Electrochemistry,* vol. 26, no. 10, pp. 1163-1168, Oct 1990. [Online]. Available: <Go to ISI>://WOS:A1990FN21800015.

[24] I. Willner and A. Riklin, "ELECTRICAL COMMUNICATION BETWEEN ELECTRODES AND NAD(P)(+)-DEPENDENT ENZYMES USING PYRROLOQUINOLINEQUINONE-ENZYME ELECTRODES IN A SELF-ASSEMBLED MONOLAYER CONFIGURATION - DESIGN OF A NEW GLASS OF AMPEROMETRIC BIOSENSORS," *Analytical Chemistry,* vol. 66, no. 9, pp. 1535-1539, May 1994, doi: 10.1021/ac00081a028.

[25] E. Katz, T. Lotzbeyer, D. D. Schlereth, W. Schuhmann, and H. L. Schmidt, "ELECTROCATALYTIC OXIDATION OF REDUCED NICOTINAMIDE COENZYMES AT GOLD AND PLATINUM-ELECTRODE SURFACES MODIFIED WITH A MONOLAYER OF PYRROLOQUINOLINE QUINONE - EFFECT OF CA2+ CATIONS," *Journal of Electroanalytical Chemistry,* vol. 373, no. 1-2, pp. 189-200, Aug 1994, doi: 10.1016/0022-0728(94)03328-5.

[26] E. Katz and H. L. Schmidt, "GOLD ELECTRODE MODIFICATION WITH A MONOLAYER OF 1,4,5,8-NAPHTHALENETETRONE AS A 4-ELECTRON TRANSFER MEDIATOR - ELECTROCHEMICAL REDUCTION OF DIOXYGEN TO WATER," *Journal of Electroanalytical Chemistry,* vol. 368, no. 1-2, pp. 87-94, Apr 1994, doi: 10.1016/0022-0728(93)03039-r.

[27] M. C. Millot, F. Martin, D. Bousquet, B. Sebille, and Y. Levy, "A REACTIVE MACROMOLECULAR MATRIX FOR PROTEIN IMMOBILIZATION ON A GOLD SURFACE - APPLICATION IN SURFACE-PLASMON RESONANCE," *Sensors and Actuators B-Chemical,* vol. 29, no. 1-3, pp. 268-273, Oct 1995, doi: 10.1016/0925-4005(95)01693-7.

[28] G. Brink, L. Schmitt, R. Tampe, and E. Sackmann, "SELF-ASSEMBLY OF COVALENTLY ANCHORED PHOSPHOLIPID SUPPORTED MEMBRANES BY USE OF DODA-SUC-NHS-LIPIDS," *Biochimica Et Biophysica Acta-Biomembranes,* vol. 1196, no. 2, pp. 227-230, Dec 1994, doi: 10.1016/0005-2736(94)00218-5.

[29] F. Mirkhalaf and D. J. Schiffrin, "Surface spectroscopy and electrochemical characterisation of metal dithizonates covalently attached to gold by a self-assembled cysteamine monolayer,"

Journal of the Chemical Society-Faraday Transactions, vol. 94, no. 9, pp. 1321-1327, May 1998, doi: 10.1039/a708625c.

[30] J. Horacek and P. Skladal, "Improved direct piezoelectric biosensors operating in liquid solution for the competitive label-free immunoassay of 2,4-dichlorophenoxyacetic acid," *Analytica Chimica Acta,* vol. 347, no. 1-2, pp. 43-50, Jul 1997, doi: 10.1016/s0003-2670(97)00125-6.

[31] P. Wagner, M. Hegner, H. J. Guntherodt, and G. Semenza, "FORMATION AND IN-SITU MODIFICATION OF MONOLAYERS CHEMISORBED ON ULTRAFLAT TEMPLATE-STRIPPED GOLD SURFACES," *Langmuir,* vol. 11, no. 10, pp. 3867-3875, Oct 1995, doi: 10.1021/la00010a043.

[32] B. Shapiro and L. Eldjarn, "THE MECHANISM FOR THE DEGRADATION OF CYSTAMINE BY IONIZING RADIATION," *Radiation Research,* vol. 3, no. 4, pp. 393-399, 1955, doi: 10.2307/3570165.

[33] B. Shapiro and L. Eldjarn, "THE EFFECTS OF IONIZING RADIATION ON AQUEOUS SOLUTIONS OF CYSTEAMINE AND CYSTAMINE," *Radiation Research,* vol. 3, no. 3, pp. 255-266, 1955, doi: 10.2307/3570327.

[34] R. Charlier, "EFFECTS OF CYSTEAMINE AND CYSTEINE ON CARDIAC OUTPUT AND OXYGEN CONTENT OF VENOUS BLOOD," *Proceedings of the Society for Experimental Biology and Medicine,* vol. 86, no. 2, pp. 290-293, 1954. [Online]. Available: <Go to ISI>://WOS:A1954UH15000025.

[35] A. Lavie-Cambot, M. Cantuel, Y. Leydet, G. Jonusauskas, D. M. Bassani, and N. D. McClenaghan, "Improving the photophysical properties of copper(I) bis(phenanthroline) complexes," *Coordination Chemistry Reviews,* vol. 252, no. 23-24, pp. 2572-2584, Dec 2008, doi: 10.1016/j.ccr.2008.03.013.

[36] N. Armaroli, G. Accorsi, F. Cardinali, and A. Listorti, "Photochemistry and photophysics of coordination compounds: Copper," in *Photochemistry and Photophysics of Coordination Compounds I*, vol. 280, V. Balzani and S. Campagna Eds., (Topics in Current Chemistry, 2007, pp. 69-115.

[37] C. W. Hsu *et al.*, "Systematic Investigation of the Metal-Structure-Photophysics Relationship of Emissive d(10)-Complexes of Group 11 Elements: The Prospect of Application in Organic Light Emitting Devices," *Journal of the American Chemical Society,* vol. 133, no. 31, pp. 12085-12099, Aug 2011, doi: 10.1021/ja2026568.

[38] B. A. Matrana, W. R. Bordelon, and D. G. Davis, "POLAROGRAPHY OF COPPER(II) .1. CYSTEAMINE-CYSTAMINE SYSTEMS," *Analytical Letters,* vol. 4, no. 7, pp. 437-&, 1971. [Online]. Available: <Go to ISI>://WOS:A1971K029100006.

[39] R. V. Parish, Z. Salehi, and R. G. Pritchard, "Five-coordinate sulfur in a polymeric copper(I) thiolate complex," *Angewandte Chemie-International Edition in English,* vol. 36, no. 3, pp. 251-253, Feb 1997, doi: 10.1002/anie.199702511.

[40] Z. Salehi, R. V. Parish, and R. G. Pritchard, "A polymeric cationic copper(I) complex involving a quadruply bridging, zwitterionic thiolate ligand: { $Cu_8Cl_6(SCH_2CH_2NH_3)_{(6)}$ Cl-$_2$}$_{(n)}$," *Journal of the Chemical Society-Dalton Transactions,* no. 22, pp. 4241-4246, Nov 1997, doi: 10.1039/a705217k.

[41] L. Ma, X. J. Zou, and W. Chen, "A New X-Ray Activated Nanoparticle Photosensitizer for Cancer Treatment," *Journal of Biomedical Nanotechnology,* vol. 10, no. 8, pp. 1501-1508, Aug 2014, doi: 10.1166/jbn.2014.1954.

[42] L. Ma *et al.*, "A new Cu-cysteamine complex: structure and optical properties," *Journal of Materials Chemistry C,* vol. 2, no. 21, pp. 4239-4246, 2014, doi: 10.1039/c4tc00114a.

[43] X. D. Ren, X. Y. Hao, H. C. Li, M. R. Ke, B. Y. Zheng, and J. D. Huang, "Progress in the development of nanosensitizers for X-ray-induced photodynamic therapy," *Drug Discovery Today,* vol. 23, no. 10, pp. 1791-1800, Oct 2018, doi: 10.1016/j.drudis.2018.05.029.

[44] B. Sah *et al.*, "Effects of Nanoparticle Size and Radiation Energy on Copper-Cysteamine Nanoparticles for X-ray Induced Photodynamic Therapy," *Nanomaterials,* vol. 10, no. 6, Jun 2020, Art no. 1087, doi: 10.3390/nano10061087.

[45] M. Y. Yao *et al.*, "A New Modality for Cancer Treatment-Nanoparticle Mediated Microwave Induced Photodynamic Therapy," *Journal of Biomedical Nanotechnology,* vol. 12, no. 10, pp. 1835-1851, Oct 2016, doi: 10.1166/jbn.2016.2322.

[46] X. J. Huang *et al.*, "Investigation of copper-cysteamine nanoparticles as a new photosensitizer for anti-hepatocellular carcinoma," *Cancer Biology & Therapy,* vol. 20, no. 6, pp. 812-825, Jun 2019, doi: 10.1080/15384047.2018.1564568.

[47] L. Larue *et al.*, "Using X-rays in photodynamic therapy: an overview," *Photochemical & Photobiological Sciences,* vol. 17, no. 11, pp. 1612-1650, Nov 2018, doi: 10.1039/c8pp00112j.

[48] M. Hayyan, M. A. Hashim, and I. M. AlNashef, "Superoxide Ion: Generation and Chemical Implications," *Chemical Reviews,* vol. 116, no. 5, pp. 3029-3085, Mar 2016, doi: 10.1021/acs.chemrev.5b00407.

[49] M. Alias *et al.*, "Theoretical studies on the energy structures and optical properties of copper cysteamine - a novel sensitizer," *Physical Chemistry Chemical Physics,* vol. 21, no. 37, pp. 21084-21093, Oct 2019, doi: 10.1039/c9cp04392f.

[50] R. Enoki, H. Gamou, M. Kohda, and J. Nitta, "Enhancement of spin-orbit interaction of Cu thin films by oxidation treatment," *Applied Physics Express,* vol. 11, no. 3, Mar 2018, Art no. 033001, doi: 10.7567/apex.11.033001.

[51] C. E. DeSantis *et al.*, "Cancer statistics for African Americans, 2016: Progress and opportunities in reducing racial disparities," *Ca-a Cancer Journal for Clinicians,* vol. 66, no. 4, pp. 290-308, Jul-Aug 2016, doi: 10.3322/caac.21340.

[52] M. F. Atoum and F. Alzoughool, "Reduction in breast cancer susceptibility due to XbaI gene polymorphism of alpha estrogen receptor gene in Jordanians," *Breast Cancer-Targets and Therapy,* vol. 9, pp. 45-49, 2017, doi: 10.2147/bctt.S125652.

[53] M. Bottini *et al.*, "Targeted Nanodrugs for Cancer Therapy: Prospects and Challenges," *Journal of Nanoscience and Nanotechnology,* vol. 14, no. 1, pp. 98-114, Jan 2014, doi: 10.1166/jnn.2014.9010.

[54] A. M. Cherian, S. V. Nair, and V. K. Lakshmanan, "The Role of Nanotechnology in Prostate Cancer Theranostic Applications," *Journal of Nanoscience and Nanotechnology,* vol. 14, no. 1, pp. 841-852, Jan 2014, doi: 10.1166/jnn.2014.9052.

[55] S. Elingarami, M. Liu, J. Fan, and N. Y. He, "Applications of Nanotechnology in Gastric Cancer: Detection and Prevention by Nutrition," *Journal of Nanoscience and Nanotechnology,* vol. 14, no. 1, pp. 932-945, Jan 2014, doi: 10.1166/jnn.2014.9008.

[56] J. F. Liao, T. T. Qi, B. Y. Chu, J. R. Peng, F. Luo, and Z. Y. Qian, "Multifunctional Nanostructured Materials for Multimodal Cancer Imaging and Therapy," *Journal of Nanoscience and Nanotechnology,* vol. 14, no. 1, pp. 175-189, Jan 2014, doi: 10.1166/jnn.2014.9049.

[57] M. Lin, J. X. Huang, and M. Sha, "Recent Advances in Nanosized Mn-Zn Ferrite Magnetic Fluid Hyperthermia for Cancer Treatment," *Journal of Nanoscience and Nanotechnology,* vol. 14, no. 1, pp. 792-802, Jan 2014, doi: 10.1166/jnn.2014.9135.

[58] A. P. Pandey, N. M. Girase, M. D. Patil, P. O. Patil, D. A. Patil, and P. K. Deshmukh, "Nanoarchitectonics in Cancer Therapy and Imaging Diagnosis," *Journal of Nanoscience and Nanotechnology,* vol. 14, no. 1, pp. 828-840, Jan 2014, doi: 10.1166/jnn.2014.9014.

[59] H. I. Pass, "PHOTODYNAMIC THERAPY IN ONCOLOGY - MECHANISMS AND CLINICAL USE," *Jnci-Journal of the National Cancer Institute,* vol. 85, no. 6, pp. 443-456, Mar 1993, doi: 10.1093/jnci/85.6.443.

[60] Y. Saadeh, T. Leung, A. Vyas, L. S. Chaturvedi, O. Perumal, and D. Vyas, "Applications of Nanomedicine in Breast Cancer Detection, Imaging, and Therapy," *Journal of Nanoscience and Nanotechnology,* vol. 14, no. 1, pp. 913-923, Jan 2014, doi: 10.1166/jnn.2014.8755.

[61] R. Singh and H. S. Nalwa, "Medical Applications of Nanoparticles in Biological Imaging, Cell Labeling, Antimicrobial Agents, and Anticancer Nanodrugs," *Journal of Biomedical Nanotechnology,* vol. 7, no. 4, pp. 489-503, Aug 2011, doi: 10.1166/jbn.2011.1324.

[62] M. B. Vrouenraets, G. W. M. Visser, G. B. Snow, and G. van Dongen, "Basic principles, applications in oncology and improved selectivity of photodynamic therapy," *Anticancer Research,* vol. 23, no. 1B, pp. 505-522, Jan-Feb 2003. [Online]. Available: <Go to ISI>://WOS:000181669100001.

[63] J. Fang, T. Seki, and H. Maeda, "Therapeutic strategies by modulating oxygen stress in cancer and inflammation," *Advanced Drug Delivery Reviews,* vol. 61, no. 4, pp. 290-302, Apr 2009, doi: 10.1016/j.addr.2009.02.005.

[64] P. Avci, S. S. Erdem, and M. R. Hamblin, "Photodynamic Therapy: One Step Ahead with Self-Assembled Nanoparticles," *Journal of Biomedical Nanotechnology,* vol. 10, no. 9, pp. 1937-1952, Sep 2014, doi: 10.1166/jbn.2014.1953.

[65] L. W. Lin *et al.*, "Active Targeting of Nano-Photosensitizer Delivery Systems for Photodynamic Therapy of Cancer Stem Cells," *Journal of Biomedical Nanotechnology,* vol. 11, no. 4, pp. 531-554, Apr 2015, doi: 10.1166/jbn.2015.2090.

[66] A. Feofanov *et al.*, "Near-infrared photosensitizer based on a cycloimide derivative of chlorin p6: 13,15-N-(3 '-hydroxypropyl)cycloimide chlorin p6," *Photochemistry and Photobiology,* vol. 75, no. 6, pp. 633-643, Jun 2002, doi: 10.1562/0031-8655(2002)075<0633:Nipboa>2.0.Co;2.

[67] J. P. Rovers, M. L. de Jode, and M. F. Grahn, "Significantly increased lesion size by using the near-infrared photosensitizer 5,10,15,20-tetrakis (m-hydroxyphenyl) bacteriochlorin in interstitial photodynamic therapy of normal rat liver tissue," *Lasers in Surgery and Medicine,* vol. 27, no. 3, pp. 235-240, 2000, doi: 10.1002/1096-9101(2000)27:3<235::Aid-lsm5>3.3.Co;2-k.

[68] J. P. Rovers, M. L. de Jode, H. Rezzoug, and M. F. Grahn, "In vivo photodynamic characteristics of the near-infrared photosensitizer 5,10,15,20-tetrakis(M-hydroxyphenyl) bacteriochlorin," *Photochemistry and Photobiology,* vol. 72, no. 3, pp. 358-364, Sep 2000, doi: 10.1562/0031-8655(2000)072<0358:Ivpcot>2.0.Co;2.

[69] G. Alsayyed, J. C. Doliveira, and P. Pichat, "SEMICONDUCTOR-SENSITIZED PHOTODEGRADATION OF 4-CHLOROPHENOL IN WATER," *Journal of Photochemistry and Photobiology a-Chemistry,* vol. 58, no. 1, pp. 99-114, Apr 1991, doi: 10.1016/1010-6030(91)87101-z.

[70] H. Weller, "Optical properties of quantized semiconductor particles," *Philosophical Transactions of the Royal Society a-Mathematical Physical and Engineering Sciences,* vol. 354, no. 1708, pp. 757-766, Mar 1996, doi: 10.1098/rsta.1996.0029.

[71] P. Wang *et al.*, "Nanosonosensitization by Using Copper-Cysteamine Nanoparticles Augmented Sonodynamic Cancer Treatment," *Particle & Particle Systems Characterization,* vol. 35, no. 4, Apr 2018, Art no. 1700378, doi: 10.1002/ppsc.201700378.

[72] A. Jemal, F. Bray, M. M. Center, J. Ferlay, E. Ward, and D. Forman, "Global Cancer Statistics," *Ca-a Cancer Journal for Clinicians,* vol. 61, no. 2, pp. 69-90, Mar-Apr 2011, doi: 10.3322/caac.20107.

[73] Z. Liu *et al.*, "Investigation of Copper Cysteamine Nanoparticles as a New Type of Radiosensitiers for Colorectal Carcinoma Treatment," *Scientific Reports,* vol. 7, Aug 2017, Art no. 9290, doi: 10.1038/s41598-017-09375-y.

[74] X. Chen *et al.*, "Study of copper-cysteamine based X-ray induced photodynamic therapy and its effects on cancer cell proliferation and migration in a clinical mimic setting," *Bioactive Materials,* vol. 7, pp. 504-514, 2022.

[75] Q. Zhang *et al.*, "Use of copper-cysteamine nanoparticles to simultaneously enable radiotherapy, oxidative therapy and immunotherapy for melanoma treatment," *Signal Transduction and Targeted Therapy,* vol. 5, no. 1, May 2020, Art no. 58, doi: 10.1038/s41392-020-0156-4.

[76] L. A. Torre, F. Bray, R. L. Siegel, J. Ferlay, J. Lortet-Tieulent, and A. Jemal, "Global Cancer Statistics, 2012," *Ca-a Cancer Journal for Clinicians,* vol. 65, no. 2, pp. 87-108, Mar-Apr 2015, doi: 10.3322/caac.21262.

[77] H. B. El-Serag, "Epidemiology of Viral Hepatitis and Hepatocellular Carcinoma," *Gastroenterology,* vol. 142, no. 6, pp. 1264-+, May 2012, doi: 10.1053/j.gastro.2011.12.061.

[78] S. Shrestha *et al.*, "X-ray induced photodynamic therapy with copper-cysteamine nanoparticles in mice tumors," *Proceedings of the National Academy of Sciences of the United States of America,* vol. 116, no. 34, pp. 16823-16828, Aug 2019, doi: 10.1073/pnas.1900502116.

[79] L. Chudal *et al.*, "Copper-Cysteamine Nanoparticles as a Heterogeneous Fenton-Like Catalyst for Highly Selective Cancer Treatment," *Acs Applied Bio Materials,* vol. 3, no. 3, pp. 1804-1814, Mar 2020, doi: 10.1021/acsabm.0c00098.

[80] Y. Chang *et al.*, "Combination of Disulfiram and Copper-Cysteamine Nanoparticles for an Enhanced Antitumor Effect on Esophageal Cancer," *Acs Applied Bio Materials,* vol. 3, no. 10, pp. 7147-7157, Oct 2020, doi: 10.1021/acsabm.0c00949.

[81] L. Y. Huang *et al.*, "Exploration of Copper-Cysteamine Nanoparticles as a New Type of Agents for Antimicrobial Photodynamic Inactivation," *Journal of Biomedical Nanotechnology,* vol. 15, no. 10, pp. 2142-2148, Oct 2019, doi: 10.1166/jbn.2019.2829.

[82] X. M. Zhen *et al.*, "A powerful combination of copper-cysteamine nanoparticles with potassium iodide for bacterial destruction," *Materials Science & Engineering C-Materials for Biological Applications,* vol. 110, May 2020, Art no. 110659, doi: 10.1016/j.msec.2020.110659.

[83] H. Y. Guo *et al.*, "A Non-rare-Earth Ions Self-Activated White Emitting Phosphor under Single Excitation," *Advanced Functional Materials,* vol. 25, no. 44, pp. 6833-6838, Nov 2015, doi: 10.1002/adfm.201502641.

[84] Z. Z. Huang *et al.*, "The exploration of novel fluorescent copper-cysteamine nanosheets for sequential detection of Fe(3+)and dopamine and fabrication of molecular logic circuits," *Journal of Materials Chemistry C,* vol. 8, no. 37, pp. 12935-12942, Oct 2020, doi: 10.1039/d0tc02843f.

[85] J. Jeong, J. Y. Kim, and J. Yoon, "The role of reactive oxygen species in the electrochemical inactivation of microorganisms," *Environmental Science & Technology,* vol. 40, no. 19, pp. 6117-6122, Oct 2006, doi: 10.1021/es0604313.

[86] F. Vatansever *et al.*, "Antimicrobial strategies centered around reactive oxygen species - bactericidal antibiotics, photodynamic therapy, and beyond," *Fems Microbiology Reviews,* vol. 37, no. 6, pp. 955-989, Nov 2013, doi: 10.1111/1574-6976.12026.

[87] J. Wang *et al.*, "Detection and analysis of reactive oxygen species (ROS) generated by nano-sized TiO2 powder under ultrasonic irradiation and application in sonocatalytic degradation of organic dyes," *Ultrasonics Sonochemistry,* vol. 18, no. 1, pp. 177-183, Jan 2011, doi: 10.1016/j.ultsonch.2010.05.002.

[88] N. N. Misra, D. Ziuzina, P. J. Cullen, and K. M. Keener, "CHARACTERIZATION OF A NOVEL ATMOSPHERIC AIR COLD PLASMA SYSTEM FOR TREATMENT OF PACKAGED BIOMATERIALS," *Transactions of the Asabe,* vol. 56, no. 3, pp. 1011-1016, May-Jun 2013. [Online]. Available: <Go to ISI>://WOS:000322504200018.

[89] S. K. Pankaj, Z. F. Wan, W. Colonna, and K. M. Keener, "Degradation kinetics of organic dyes in water by high voltage atmospheric air and modified air cold plasma," *Water Science and Technology,* vol. 76, no. 3, pp. 567-574, Jul 2017, doi: 10.2166/wst.2017.169.

[90] W. B. Dai, Y. F. Lei, M. Xu, P. Zhao, Z. H. Zhang, and J. Zhou, "Rare-Earth Free Self-Activated Graphene Quantum Dots and Copper-Cysteamine Phosphors for Enhanced White Light-Emitting-Diodes under Single Excitation," *Scientific Reports,* vol. 7, Oct 2017, Art no. 12872, doi: 10.1038/s41598-017-13404-1.

[91] H. Akafzade, S. C. Sharma, N. Hozhabri, W. Chen, and L. Ma, "Raman spectroscopy analysis of new copper-cysteamine photosensitizer," *Journal of Raman Spectroscopy,* vol. 50, no. 4, pp. 522-527, Apr 2019, doi: 10.1002/jrs.5541.

[92] S. Ahmad *et al.*, "Synthesis, theoretical calculations and antimicrobial studies of copper(I) complexes of cysteamine, cysteine and 2-mercaptonicotinic acid," *Polyhedron,* vol. 85, pp. 239-245, Jan 2015, doi: 10.1016/j.poly.2014.08.029.

[93] N. K. Pandey *et al.*, "A facile method for the synthesis of copper-cysteamine nanoparticles and study of ROS production for cancer treatment," *Journal of Materials Chemistry B,* vol. 7, no. 42, pp. 6630-6642, Nov 2019, doi: 10.1039/c9tb01566c.

[94] R. G. Parr and Y. Weitao, *Density-Functional Theory of Atoms and Molecules*. New York: Oxford University Press, 1989.

[95] R. O. Jones, "Density functional theory: Its origins, rise to prominence, and future," *Reviews of Modern Physics,* vol. 87, no. 3, pp. 897-923, Aug 2015, doi: 10.1103/RevModPhys.87.897.

[96] K. Capelle, "A bird's-eye view of density-functional theory," *Brazilian Journal of Physics,* vol. 36, no. 4A, pp. 1318-1343, Dec 2006, doi: 10.1590/s0103-97332006000700035.

[97] C. J. Cramer, *Essentials of Computational Chemistry Theories and Models*, 2nd ed. Chichester, West Sussex, England: Wiley, 2004.

[98] W. Kohn, "Nobel Lecture: Electronic structure of matter-wave functions and density functionals," *Reviews of Modern Physics,* vol. 71, no. 5, pp. 1253-1266, Oct 1999, doi: 10.1103/RevModPhys.71.1253.

[99] M. Jaminon, C. Mahaux, and P. Rochus, "SINGLE-PARTICLE POTENTIAL IN A RELATIVISTIC HARTREE-FOCK MEAN FIELD APPROXIMATION," *Nuclear Physics A,* vol. 365, no. 3, pp. 371-391, 1981, doi: 10.1016/0375-9474(81)90397-3.

[100] S. M. Blinder, "MODERN QUANTUM-CHEMISTRY - INTRODUCTION TO ADVANCED ELECTRONIC-STRUCTURE - SZABO,A, OSTLUND,NS," *Journal of the American Chemical Society,* vol. 105, no. 16, pp. 5523-5523, 1983. [Online]. Available: <Go to ISI>://WOS:A1983RC16600114.

[101] A. D. Becke, "Perspective: Fifty years of density-functional theory in chemical physics," *Journal of Chemical Physics,* vol. 140, no. 18, May 2014, Art no. 18a301, doi: 10.1063/1.4869598.

[102] T. van Mourik, M. Buhl, and M. P. Gaigeot, "Density functional theory across chemistry, physics and biology Introduction," *Philosophical Transactions of the Royal Society a-Mathematical Physical and Engineering Sciences,* vol. 372, no. 2011, Mar 2014, Art no. 20120488, doi: 10.1098/rsta.2012.0488.

[103] K. Burke and L. O. Wagner, "DFT in a nutshell," *International Journal of Quantum Chemistry,* vol. 113, no. 2, pp. 96-101, Jan 2013, doi: 10.1002/qua.24259.

[104] E. H. Lieb and B. Simon, "THOMAS-FERMI THEORY OF ATOMS, MOLECULES AND SOLIDS," *Advances in Mathematics,* vol. 23, no. 1, pp. 22-116, 1977, doi: 10.1016/0001-8708(77)90108-6.

[105] L. H. Thomas, "The calculation of atomic fields," *Proceedings of the Cambridge Philosophical Society,* vol. 23, pp. 542-548, Jul 1927, doi: 10.1017/s0305004100011683.

[106] P. Hohenberg and W. Kohn, "INHOMOGENEOUS ELECTRON GAS," *Physical Review B,* vol. 136, no. 3B, pp. B864-+, 1964, doi: 10.1103/PhysRev.136.B864.

[107] W. Kohn and L. J. Sham, "SELF-CONSISTENT EQUATIONS INCLUDING EXCHANGE AND CORRELATION EFFECTS," *Physical Review,* vol. 140, no. 4A, pp. 1133-&, 1965, doi: 10.1103/PhysRev.140.A1133.

[108] D. J. Griffiths, *Introduction to Quantum Mechanics*, 2nd ed. Upper Saddle River NJ: Pearson Prentice Hall, 2005.

[109] D. C. Langreth and M. J. Mehl, "BEYOND THE LOCAL-DENSITY APPROXIMATION IN CALCULATIONS OF GROUND-STATE ELECTRONIC-PROPERTIES," *Physical Review B,* vol. 28, no. 4, pp. 1809-1834, 1983, doi: 10.1103/PhysRevB.28.1809.

[110] S. Moroni, D. M. Ceperley, and G. Senatore, "STATIC RESPONSE AND LOCAL-FIELD FACTOR OF THE ELECTRON-GAS," *Physical Review Letters,* vol. 75, no. 4, pp. 689-692, Jul 1995, doi: 10.1103/PhysRevLett.75.689.

[111] P. R. Antoniewicz and L. Kleinman, "KOHN-SHAM EXCHANGE POTENTIAL EXACT TO 1ST ORDER IN RHO(K)/RHO0," *Physical Review B,* vol. 31, no. 10, pp. 6779-6781, 1985, doi: 10.1103/PhysRevB.31.6779.

[112] J. P. Perdew *et al.*, "ATOMS, MOLECULES, SOLIDS, AND SURFACES - APPLICATIONS OF THE GENERALIZED GRADIENT APPROXIMATION FOR EXCHANGE AND CORRELATION," *Physical Review B,* vol. 46, no. 11, pp. 6671-6687, Sep 1992, doi: 10.1103/PhysRevB.46.6671.

[113] J. P. Perdew, K. Burke, and M. Ernzerhof, "Generalized gradient approximation made simple," *Physical Review Letters,* vol. 77, no. 18, pp. 3865-3868, Oct 1996, doi: 10.1103/PhysRevLett.77.3865.

[114] C. Bowen, G. Sugiyama, and B. J. Alder, "STATIC DIELECTRIC RESPONSE OF THE ELECTRON-GAS," *Physical Review B,* vol. 50, no. 20, pp. 14838-14848, Nov 1994, doi: 10.1103/PhysRevB.50.14838.

[115] G. Ortiz, "GRADIENT-CORRECTED PSEUDOPOTENTIAL CALCULATIONS IN SEMICONDUCTORS," *Physical Review B,* vol. 45, no. 19, pp. 11328-11331, May 1992, doi: 10.1103/PhysRevB.45.11328.

[116] J. L. Bao, L. Gagliardi, and D. G. Truhlar, "Self-Interaction Error in Density Functional Theory: An Appraisal," *Journal of Physical Chemistry Letters,* vol. 9, no. 9, pp. 2353-2358, May 2018, doi: 10.1021/acs.jpclett.8b00242.

[117] F. Zhou, C. A. Marianetti, M. Cococcioni, D. Morgan, and G. Ceder, "Phase separation in LixFePO4 induced by correlation effects," *Physical Review B,* vol. 69, no. 20, May 2004, Art no. 201101, doi: 10.1103/PhysRevB.69.201101.

[118] A. D. Becke, "A NEW MIXING OF HARTREE-FOCK AND LOCAL DENSITY-FUNCTIONAL THEORIES," *Journal of Chemical Physics,* vol. 98, no. 2, pp. 1372-1377, Jan 1993, doi: 10.1063/1.464304.

[119] J. Heyd and G. E. Scuseria, "Efficient hybrid density functional calculations in solids: Assessment of the Heyd-Scuseria-Ernzerhof screened Coulomb hybrid functional," *Journal of Chemical Physics,* vol. 121, no. 3, pp. 1187-1192, Jul 2004, doi: 10.1063/1.1760074.

[120] J. Heyd, G. E. Scuseria, and M. Ernzerhof, "Hybrid functionals based on a screened Coulomb potential," *Journal of Chemical Physics,* vol. 118, no. 18, pp. 8207-8215, May 2003, doi: 10.1063/1.1564060.

[121] J. Heyd, G. E. Scuseria, and M. Ernzerhof, "Hybrid functionals based on a screened Coulomb potential (vol 118, pg 8207, 2003)," *Journal of Chemical Physics,* vol. 124, no. 21, Jun 2006, Art no. 219906, doi: 10.1063/1.2204597.

[122] A. V. Krukau, O. A. Vydrov, A. F. Izmaylov, and G. E. Scuseria, "Influence of the exchange screening parameter on the performance of screened hybrid functionals," *Journal of Chemical Physics,* vol. 125, no. 22, Dec 2006, Art no. 224106, doi: 10.1063/1.2404663.

[123] G. Kresse and J. Furthmuller, "Efficient iterative schemes for ab initio total-energy calculations using a plane-wave basis set," *Physical Review B,* vol. 54, no. 16, pp. 11169-11186, Oct 1996, doi: 10.1103/PhysRevB.54.11169.

[124] G. Kresse and J. Furthmuller, "Efficiency of ab-initio total energy calculations for metals and semiconductors using a plane-wave basis set," *Computational Materials Science,* vol. 6, no. 1, pp. 15-50, Jul 1996, doi: 10.1016/0927-0256(96)00008-0.

[125] P. E. Blochl, "PROJECTOR AUGMENTED-WAVE METHOD," *Physical Review B,* vol. 50, no. 24, pp. 17953-17979, Dec 1994, doi: 10.1103/PhysRevB.50.17953.

[126] G. Kresse and D. Joubert, "From ultrasoft pseudopotentials to the projector augmented-wave method," *Physical Review B,* vol. 59, no. 3, pp. 1758-1775, Jan 1999, doi: 10.1103/PhysRevB.59.1758.

[127] J. Paier, R. Hirschl, M. Marsman, and G. Kresse, "The Perdew-Burke-Ernzerhof exchange-correlation functional applied to the G2-1 test set using a plane-wave basis set," *Journal of Chemical Physics,* vol. 122, no. 23, Jun 2005, Art no. 234102, doi: 10.1063/1.1926272.

[128] K. Momma and F. Izumi, "VESTA: a three-dimensional visualization system for electronic and structural analysis," *Journal of Applied Crystallography,* vol. 41, pp. 653-658, Jun 2008, doi: 10.1107/s0021889808012016.

[129] P. E. Blochl, O. Jepsen, and O. K. Andersen, "IMPROVED TETRAHEDRON METHOD FOR BRILLOUIN-ZONE INTEGRATIONS," *Physical Review B,* vol. 49, no. 23, pp. 16223-16233, Jun 1994, doi: 10.1103/PhysRevB.49.16223.

[130] K. Berland *et al.*, "van der Waals forces in density functional theory: a review of the vdW-DF method," *Reports on Progress in Physics,* vol. 78, no. 6, Jun 2015, Art no. 066501, doi: 10.1088/0034-4885/78/6/066501.

[131] M. Dion, H. Rydberg, E. Schroder, D. C. Langreth, and B. I. Lundqvist, "Van der Waals density functional for general geometries," *Physical Review Letters,* vol. 92, no. 24, Jun 2004, Art no. 246401, doi: 10.1103/PhysRevLett.92.246401.

[132] J. Klimes, D. R. Bowler, and A. Michaelides, "Chemical accuracy for the van der Waals density functional," *Journal of Physics-Condensed Matter,* vol. 22, no. 2, Jan 2010, Art no. 022201, doi: 10.1088/0953-8984/22/2/022201.

[133] J. Klimes, D. R. Bowler, and A. Michaelides, "Van der Waals density functionals applied to solids," *Physical Review B,* vol. 83, no. 19, May 2011, Art no. 195131, doi: 10.1103/PhysRevB.83.195131.

[134] K. Lee, E. D. Murray, L. Z. Kong, B. I. Lundqvist, and D. C. Langreth, "Higher-accuracy van der Waals density functional," *Physical Review B,* vol. 82, no. 8, Aug 2010, Art no. 081101, doi: 10.1103/PhysRevB.82.081101.

[135] G. Roman-Perez and J. M. Soler, "Efficient Implementation of a van der Waals Density Functional: Application to Double-Wall Carbon Nanotubes," *Physical Review Letters,* vol. 103, no. 9, Aug 2009, Art no. 096102, doi: 10.1103/PhysRevLett.103.096102.

[136] T. Thonhauser, V. R. Cooper, S. Li, A. Puzder, P. Hyldgaard, and D. C. Langreth, "Van der Waals density functional: Self-consistent potential and the nature of the van der Waals bond," *Physical Review B,* vol. 76, no. 12, Sep 2007, Art no. 125112, doi: 10.1103/PhysRevB.76.125112.

[137] S. K. Barman and M. N. Huda, "First-principles study on the effect of Sn doping in Cu2S-Acanthite phase as a substitute to low chalcocite for modeling complex doping," *Journal of Applied Physics,* vol. 128, no. 1, Jul 2020, Art no. 015703, doi: 10.1063/5.0008499.

[138] H. P. Sarker, P. M. Rao, and M. N. Huda, "Niobium Doping in BiVO4: Interplay Between Effective Mass, Stability, and Pressure," *Chemphyschem,* vol. 20, no. 5, pp. 773-784, Mar 2019, doi: 10.1002/cphc.201800792.

[139] H. Akkus and A. M. Mamedov, "Ab initio calculations of the electronic structure and linear optical properties, including self-energy effects, for paraelectric SbSI," *Journal of Physics-Condensed Matter,* vol. 19, no. 11, Mar 2007, Art no. 116207, doi: 10.1088/0953-8984/19/11/116207.

[140] L. P. Dong, R. X. Jia, B. Xin, B. Peng, and Y. M. Zhang, "Effects of oxygen vacancies on the structural and optical properties of beta-Ga2O3," *Scientific Reports,* vol. 7, Jan 2017, Art no. 40160, doi: 10.1038/srep40160.

[141] P. Rani, G. S. Dubey, and V. K. Jindal, "DFT study of optical properties of pure and doped graphene," *Physica E-Low-Dimensional Systems & Nanostructures,* vol. 62, pp. 28-35, Aug 2014, doi: 10.1016/j.physe.2014.04.010.

[142] R. F. W. Bader, "ATOMS IN MOLECULES," *Accounts of Chemical Research,* vol. 18, no. 1, pp. 9-15, 1985, doi: 10.1021/ar00109a003.

[143] E. Sanville, S. D. Kenny, R. Smith, and G. Henkelman, "Improved grid-based algorithm for Bader charge allocation," *Journal of Computational Chemistry,* vol. 28, no. 5, pp. 899-908, Apr 2007, doi: 10.1002/jcc.20575.

[144] G. Henkelman, A. Arnaldsson, and H. Jonsson, "A fast and robust algorithm for Bader decomposition of charge density," *Computational Materials Science,* vol. 36, no. 3, pp. 354-360, Jun 2006, doi: 10.1016/j.commatsci.2005.04.010.

[145] W. Tang, E. Sanville, and G. Henkelman, "A grid-based Bader analysis algorithm without lattice bias," *Journal of Physics-Condensed Matter,* vol. 21, no. 8, Feb 2009, Art no. 084204, doi: 10.1088/0953-8984/21/8/084204.

[146] M. Yu and D. R. Trinkle, "Accurate and efficient algorithm for Bader charge integration," *Journal of Chemical Physics,* vol. 134, no. 6, Feb 2011, Art no. 064111, doi: 10.1063/1.3553716.

[147] Y. Wang *et al.*, "A new type of cuprous-cysteamine sensitizers: Synthesis, optical properties and potential applications," *Materials Today Physics,* vol. 19, Jul 2021, Art no. 100435, doi: 10.1016/j.mtphys.2021.100435.

[148] M. Cococcioni, "The LDA+ U approach: a simple Hubbard correction for correlated ground states," *Correlated Electrons: From Models to Materials Modeling and Simulation,* vol. 2, 2012.

[149] S. L. Dudarev, G. A. Botton, S. Y. Savrasov, C. J. Humphreys, and A. P. Sutton, "Electron-energy-loss spectra and the structural stability of nickel oxide: An LSDA+U study," *Physical Review B,* vol. 57, no. 3, pp. 1505-1509, Jan 1998, doi: 10.1103/PhysRevB.57.1505.

[150] S. Y. Chang *et al.*, "Structure and bonding in Au(I) chloride species: a critical examination of X-ray absorption spectroscopy (XAS) data," *Rsc Advances,* vol. 5, no. 9, pp. 6912-6918, 2015, doi: 10.1039/c4ra13087a.